Spatial Distortion and Image Quality Assessment of Gradient Echo Imaging for Radiation Therapy Planning

Mithunan Modchalingam

Master of Science

Medical Physics Unit

McGill University
Montreal, Quebec

November 27, 2017

A thesis submitted to McGill University in partial fulfillment of the requirements of the degree of Master of Science in Medical Radiation Physics

Acknowledgments

I would first and foremost like to thank my supervisor, Ives Levesque, for the continued support and guidance through out the course of my project. As this was my first MRI project, under his supervision I was able to obtain a solid foundation of MR knowledge which I hope to build on moving forward. I would also like to thank my lab mates in the McGill MRI Methods group. Specifically, I would like to thank: Véronique Fortier for helping me get accustomed to the MRI, helping me acquire images when necessary, and helping me with the phase unwrapping, Stella Xing for setting up and showing me how to work with MIMVista, and Zaki Ahmed for providing information for the simulations.

I would also like to thank Joe Larkin for his work in building the grid phantom, Daniel Markel for introducing me to registrations, as well as Guillaume Gilbert from Philips Healthcare for supplying the SWIp-QSM pulse sequence used to obtain phase data.

Additionally, I would like to acknowledge the funding provided by both the NSERC CREATE grant, as well as the McGill Faculty of Medicine.

Finally and most importantly, I would like to thank my parents for their unwavering support, without which none of this would have been possible.

Abstract

Imaging is crucial prior to the administration of radiation therapy for the delineation of critical structures. Though CT scans are the standard for radiation therapy planning images, MRI provides increased soft tissue contrast leading to more accurate target delineation. One disadvantage of MR images however is that they suffer from geometric image distortions that reduce spatial precision. System-specific distortions were measured using a pelvis sized grid phantom and a non-linear demons registration. Radial distances from the isocenter with spatial distortions below 2 mm were determined for the T1-w 3D GRE, T2-w 2D SE, T2-w 3D SE, and T1-w THRIVE on a Philips 3 T Ingenia MRI. They were found to be 255 mm, 154 mm, 250 mm, and 230 mm respectively. The distortions were seen to be reduced with increasing bandwidth. Sequence independent distortions were also measured to be below 1.5 mm for radial distances below 270 mm. Areas of high expected patient-dependent distortions were then determined in the head of a healthy volunteer and seen to be at air-tissue and air-bone interfaces. These distortions were also reduced with an increase in bandwidth, at the cost of SNR. Multi-echo averaging and conventional signal averaging were performed to regain SNR and compared in terms of SNR, CNR and qualitative image quality. Multi-echo averaging outperformed conventional signal averaging in terms of SNR and CNR, and was equivalent to or better than conventional signal averaging in terms of qualitative image quality. Altogether, the use of high readout bandwidth and multi-echo averaging improves the quality of three-dimensional gradient echo MRI for use in radiation therapy.

Abrégé

L'imagerie est cruciale pour le tracé des structures critiques avant l'administration de la radiothérapie. Quoique la tomodensitométrie est la norme pour les images de planification en radiothérapie, l'imagerie par résonance magnétique (IRM) fournit un contraste accrue des tissus mous menant à une délimitation plus précise de la cible. Un inconvénient des images IRM est cependant qu'elles souffrent de distorsions géométrique qui réduisent la précision spatiale. Les distortions spécifiques au système ont été mesurées à l'aide d'un fantôme à structure de grille et grâce au recalage non linéaire par la méthode Demons. Les distances radiales de l'isocentre acceptable pour la planification de la radiothérapie sur un Philips 3 T Ingenia mesurées pour les séquences d'écho de gradient 3-dimensions pondérée T1, écho de spin pondérée T2 (2 et 3 dimensions), et « THRIVE » pondérée T1 sont avéré être 255 mm, 154 mm, 250 mm et 230 mm, respectivement. Les distorsions ont été réduites avec une augmentation de la bande passante en réception. Les distorsions indépendantes de la séquence ont également été mesurées et se situent au-dessous de 1,5 mm pour une distance radiale de 270 mm. Les zones de grandes distortions dûes au patient furent ensuite mesurées dans la tête d'un volontaire humain et observées aux interfaces air-tissus et air-os. Ces distorsions furent également réduites avec une augmentation de la bande passante en réception, au détriment du rapport signal-bruit. Une pondération multi-écho et une pondération de signal conventionnel ont été évaluées pour rétablir le rapport signal-bruit original, et comparées en termes de rapport contraste-bruit et de qualité d'image. La pondération multi-écho a surpassé le signal conventionnel en termes de rapport signal-bruit et contraste-bruit et était équivalent ou mieux que le signal conventionnel en termes de qualité d'image qualitative. En somme, l'utilisation d'une large bande passante de réception et la pondération multi-écho améliore la qualité d'image IRM d'écho de gradient 3D pour l'utilisation en radiothérapie.

Contents

List of Figures

List of Tables

List of Abbreviations

ACR American College of Radiology

AP Anterior-Posterior

BW Readout Bandwidth

CNR Contrast-to-noise Ratio

CTV Clinical Target Volume

CT Computed Tomography

ETL Echo Train Length

FOV Field of View

GM Grey Matter

GRE Gradient Recalled Echo

GTV Gross Tumor Volume

IMPT Intensity Modulated Proton Therapy

IMRT Intensity Modulated Radiation Therapy

LR Left-Right

ME Multi-Echo

MRI Magnetic Resonance Imaging

MR Magnetic Resonance

MU Monitor Units

NMR Nuclear Magnetic Resonance

NSA Number of Signal Averages

PD Proton Density

PMMA Poly(methyl methacrylate)

ppm Parts per Million

PTV Planning Target Volume

SE Spin Echo

SI Superior-Inferior

SNR Signal-to-noise Ratio

T1-w T1-weighted

T2-w T2-weighted

TE Echo Time

TR Repetition Time

WM White Matter

Chapter 1

Introduction

Imaging is a crucial step prior to the administration of radiation therapy used to define target and critical structure volumes. The current standard for the acquisition of radiation therapy planning images is a CT scan due to its ability to create spatially precise images, along with providing electron density information required for planning. Though CT is the current gold standard, it does not provide the same degree of soft tissue contrast as MRI. With increased soft tissue contrast, more accurate target delineation can be achieved thereby producing an improved treatment plan.

MRI however suffers from certain key limitations which currently make MRI-only treatment planning difficult to implement. One main limitation is the inability of MRI to provide electron density information required for dose calculations. One method which accounts for this is known as bulk density assignment, where an electron density is assigned to regions of similar tissue for use in dose calculations. The plans computed from the bulk density assignment method were compared to plans computed from CT images with no inhomogeneity corrections and were seen to be very comparable. The maximum difference in the MUs were seen to be within 1.6% in the lung [28].

The second drawback of MRI, and the topic of this thesis, is the reduced spatial precision caused by image distortions. As radiation therapy involves large radiation doses deposited to specific regions, spatial precision is paramount to ensure the dose is appropriately distributed. These distortions are caused by inhomogeneities in the main magnetic field, the non-linearities of the pulsed gradient fields, and large susceptibility differences in adjacent regions, and can result in millimetre shifts in the acquired images. Though these distortions may not be a problem for diagnostic imaging, a spatial precision of <2 mm is required for radiation therapy planning images [64, 69]. The inhomogeneity of the main magnet, as well as the non-linearity of the gradient fields, depend on the system hardware and thus need to be measured on a site by site basis for a variety of pulse sequences [64].

The aims of this work were to characterize system-dependent and patient-dependent distortions, along with improve gradient echo image quality. This thesis summarizes the measurement of the distortion field in the Philips Ingenia 3 T MR scanner at the McGill University Health Centre - Glen Site for a variety of clinically relevant pulse sequences. Measurements were acquired using a constructed grid phantom with a volume similar to that of a adult human pelvis. A CT image of the phantom was acquired to act as the undistorted gold standard image, for comparison with the distorted MR images acquired using varying sequences. To determine the distortion field, a registration method was used whereby the MR images were linearly registered to the CT image, following which the linearly registered MR images were non-linearly registered again to the CT image. The deformation field obtained during the non-linear registration was taken to be the distortion field for the sequences used.

In addition to system dependent distortion measurements, a multi-echo gradient echo sequence was also studied in order to improve image quality. Patient-dependent susceptibility distortions were calculated from images acquired in a healthy volunteer and areas of high expected distortions were qualitatively observed. The bandwidth was increased in order to reduce these distortions, at the cost of SNR, and multi-echo averaging along with conventional signal averaging were used to regain the SNR. The images produced by multi-echo averaging and conventional signal averaging were compared qualitatively in their ability to depict critical structures in brain radiotherapy, and finally these two methods were compared quantitatively in their ability to regain SNR and maintaining CNR.

The work of this thesis is presented in 5 chapters. In addition to the current introductory chapter, Chapter 2 presents background information on the physics of MRI, its application to radiation therapy, as well as relevant studies in distortion field quantification. Chapter 3 then presents the methods in detail, whereas Chapter 4 presents the results of these experiments and an associated discussion. Finally, Chapter 5 gives a conclusion of the results and suggestions of future work to be completed.

Chapter 2

Background

2.1 MRI basics

2.1.1 Spins and Magnetic Moment

Spin is a fundamental property of subatomic particles that plays a significant role in Magnetic Resonance Imaging (MRI). It is an intrinsic value of a subatomic particle's angular momentum, and takes a discrete integer or half integer value. Protons, neutron and electrons all have spin values of $+\frac{1}{2}$. Only atoms with non-zero nuclear spins can be used in MRI as only they are able to absorb and emit electromagnetic radiation and undergo nuclear magnetic resonance (NMR). ^{1}H is the most abundant atom in the universe and, due to possessing a single proton as its nucleus, has a spin of $+\frac{1}{2}$. Since ^{1}H has a non-zero spin and is the most abundant atom in the body, the majority of MRI scans use ^{1}H as the primary NMR isotope.

A magnetic moment is a vector which is used to measure the torque an object will experience when placed in an external magnetic field. The magnetic moments of ^{1}H atoms within the body are oriented evenly when not placed inside an external field. This results in a lack of net magnetization. When placed under an external magnetic field, such as an MRI scanner, the magnetic moments of the ^{1}H align with the direction of the magnetic field. In the classical picture, these magnetic moments will experience a torque which is applied until they are perfectly aligned with the B_0 field as seen in 2.1. The magnetic moments can be thought of in the classical picture as it is sufficient to understand MR imaging. The alignment of these magnetic moments thus creates a net magnetization in the direction of the B_0 field within the MRI [46].

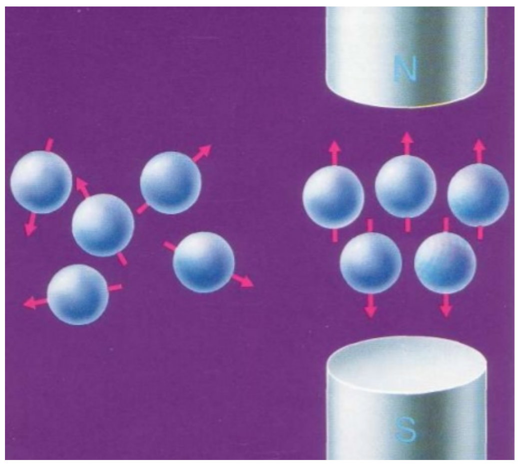

Figure 2.1: The magnetic moments of protons are distributed in random directions when not in an applied magnetic field. When a magnetic field is applied the magnetic moments align in the direction of the applied field to create a net magnetization. Image obtained from [46] pg 7

The spin and the magnetic moment are linearly proportional and are related through the gyromagnetic ratio.

$$\mu = \gamma I \tag{2.1}$$

The relation can be seen above in (2.1) where μ represents the magnetic moment, γ the gyromagnetic ratio, and I the nuclear spin. The SI unit of the gyromagnetic ratio is $rad \cdot s^{-1} \cdot T^{-1}$ but is typically stated as $\frac{\gamma}{2\pi}$ in MHz/tesla due to its role in the Larmor equation explained in section 2.1.3. The gyromagnetic ratio has a positive value when the spin and the magnetic moment point in the same direction and a negative value when these directions are opposite. An important $\frac{\gamma}{2\pi}$ is that of the ^{1}H nucleus, which has a value of 42.58 MHz/T.

2.1.2 Spin States

In the quantum mechanical picture, once placed in the B_0 field the spins begin to sort into two spins states known as spin-up, or parallel, and spin-down, or anti-parallel. As the names suggest, the spins in the parallel state are in alignment with the external magnetic field whereas the spins in the anti-parallel state oppose the external field. The spins in the parallel configuration are in an energy level defined by (2.2) whereas the anti-parallel spins are in an energy level defined by (2.3). Here γ represents the gyromagnetic ratio and h the Planck's constant.

$$E_+ = \frac{-\gamma h B_0}{4\pi} \tag{2.2}$$

$$E_- = \frac{\gamma h B_0}{4\pi} \tag{2.3}$$

The negative sign of (2.2) suggest that the parallel energy level is a lower energy level than that of the anti-parallel state. The energy difference between the two levels is stated in Equation (2.4)

$$\Delta E = \frac{\gamma h B_0}{2\pi} \tag{2.4}$$

With the energy difference obtained, the Boltzmann distribution can then be used to calculate the relative number of nuclei in the parallel and anti-parallel configurations as seen in (2.5).

$$\frac{N_{antiparallel}}{N_{parallel}} = exp(\frac{-\Delta E}{kT}) = exp(\frac{-\gamma h B_0}{2\pi kT}) \tag{2.5}$$

Here k represents the Boltzmann constant, $1.38 \times 10^{-23} m^2 kg s^{-2} K^{-1}$, and T the absolute temperature in kelvin. With the use of the approximation $e^{-x} \approx 1 - x$ the relative number of spins in each state can be further simplified to that seen in (2.6).

$$\frac{N_{antiparallel}}{N_{parallel}} = 1 - \frac{\gamma h B_0}{2\pi kT} \tag{2.6}$$

From (2.6) it can be seen that, at equilibrium, there will always be more parallel spins than antiparallel spins, primarily due to the parallel state being that of a lower energy [46, 67].

2.1.3 Net Magnetization, Precession, and Excitation

The excess parallel spins thus create an observable quantity known as the net nuclear magnetization. The net magnetization is the sum of the magnetic moments as seen in (2.7). Due to the excess number of parallel spins once placed in an applied magnetic field, the magnetic moments create a net magnetization in the direction of the applied magnetic field. In MRI, this direction is normally referred to as the longitudinal axis.

$$M = \sum_{volume} \mu \tag{2.7}$$

To obtain an MRI signal however, transitions between the parallel and antiparallel energy levels must be induced. To do this, a time varying magnetic field must be applied at a certain frequency. Through the use energy difference obtained in (2.4) the frequency of the wave required can be derived as seen in (2.8).

$$\begin{aligned} hf &= \Delta E = \frac{\gamma h B_0}{2\pi} \\ f &= \frac{\gamma B_0}{2\pi} \end{aligned} \tag{2.8}$$

The frequency stated in (2.8) is given in units of Hz but, with the multiplication of 2π, can be changed to units of radians per second. By doing so, the required angular frequency ω_0 can be obtained as seen (2.9). This is known as the Larmor frequency.

$$\omega_0 = \gamma B_0 \tag{2.9}$$

The applied time-varying magnetic field, with the angular frequency ω_0, used to excite the spins is known as the B_1 pulse. The B_1 pulse is applied perpendicular to the static B_0 field of the MRI, and through manipulation of the amplitude and duration of the pulse, dictates the angle with which the net magnetization is flipped. A commonly used flip angle is 90 degrees, which results in the net magnetization being flipped from the longitudinal axis to the transverse plane. Once flipped the net magnetization undergoes precession which again occurs at the Larmor frequency. Further discussion of the precession along with its mathematical representation can be found in 2.1.5

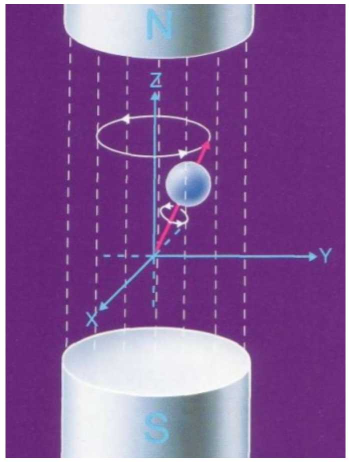

Figure 2.2: Once an RF pulse is applied to the net magnetization it begins to precess about the longitudinal axis. Image taken from [46] pg 9

2.1.4 Relaxation

Once the B_1 pulse has been used to flip the net magnetization to the transverse plane, relaxation occurs. The longitudinal component of the magnetization begins to recover as described by (2.10)

$$\frac{dM_z}{dt} = -\frac{M_z - M_0}{T_1} \tag{2.10}$$

To which the solution is (2.11)

$$M_z(t) = M_0 + (M_z(0) - M_0)e^{-t/T_1} \tag{2.11}$$

T_1 is known as the spin-lattice time constant, which defines the time it takes for an object to regain 63% of its equilibrium z-component magnetization. The T_1 relaxation involves the exchange of energy between the nuclei used for the scan and the lattice which surrounds it. The spins excited from the parallel state to the antiparallel state de-excite through the emission of photons to return to their original states. Given enough time, the M_z following the application of B_1 pulse will return to its initial state, M_0, at which it is at thermal equilibrium [36].

Following a commonly used flip angle of 90 degrees, the recovery of the longitudinal magnetization can be described by Equation (2.12)

$$M_z(t) = M_0(1 - e^{-t/T_1}) \tag{2.12}$$

Along with longitudinal relaxation, the system also experiences transverse relaxation. Since the net magnetization is flipped into the transverse plane, a loss of this transverse magnetization is required to achieve thermal equilibrium. The transverse relaxation time is described by (2.13)

$$\frac{dM_{xy}}{dt} = \frac{-M_{xy}}{T_2} \tag{2.13}$$

To which the solution for a common 90 degree pulse is (2.14)

$$M_{xy}(t) = M_{xy}(t = 0)e^{-t/T_2} \tag{2.14}$$

Here, the T_2 is known as the spin-spin time constant. Loss of phase coherence leads to loss of transverse magnetization. This dephasing can be caused by fluctuations in the magnetic field, and z component fluctuations, which cause dephasing but not spin transitions, are the dominant cause of this relaxation process [36]. Along with magnetic field discrepancies, impurities in the sample, the chemical environment, and the system imperfections can all cause a loss of phase coherence faster than that defined by T_2. The additional effect on the transverse magnetization is often defined by a second term ${T_2}'$ which when combined with T_2 gives a time constant ${T_2}^*$ which accounts for these static processes. The relation between the three terms can be seen below in (2.15)

$$\frac{1}{T_2{}^*} = \frac{1}{T_2} + \frac{1}{T_2{}'} \tag{2.15}$$

Different objects and different types of material in the body exhibit different T_1, T_2, and $T_2{}^*$ values. This then causes varying rates of relaxation which, through the manipulation of pulse sequence parameters, allows a pathway by which contrast can be obtained. Pulse sequences and contrast are discussed further in section 2.2.

2.1.5 Bloch Equation

The behaviour of the net magnetization is described by the Bloch equation. The Bloch equation is able to define the precession of the net magnetization while taking the longitudinal and transverse relaxation into consideration as seen in (2.16).

$$\frac{d\mathbf{M}}{dt} = \mathbf{M} \times \gamma\mathbf{B} - \frac{M_x\hat{\mathbf{i}} + M_y\hat{\mathbf{j}}}{T_2} - \frac{(M_z - M_0)\hat{\mathbf{k}}}{T_1} \tag{2.16}$$

In Equation 2.16, $\mathbf{M} \times \gamma\mathbf{B}$ describes the precession of the net magnetization. As the cross product is taken of $\mathbf{M}$ and $\mathbf{B}$, this states that the precession of the net magnetization will be in a direction perpendicular to the net magnetization vector and the magnetic field vector. This is also the reason the B_1 excitation pulse is applied perpendicular to the B_0 field as discussed in section 2.1.3. Along with this, from (2.9) it can be seen that the net magnetization precesses at the Larmor frequency.

The $-\frac{M_x\hat{\mathbf{i}} + M_y\hat{\mathbf{j}}}{T_2}$ term shows the loss of transverse magnetization as described by an object's T_2 value whereas the $-\frac{(M_z - M_0)\hat{\mathbf{k}}}{T_1}$ term is the recovery of the longitudinal magnetization as described by an object's $T1$ value.

The precession component of the Bloch equation can be written in matrix notation and shown as (2.17)

$$\begin{pmatrix} \frac{dM_x}{dt} \\ \frac{dM_y}{dt} \\ \frac{dM_z}{dt} \end{pmatrix} = \begin{pmatrix} 0 & \gamma B_0 & 0 \\ -\gamma B_0 & 0 & 0 \\ 0 & 0 & 0 \end{pmatrix} \begin{pmatrix} M_x \\ M_y \\ M_z \end{pmatrix} \tag{2.17}$$

By including the relaxation terms, the Bloch equation in matrix form then becomes (2.18)

$$\begin{pmatrix} \frac{dM_x}{dt} \\ \frac{dM_y}{dt} \\ \frac{dM_z}{dt} \end{pmatrix} = \begin{pmatrix} -1/T_2 & \gamma B_0 & 0 \\ -\gamma B_0 & -1/T_2 & 0 \\ 0 & 0 & -1/T_1 \end{pmatrix} \begin{pmatrix} M_x \\ M_y \\ M_z \end{pmatrix} + \begin{pmatrix} 0 \\ 0 \\ \frac{M_0}{T_1} \end{pmatrix} \tag{2.18}$$

By using (2.9) the solution to (2.18) can be shown to be (2.19)

$$\mathbf{M}(t) = \begin{pmatrix} e^{-t/T_2} & 0 & 0 \\ 0 & e^{-t/T_2} & 0 \\ 0 & 0 & e^{-t/T_1} \end{pmatrix} \mathbf{R}_z(\omega_0 t)\mathbf{M}_0 + \begin{pmatrix} 0 \\ 0 \\ M_0(1 - e^{-t/T_1}) \end{pmatrix} \tag{2.19}$$

where

$$\mathbf{R}_z(\omega_0 t) = \begin{pmatrix} cos(\omega_0 t) & sin(\omega_0 t) & 0 \\ -sin(\omega_0 t) & cos(\omega_0 t) & 0 \\ 0 & 0 & 1 \end{pmatrix} \tag{2.20}$$

In (2.19), $\mathbf{M}_0$ represents the initial net magnetization and $\mathbf{R}_z(\omega_0 t)$ the rotation about the z axis at the angular frequency ω_0. Here it is clear to see the rotation of the net magnetization at the Larmor frequency ω_0 about the z axis, along with the exponential decay of the transverse magnetization, and the recovery of the longitudinal magnetization [36].

2.1.6 Gradient field

As the signal received is the sum of all spin contribution in the sensitive volume of the receive coil, spatial information is lost within a homogeneous field. As such, an additional method is required for spatial encoding. Gradient fields cause a spatial linearly varying magnetic field in the MRI that is used for spatial encoding within the image. There are three coils within the MR which are used for spatial encoding in the x, y and z direction. The gradients used for encoding the x and y directions are performed with saddle coils, whereas the spatial encoding in the z direction is performed with the use of a Maxwell coil. This can be seen in Figure 2.3.

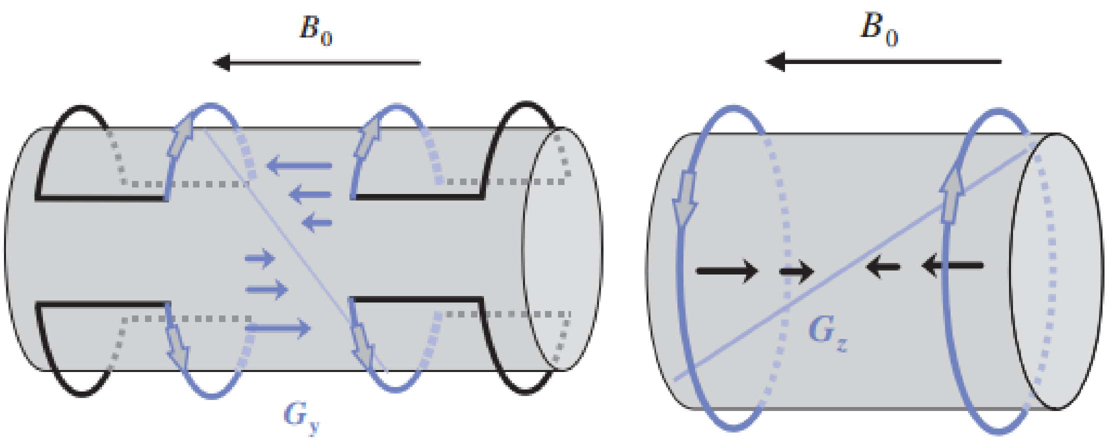

(a) **(b)**

Figure 2.3: (a) A saddle coil and a (b) Maxwell coil used for spatial encoding within an MRI. Image obtained from [35] pg. 174.

The gradient field changes the value of the static magnetic field as a function of the position within the scanner, thereby changing the Larmor frequency as a function of position. Three gradients exist to allow for a variation in the Larmor frequency in the x, y, and z directions. (2.9) defines the value of the Larmor frequency and its dependence of the magnetic field strength very clearly. By adding an x gradient for example, the value of the magnetic field will change in the x direction for the z component of the static field as described by (2.21)

$$\frac{dB_z}{dx} = G_x \tag{2.21}$$

The x gradient thus changes the Larmor frequency as defined by (2.22)

$$\Delta\omega(x) = \gamma G_x x \tag{2.22}$$

The Larmor frequency as a function of position can then be obtained by the addition of the Larmor frequency set by the static B_0 field and the variation caused by the gradients. This leads to a location dependent frequency as seen in (2.23)

$$\omega(x) = \omega_0 + \Delta\omega(x) = \gamma(B_0 + G_x x) \tag{2.23}$$

2.1.7 Frequency and Phase Encoding

The gradient fields discussed in section 2.1.6 allow for spatial localization through frequency and phase encoding. When the frequency encoding gradient field is turned on during signal acquisition, the resonant frequencies vary as a function of location along the frequency encode axis, as described by 2.22. Since the resonance frequency varies along the frequency encode direction, this in turn results in a range of frequencies being associated with each pixel. This allows for spatial encoding in one direction as each pixel will have a different range of frequencies associated with it.

Frequency encoding allows for spatial location in one direction, but phase encoding is required to allow for spatial encoding in a second axis. The phase encode gradient is turned on and off to dephase the spins about the phase encode axis. The spins are phase shifted linearly as a function of their position along the phase encode direction. Along with the frequency encoding, the phase encoding allows for localization in 2D. The use of successive frequency and phase encodes for the acquisition of MR images is known as spin warp MRI [17].

The frequency and phase encode gradients are turned on and off following the excitation pulse. This sets the initial spatial frequency coordinates in k-space. The frequency encode gradient is once again turned on during signal acquisition to allow for the collection of signal through one line of k-space. The phase encoding process is then repeated to collect many phase encoding patterns, adding up to the total amount of data required to reconstruct an image. A further mathematical explanation can be seen in section 2.1.8.

Multi-slice acquisitions, using slice selective excitation, will result in a 3D image data set acquired using a 2D sequence. To perform slice selective excitation a second frequency encode gradient, referred to as a slice selection gradient, as well as an appropriate RF pulse is required. Unlike spatial encoding using the frequency encode gradient, for slice selective excitation the frequency encode gradient is turned on during the excitation pulse. The gradient field is used to change the resonant frequencies as a function of position in the slice direction. The excitation pulse applied during this time is such that the bandwidth covers the range of frequencies to be excited. This ultimately results in the excitation of a slice. Since the gradient field changes the resonant frequencies within the MR in the slice direction, the spins outside the ranges of frequencies will not be excited by the RF pulse and therefore slice selective excitation can be achieved.

Three-dimensional imaging can also be performed as opposed to multi-slice imaging. 3D sequences allow for spatial localization in all three dimensions with the use of two phase encodes. This allows for excitation and imaging of an entire volume rather than of multiple slices. 3D sequences have a few advantages to 2D multi-slice imaging in terms of increased signal-to-ratio (SNR) [70] and smaller slice thicknesses, but tend to suffer from longer imaging times.

2.1.8 MRI Signal

The receive coil of the MRI is sensitive over the volume of the receive-coil and is able to detect changes in magnetic flux, in the transverse direction, caused by precession. As sensitivity is not uniform however, spatial variations have been neglected. The time signal can therefore be stated as (2.24)

$$\begin{aligned} s_r(t) &= \int_{vol} M_{x,y}(r,t)dV \\ s_r(t) &= \int_x \int_y \int_z M_{x,y}(x,y,z,t)dxdydz \end{aligned} \tag{2.24}$$

(2.24) can then be further developed and stated as (2.25) to take into account the initial magnetization, relaxation, precession, and the effect of a time varying gradient field.

$$s_r(t) = \int\int\int M_{x,y}(x,y,z,t)e^{-t/T_2(r)}e^{-i\omega_0 t}exp\bigg(-i\gamma\int_0^t G(\tau)\cdot r d\tau\bigg)dxdydz \tag{2.25}$$

For simplicity's sake, the relaxation term defined by $e^{-t/T_2(r)}$ can be ignored. Additionally since the signal is demodulated by ω_0 the term $e^{-i\omega_0 t}$ can also be omitted.
The time varying gradients can further be separated in x, y and z and stated as $G_x(t)$, $G_y(t)$ and $G_z(t)$. By combining all stated simplifications Equation (2.25) can be written as (2.26)

$$\begin{aligned} s_r(t) = \int\int\int M_{x,y}(x,y,z,t)exp\bigg[-i\gamma x\bigg(\int_0^t G_x(\tau)d\tau\bigg)\bigg]\cdot exp\bigg[-i\gamma y\bigg(\int_0^t G_y(\tau)d\tau\bigg)\bigg] \\ \cdot exp\bigg[-i\gamma z\bigg(\int_0^t G_z(\tau)d\tau\bigg)\bigg]dxdydz \end{aligned} \tag{2.26}$$

The effects of the time varying gradient fields can be further stated as (2.27).

$$
\begin{aligned}
k_x(t) &= \frac{\gamma}{2\pi}\int_0^t G_x(\tau)d\tau \\
k_y(t) &= \frac{\gamma}{2\pi}\int_0^t G_y(\tau)d\tau \\
k_z(t) &= \frac{\gamma}{2\pi}\int_0^t G_z(\tau)d\tau
\end{aligned} \tag{2.27}
$$

Finally, by using (2.27) in (2.26) the signal equation can be stated in its simplest form as (2.28)

$$
s_r(t) = \int_x \int_y \int_z M_{x,y}(x,y,z,t)e^{-i2\pi[k_x(t)x+k_y(t)y+k_z(t)z]}dxdydz \tag{2.28}
$$

To put Equation (2.28) into words, the signal obtained at a time t is the Fourier transform of the transverse magnetization $M_{x,y}(x,y,z,t)$ at spatial frequency coordinates determined by the time integral of the gradient fields [36].

2.2 Pulse Sequences

Multiple pulse sequences are available for use in MRI with each sequence providing separate characteristics and capabilities. Two common families of pulse sequences are known as the spin echo and the gradient echo sequences. The spin echo sequence is produced with the use of a 90 degree RF pulse which flips the net magnetization from the longitudinal axis to the transverse plane. Following the initial pulse, the spins begin to dephase. A second pulse, normally of 180 degrees, is then applied at a time τ causing the spins to rephase. These spins rephase and produce an echo at time 2τ, also known as the echo time or TE. An example of the spin dephasing and rephasing can be seen in Figure 2.4. This echo can ultimately be read in order to obtain a signal.

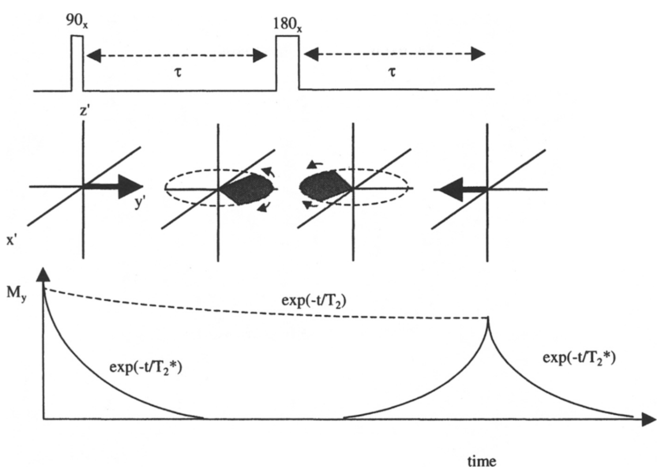

Figure 2.4: Illustration of the spin echo. The net magnetization is flipped to the transverse plan by a 90 degree pulse. It begins to dephase and is made to rephase by a 180 degree pulse at time τ. An echo is created at time 2τ. Image obtained from [67] pg 171

Once the longitudinal magnetization has been recovered, the same sequence of pulses can be applied multiple times with varying phase encodes to allow for the acquisition of different lines in k-space. The time between two excitation pulses is known as the repetition time, or the TR. An example of a spin echo sequence can be seen in Figure 2.5. Spin echo imaging allows for the acquisition of proton density weighted, T1-weighted, and

T2- weighted images.

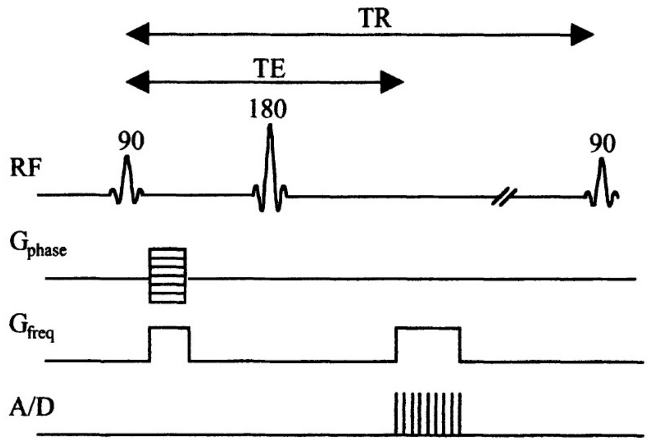

Figure 2.5: Pulse sequence diagram for a spin echo sequence that shows previously mentioned parameters such as the TE and TR. The G_{phase} and G_{freq} rows represent the phase and frequency encode gradients being turned on where as the A/D represents the signal collection at time TE. Image adapted from [67] pg 189

The signal in a typical spin echo sequence, neglecting the effect of the 180^o refocusing pulse on the z magnetization, can be expressed as Equation 2.29

$$S \propto k_p(1 - e^{-TR/T_1})e^{-TE/T_2} \tag{2.29}$$

where k_p represents the proton density. From Equation 2.29 it can be seen that the T1, T2 and PD weighting in a spin echo sequence are effected by the TR and the TE. A short TR with respect to T1, along with a short TE with respect to T2 leads to T1-weighted imaging, whereas a long TR and long TE lead to T2-weighted imaging. PD weighted imaging on the other hand can be performed with a long TR and a short TE.

Gradient echo images on the other hand use the gradient fields to obtain an echo, rather than a 180 degree pulse. Like the spin echo sequence, an initial RF pulse is used to flip the magnetization to the transverse plane. Unlike the spin echo sequence which uses normally uses flip angles near 90 degrees however, the flip angle α of the gradient sequence may be lower than 90 degrees. This allows for faster recovery of the longitudinal magnetization and thus a shorter TR is allowed. Due to the reduced TR, the scan times of gradient echo sequences tend to be lower than that of spin echo sequences. An example of a gradient-echo pulse sequence can be seen in 2.6

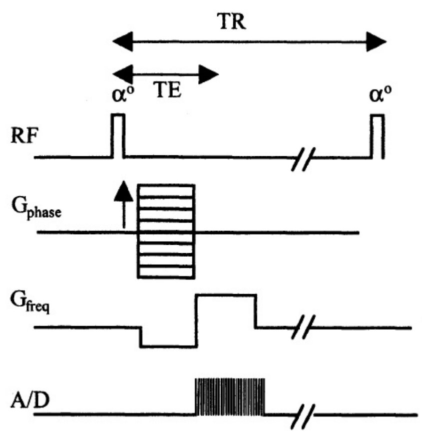

Figure 2.6: Pulse sequence diagram for a simple gradient-echo sequence. The G_{phase} and G_{freq} rows represent the phase and frequency encode gradients being turned on where as the A/D represents the signal collection at time TE. Image adapted from [67] pg 195

The signal in a gradient echo image can be described by Equation 2.30

$$S \propto k_p \frac{(1 - e^{-TR/T_1}) sin\alpha}{1 - (cos\alpha)(e^{-TR/T_1})} e^{TE/T_2^*} \tag{2.30}$$

where k_p again represents the proton density, and α the flip angle. Equation 2.30 makes the assumption that signal is gone before every subsequent excitation. This can be achieved by one of two ways. Either the repetition time, TR, can be selected such that it is much greater T2, or perfect spoiling of the magnetization can be assumed. In either case, the assumption achieves the state of all transverse magnetization being lost, resulting in all signal being gone before the subsequent excitation.

From Equation 2.30 it can be seen that the degree of T1, T2* or proton density weighting in a gradient echo sequence is determined by the TR, TE and flip angle. A short TR, along with a short TE and a large flip angle leads to T1-weighted imaging, whereas T2*-weighted imaging can be obtained with a long TR, and long TE. In this case the flip angle effects the amount of signal.

A multi echo gradient echo sequence is similar to the gradient echo sequence but rather than having one signal per RF pulse, the gradient field is used to repeatedly dephase and rephase the signal. An example can be seen in Figure 2.7. This allows of the acquisition of multiple echoes. Each echo is able to produce a separate image at different echo times. One way multi-echo imaging can provide an advantage is that all acquired echoes can be averaged leading to an improved SNR.

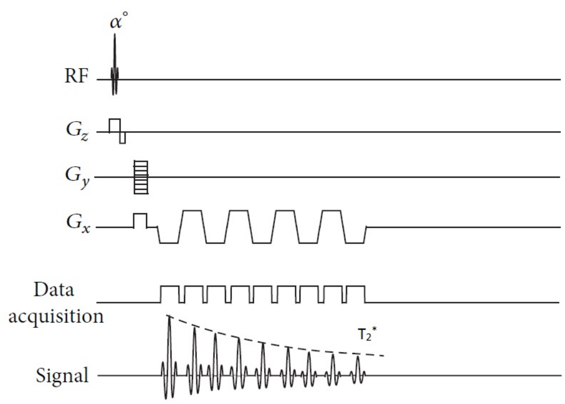

Figure 2.7: An example of a multi-echo gradient echo pulse sequence. As opposed to the collection of one image per excitation, multiple signals are collected leading to mulptiple images. Image adapted from [38].

Different materials experience varying rates of relaxation characterized by their respective T1, T2, and T2* values. This difference leads to a difference in signal intensity, which allows for contrast to be obtained. As seen in Figure 2.8, by selecting an appropriate TR or TE, the signal difference between two distinct objects can be maximized to obtain the desired contrast.

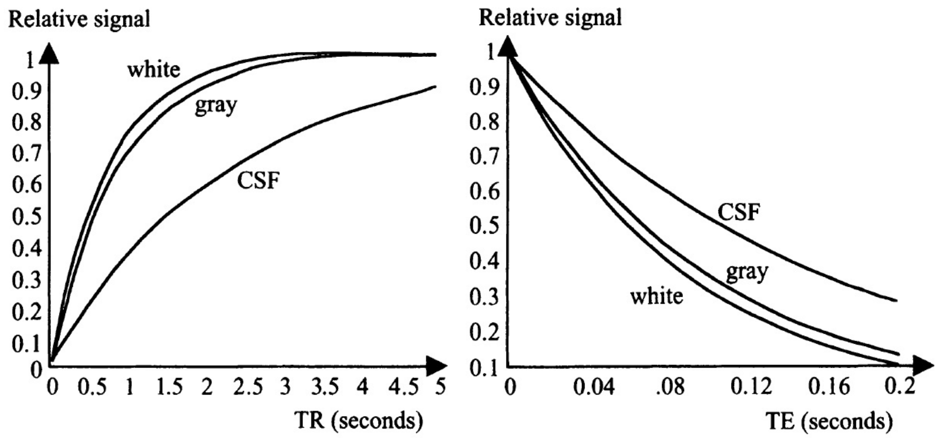

Figure 2.8: The longitudinal magnetization recovery (left) and transverse magnetization decay (right) of different material. Appropriate selection of the TR and TE can be used to obtain appropriate image contrast [67] pg 190

2.3 Radiation therapy and the role of MRI

Radiation therapy involves the delivery of a high dose of ionizing radiation to obtain tumor control while sparing healthy tissue. As precise delivery is required to minimize damage to healthy tissue, planning images are acquired prior to administration of radiation therapy. On these planning images, critical structures such as the tumor volume and the organs at risk are contoured, allowing for the creation of a treatment plan. The plan is created and optimized such that the tumor receives enough dose to achieve tumor control while the organs at risk receive as low a dose as possible to avoid complications. The treatment area is known as the planning target volume (PTV) which is encompasses the clinical target volume (CTV) which in turn encompasses the gross tumor volume (GTV). The GTV is defined as the palpable mass of the tumor as seen on the planning image. The CTV is the other hand is the region in which there is thought to be microscopic tumor growth, and this area is treated to increase the probability of tumor control. The PTV encompasses the GTV and CTV and provides a margin which account for errors in the treatment planning process [1, 27]. Improving the ability to accurately define target volumes can thus result in a reduction of the PTV and a create a more conformal treatment.

As of now the most common imaging modality used to acquire planning image data is computed tomography (CT). CT scans offer excellent spatial precision required for target delineation, along with electron density information required for dose calculations. CT scans however use ionizing radiation for the acquisition of planning images which in turn results in a deposition of dose to the patient. Along with dose deposition, the images obtained from CT scans do not display a high degree of soft tissue contrast. This causes difficulty in the localization of the tumor itself and ultimately leads to a larger uncertainty during the creation of the contours. MRI on the other hand is able to provide a high degree of soft tissue contrast, as well as functional imaging when necessary, thereby allowing for a more accurate definition of target volumes. The size of the GTV in MRI relative to that in CT has been seen to vary in literature on a site by site basis. Studies have claimed that the GTV obtained on MRI is significantly larger than those of CT in tongue, nasopharyngeal and brain tumors [2, 18, 56], whereas others have claimed that the GTV is smaller in MRI for advanced head and neck and prostate cancers [24, 42].

Regardless of the size of the tumors with respect to CT, by using MRI images for the creation of the contours not only is a more accurate target defined, but more consistent tumor volumes are obtained with reduced interobserver variability [3, 42, 68]. A more accurate contour set results in lower amounts of radiation deposited to healthy tissue and is thus safer for the patient.

Currently MRI plays a role in radiation therapy as the obtained MRI images can be used to contour the critical structures. These structures outlined on the MRI image can then be registered on to a CT image. By doing so, the contours obtained on the MRI images are transferred onto the CT images to allow for the creation of the treatment plan. This registration process however can add an uncertainty of up to 2 mm which reduces the precision of beam targeting and treatment calculations [61]. By creating a treatment plan with the use of only MRI, the registration step can be avoided leading to reduced error margins and a more conformal treatment. As an additional benefit, the patient would also be spared the ionizing radiation exposure of a CT. Doses deposited from CT can vary from 2.1 mSv for a head scan, to 31 mSv for a multiphase abdominal and pelvis scan [48]. Though the risk is small, any dose received from CT carries with it a non-zero risk. CT scans were projected to cause about 29,000 cancers for the 72,000,000 scans taken in the US in 2007 [6] .

The two biggest draw backs of MRI only treatment planning lies with the fact that MRI images are not able to provide electron density information, and experience image distortions. The image distortions need to be corrected and a method to obtain the electron density information must be implemented prior to dose calculations. One strategy used to provide electron density information to soft tissue in MRI images is known as bulk density assignment. By the application of bulk density assignment, studies have shown clinically acceptable plans can be created from MR images alone [11, 33, 57]. Dose calculations were performed by Jonsson et al., on MRI only planning images using bulk density assignment, and compared to calculations performed on CT data with inhomogeneity corrections enabled. The calculated monitor units (MU) required to deliver the 3D conformal treatment plan, in the lungs, were seen to be very similar with the maximum difference of 1.6% [28].

The feasibility of MRI only treatment plans have also been previously studied and shown to be comparable to those created with CT. When the 3D conformal treatment plans created on an MRI/CT registered image were compared to a plan created with the use of only MRI with distortion corrections, both plans were seen to be clinically acceptable with a complete coverage of the PTV by the 95% isodose line [51]. The difference between the mean and maximum dose on both plans was seen to be less than 1% whereas the difference between the dose to the isocenter and the minimum dose was seen to be 1.8% and 12.5% respectively [51]. MRI only planning is thought to have a promising future as the current limitations present in MRI guided radiation therapy are not seen to be major deterrents [39]. Not only has MRI guided radiation therapy been determined to be feasible for intensity modulated radiation therapy (IMRT), but has also been shown to be feasible for intensity modulated proton therapy (IMPT) moving forward [32].

2.3.1 MRI Pulse Sequences in Radiation Therapy Planning

A variety of pulse sequences can be used to obtain different information for radiation therapy planning images. The pulse sequence selected depends on a variety of factors such as the location of the tumor, the resolution required, the contrast, and the capability of the patient to withstand long imaging times. For example, a common sequence used for tumors in the neck are short tau inversion recovery (STIR) or T1-weighted images, whereas for perineural and skull base images T1 fat saturated images are used and T2 weighted images are typically obtained for tumors in the paranasal sinus [8].

Though there is consensus for the sequences to be used there is evidence that using new and multiple sequences pose a complimentary effect. For nasopharyngeal carcinomas, the most common sequence used to obtain images are T1-w fat saturated axial images with additional T2-w coronal and sagittal images. However, when T1-w coronal and sagittal images were added the GTV was seen to increase by 20%. Additional pulse sequences were again seen to further increase the size of the GTV. As a result, it was recommended both T1 and T2 weighted images were taken in all planes to determine the GTV for highly conformal therapies [41]. The acquisition of all these images however can lead to impractical imaging times so there is a tradeoff to be made.

The advantage of multiple sequences was also seen when T2 images were compared to Fluid Attenuated Inversion Recovery (FLAIR) images for high grade gliomas. The CTV and PTV obtain from each image showed significant variation. The overlap of the two images were seen to be 63.6% for the CTV and 82.1% for the PTV. The PTV and CTV from the two sequences were seen not to be interchangeable and could have further bearing on highly conformal treatments had only one of the sequence been used [49].

2.4 Image Distortions

As briefly mentioned in section 2.3, MRI images suffer from image distortions which may need to be corrected prior to their use in radiation therapy. There are two main types of image distortions which can cause inaccuracies in the obtained image. The image distortions are classified as either intensity non-uniformity distortions or as geometric distortions [69]. Intensity distortions cause varying intensity values at different voxels but can be corrected by the multiplication of a correction factor. This correction factor can be obtained as the determinant of the Jacobian of the distortion values [16].

Geometric distortions on the other hand are slightly more difficult to correct. Geometric distortions can be further broken down as being system-dependent or patient-dependent. The system-dependent distortions are caused by variations and imperfections of the MRI hardware whereas the patient-dependent distortions are due to patient anatomy and its effect on image acquisition. These distortions are typically on a millimetre scale, and though they may not be a problem in diagnostic images, are relevant to radiation therapy planning where spatial precision is key to target delineation [47, 69].

2.4.1 System-Dependent Distortions

The two main causes of system-dependent distortions are static field inhomogeneities and non-linearities of the gradient fields. As described in section 2.1.3, the MRI uses a static field known as B_0 to align the protons spins in order to obtain a net magnetization. This field should ideally be perfectly homogeneous to allow for a constant Larmor frequency. Following system installation however, the homogeneity of the B_0 field may remain orders of magnitude away from ideal levels. To correct for these large B_0 inhomogeneities, shimming is performed. Shimming is normally performed in 3T scanners with the use specialized shim coils within the magnet. Current is passed through these coils to carefully create magnetic fields which oppose that of the unwanted inhomogeneity. With these shim coils, inhomogeneities of several orders of magnitude can be corrected. Even with shimming however, microTesla variations in the static field causes variation of the proton Larmor frequency. This ultimately causes spins to dephase thereby leading to in-plane shifts of the apparent position of the object. The image distortions caused by the static field distortions are sequence dependent and can reduced by reduced echo times [43]. Changing the echo time affects the degree of T2 and T2* weighting in the image however, and thus may not always be appropriate. Along with field strength non-uniformities caused by MRI hardware, susceptibility differences of patient anatomy can also play a role in varying the magnetic field value at a specific location. These distortions are proportional to the static field strength while being inversely proportional to the strength of the read-out gradient. The amount of distortions can be represented mathematically as Equation 2.31.

$$\Delta x_{field} = \frac{\Delta B_0(x, y, z)}{G_{readout}} \tag{2.31}$$

In Equation 2.31, the geometric distortion Δx_{field} is determined as the quotient of the static field inhomogeneity $\Delta B_0(x, y, z)$, and readout gradient strength $G_{readout}$.

Gradient fields on the other hand are used to create a linear gradient across the imaging field of view (FOV) which causes the precession frequency to vary as a function of position. By doing so, spatial location can be determined in a given image. In a given FOV the gradient should be perfectly linear but again this is not realistic. The gradient fields are turned on and off in a very short time which causes restrictions on the length of the gradient coils and the number of turns within the coil. This causes difficulty in maintaining a linear gradient, especially at the outer edges of the FOV as seen in Figure 2.9 [65].

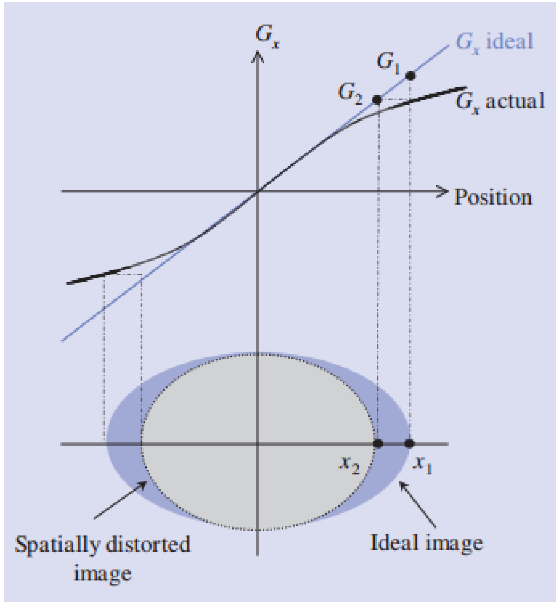

Figure 2.9: An example of gradient non-linearities distortion at the edges of the field of view. Image obtained from [35] pg 176.

As the gradient nonlinearities are the dominant source of image distortions, the degree of image distortion in an MRI tends to increase as a function of the radial distance from the isocenter [25]. These non-linearities once again cause in-plane shifts in an image given by the equation

$$\Delta x_{grad} = \frac{x * \Delta G_{read}}{G_{read}} \tag{2.32}$$

A combination of equations 2.31 and 2.9 gives an Equation for the total theoretical in-plane system-dependent distortion of a given system 2.33 [69].

$$\Delta x_{system} = \Delta x_{field} + \Delta x_{grad} = \frac{\Delta B_0(x, y, z) + x * \Delta G_{read}}{G_{read}} \tag{2.33}$$

Since every scanner has its own hardware there is variability in the distortion field seen from scanner to scanner. Different pulse sequences also show a great deal of variability in their obtained distortion fields. As such, it is recommended that the distortion fields be obtained for each scanner on site by site basis, as well as for each pulse sequence to be used [64].

2.4.1.1 Common Phantoms and Methods Used for Distortion Field Quantification

System-dependent distortions have been studied for a variety of scanners with the use of a variety of different sequences and sequence parameters. Several phantoms have been constructed for the study of these distortions, all of which contain a system of known geometry. Common phantom designs follow that outline by Wang et al., which uses square grid sheets aligned in parallel in the z direction. This allows for the creation of an array of 3D control points which can be defined at the intersection of the grid lines at each surface of the sheet [65]. The application of the phantom described by Wang et al, depends on the dimensions of tank used during construction. With appropriate dimensions, the phantom can be used for head volume or pelvis volume imaging.

Another commonly used phantom is known as a linear test object as outline by Tanner et. al. Three sets of water filled, orthogonal PMMA rods are mounted perpendicular to the three imaging planes. This again allows for the creation of control points at the intersection of the three sets of tubes [16, 55]. These phantoms are typically large volume phantoms used for pelvis volume imaging.

Additionally, phantoms have been designed with spherical balls [62] placed in a cubic pattern in a copper-sulfate solution, or vitamin D capsules [60] placed at defined locations in polyurethane foam. Upon imaging, the glass balls and vitamin D pills then act as the control points for the characterization of the distortions. Much like the linear test object these phantoms are used for large field imaging.

Two main methods are commonly used to quantify MR image distortions. The first method involves the comparison of control point positions on MR images to undistorted CT images [5, 10, 13, 50]. The difference in the position of the control points allows for the quantification of the distortion field. The second method is the use of deformable registration to register the MRI image to an undistorted CT, resulting in the production of a deformation field [34, 53]. The deformation field produced by the registration is taken to be the quantification of the distortion field.

2.4.1.2 Relevant studies in system-dependent distortions

Weygand et al., summarized 10 studies of system dependent image distortion. In these studies, it was seen that 19 of 29 measurements showed distortions greater than the 2 mm precision required for radiation therapy [69]. The same authors reported that as technology advances, the system integrated distortion correction algorithms continue to improve resulting in reduction of the maximum distortions seen throughout time.

Of specific interest in the studies listed by Weygand et al., Sun et al. used a 3 T Skyra scanner, a PMMA phantom, and a T2*-GRE sequence to study the effect of vendor provided distortion corrections. They found a maximum distortion of 7.5mm, 2.6 mm and 1.7 mm for a pelvis sized phantom with no distortion correction, 2D distortion correction and 3D distortion correction respectively [53].

Baldwin et al., on the other hand determined the distortion field on a 3 T Ingenia MRI using a gradient echo sequence and a phantom made of PMMA and polystrene similar to that proposed by Wang et al., [65]. They found that when a slice was taken at the isocenter of the MRI, a maximum distortion of 4.5 mm was seen in the top corner of the image. Not only that but they were also able to separate the distortion into gradient nonlinearity based distortions, and those caused by B_0 inhomogeneity. This was done through use of the reverse gradient technique [4, 5]. As distortions caused by static field inhomogeneities are only present in the frequency encode direction, two images were obtained with reversed frequency encode polarities. The reversal of the polarity causes the direction of the static field inhomogeneity distortions and susceptibility distortions to be switched. By then taking the average of the two distortion fields, the distortion caused by the gradient nonlinearities were isolated. This was also referred to as sequence independent distortions [4, 5]. Baldwin et al., found that the gradient nonlinearity distortions were the dominant source of distortions and that the B_0 inhomogeneity distortions were only predominant in the extremity of the image in the transverse plane [5].

Walker et al., determined the radial distance at which an average distortion of 2 mm was seen, to determine acceptable volumes for radiation therapy planning [64]. They were able to determine that for prostate and cervical cancer regions an acceptable radial distance could extend beyond 200 mm. For head cases however, they suggested that the acceptable radial distance be limited to below 150 mm. They also suggested that geometric distortions during radiation therapy planning would have the greatest effect for breast and lung cases due to their positioning in the MR, and the air-tissue interface in the lung [64].

2.4.2 Patient-Dependent Distortions

Along with system-dependent distortions, there are also the object-dependent distortions such as the chemical fat-water shift and distortions caused by large susceptibility changes. The chemical shift distortions are caused by the fact that the fat and water molecules have a slightly different resonance frequency. The difference in resonance frequencies is due to their different chemical environments, which leads to varying levels of magnetic shielding. This causes difficulty localizing them using spatial encoding, and results in fat being slightly shifted in the frequency encode direction. The chemical shift can be reduced however by varying pulse sequence parameters and pulse sequence elements during image acquisition. For example, the use of a larger receive bandwidth, smaller FOV [37], and fat saturation techniques [14] all work to reduce the amount of distortions caused by chemical shifts in the image.

The difference in the magnetic susceptibility of materials in the body is also able to cause distortions. The magnetic susceptibility is a property of a material which determines its tendency to become magnetized once placed in a magnetic field. Objects are separated into three separate classifications which depend on their susceptibility value χ. Diamagnetic objections have a χ value less than 0, whereas ferromagnetic objects have a χ values greater than 10^{-2}. Objects with χ between 0 and 10^{-2} are known as paramagnetic. When placed in a magnetic field, ferromagnetic objects are strongly magnetized and paramagnetic objects are weakly magnetized in the direction of the magnetic field. Diamagnetic objects on the other hand become magnetized in the direction opposing that of the magnetic field.

A material with a susceptibility of χ perturbs the static field to produce a field given by the equation

$$B_{0,perturbed} = (1 + \chi)B_0 \tag{2.34}$$

Since the magnetic field becomes perturbed, the Larmor frequency changes. As such, distortions caused by magnetic susceptibility work fundamentally in the same way as static field inhomogeneity distortions. Susceptibility distortions tend to occur in areas with two materials of highly varying susceptibility values as these variations cause perturbations in local magnetic field. They can occur throughout the body and mostly occur at tissue-air interfaces as water has a susceptibility of $\chi_{water} = -9 \times 10^{-6}$ and air a susceptibility of $\chi_{air} = 3.6 \times 10^{-7}$ relative to vacuum. In head and neck patients the susceptibility changes begin to play a large role in creation of distortions due to air bone interfaces found in areas such as the nasal sinuses, and the ear canals [66]. Susceptibility distortions are also greater in higher field strengths, and greater in gradient echo sequences as opposed to spin echo sequences [19]. These distortions have the ability to cause both slice position errors and in-plane errors to which the magnitude can be represented as Equation 2.35 [44]

$$\Delta x = \Delta\chi \frac{B_0}{G_{read}} \tag{2.35}$$

Additionally, if the B_0 map is obtained, the expected distortions can be calculated as seen in Equation 2.36

$$\Delta x = \frac{\Delta B_0}{BW_f} \Delta V_f \tag{2.36}$$

where ΔB_0 is the static field inhomogeneity in Hz, BW_f the bandwidth used during image acquisition in Hz/pixel, and ΔV_f the dimension of the pixel in the frequency encode direction [66].

2.4.2.1 Relevant studies in patient-dependent distortions

Studies of patient-dependent distortions are much more scarce than those of system dependent distortions. This is in part due to the high variability of patient dependent distortions as they can vary significantly from patient to patient or day to day. A few studies have used simulated susceptibility distortions in order determine their severity at different interfaces [5, 52, 63].

The largest distortion caused by susceptibility difference was always seen to be at interfaces between air and soft tissue. Maximum distortions of 3.34 mm and 4.37 mm were seen in the lung for a 3 T bore type MRI and biplanar MRI respectively [52]. Simulations were also performed to determine the susceptibility distortions in a 1.5 T bi-planar magnet in a MR-linac, and maximum distortions of 2.6 mm and 2.5 mm were seen for the lung and prostate respectively [63]. The susceptibility distortion in the brain on the other hand were seen to be 0.57 mm for a 0.5 T bore type MRI [52] and 0.3 mm for the simulation of the 0.2 T rotating magnet [63].

Wang et al, also determined the expected patient-dependent distortions for 19 brain tumor patients on a 3 T scanner. Using B_0 field distortion maps and Equation 2.36 they calculated that in a 3D T1 weighted image 86.9% of the distortions were below 0.5 mm, 97.4% below 1 mm and only 0.1% above 2 mm. The maximum distortion they observed remained below 4 mm. The maximum distortions once again occurred at air-tissue boundaries, with the largest amount of distortions being seen around the sinuses, followed by the ear canal [66].

From a more technical point of view, Baldwin et al., determined the distortions caused by the susceptibility differences of mineral oil and a polystyrene grid phantom. The distortions were seen to be subpixel in magnitude with a value of 0.49 mm [5]. The susceptibility values of mineral oil and polystyrene are much closer than that of air and water, thus producing smaller distortions than those expected in patients.

2.4.3 Bandwidth, SNR and Distortions

Multiple aspects determine the amount of distortions present in an MR image. The bandwidth, slice thickness, pulse sequence, scanner hardware and direction of the phase encode all play a role in the amount of observed distortion, making the fundamental characterization of the problem difficult. The amount of distortion present also increases with increasing radial distance from the isocenter as the gradient field linearity and static field homogeneity are reduced. A very common way of reducing image distortions is by increasing the bandwidth used to acquire the image. It has been seen that a 10 times increase in the bandwidth has the ability to reduce the average distortion by 1 mm and the maximum distortion by 3 mm [64]. Though increasing the bandwidth provides a decrease in distortions, it comes at the cost of SNR. The SNR is related to the bandwidth by the equation

$$SNR \propto \frac{1}{\sqrt{Bandwidth}} \tag{2.37}$$

Due to the loss of SNR, there is typically an upper limit on the bandwidth that can be used during image acquisition. One suggestion to improve the SNR while using a high bandwidth is through signal averaging as decreased resolution or increased voxel volume is largely undesirable. Multiple excitations can be used to acquire multiple images with a high bandwidth. These images can then be averaged leading to an increase in the SNR. Signal averaging has a theoretical SNR increase as seen in Equation 2.38, but is limited by the fact that the imaging time is proportional to the number of signals averaged (NSA).

$$SNR \propto \sqrt{NSA} \tag{2.38}$$

As opposed to conventional signal averaging, multi-echo averaging also offers the possibility of increasing SNR for high bandwidth image acquisitions [23, 30]. Multi-echo averaging involves the acquisition of multiple images per excitation at different echo times. These echoes can then be averaged to improve the SNR. Though the TR must be increased to allow for the acquisition of additional echoes, as the measurement does not need to be repeated multiple times as in conventional signal averaging, a decrease in the scan time may be obtained.

2.4.4 Distortion Corrections

Vendors provide correction algorithms which attempt to correct geometric distortion through post-processing, using known information about the particular scanner. These algorithms correct system-dependent distortions but are unable to account for distortions on a patient to patient basis without additional information. A common method by which gradient fields distortion are corrected are through the use of spherical harmonics [21, 26, 54]. The specifics behind these correction algorithms however depend on the vendors themselves as different vendors provide algorithms that work in different ways. For example, on specific GE scanners a 2D correction algorithm is provided, along with a 3D correction which only functions if the 2D correction is also on [60]. Philips scanners on the other hand are able to perform 2D and 3D corrections independently. In all cases, the vendor corrections provide significant improvement in the image quality and should be turned on for all radiation therapy imaging purposes [29, 60, 64].

Chapter 3

Methods

This thesis had two major objectives as pertaining to the use of MRI in radiation therapy. The first of which, outlined in section 3.1, was the use of a pelvis sized grid phantom in order to quantify system dependent image distortions. These distortions were measured as a function of the radial distance from the isocenter, allowing for the determination of the radial distances which have image distortions less than the tolerance of 2 mm. The second objective, outline in section 3.2, was a study of the susceptibility induced image distortions as well as the effects of multi-echo averaging on image quality in a healthy human volunteer. First, simulations were performed to determine the regions of expected high susceptibility induced distortion. These regions were then observed qualitatively and the bandwidth was increased, at the cost of SNR, to reduce the present distortions. Multi-echo averaging as well as conventional signal averaging was then performed and compared in their ability to regain the SNR loss, their ability to maintain CNR, and their overall image quality.

3.0.1 Definition of Coordinate System

As this project involved the acquisition of both phantom and in-vivo data, the DICOM standard coordinate system was set-up as seen in Figure 3.1 and held constant for all data sets. For both phantom and in-vivo images, the z direction was defined as the axis into the bore and as such was synonymous with the SI direction. The x axis was synonymous with the LR direction and the y axis was synonymous with the AP direction. As all images were acquired in the axial plane as is customary for radiation therapy, the xy-plane was referred to as inplane, whereas the z direction referred to as through plane. These terms are used interchangeably for the remainder of this thesis. The phase and frequency encodes directions were in either of the x or y directions depending on the pulse sequence used.

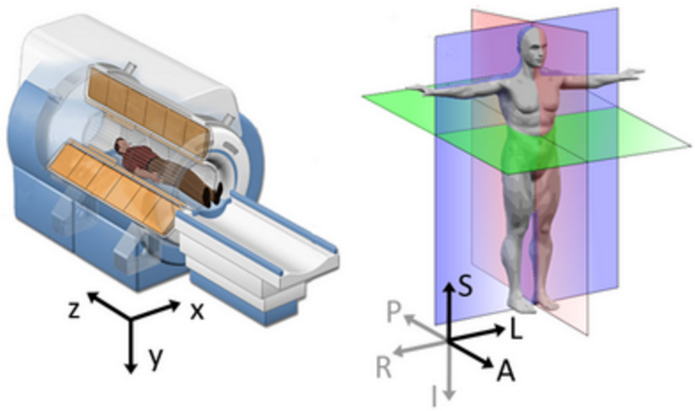

Figure 3.1: The coordinate system used for all phantom and in-vivo measurements. MRI coordinate system. (2017, July) 3D Slicer Coordinate System. [Online]. https://www.slicer.org/wiki/Coordinate_systems.

3.1 System-Dependent Distortion Quantification Using Grid Phantom

The following section outlines the methods related to the first major objective of this thesis. A grid phantom was constructed and used to determine system-dependent distortions. First the B_0 homogeneity was measured to ensure reproducibility of the B_0 field. The distortions were then measured for multiple clinically relevant pulse sequences. Additionally, the effect of the bandwidth value was also studied in order to determine its effect on the obtained distortions, and distortion reproducibility was measured. Finally, the sequence independent distortions were determined.

3.1.1 Grid Phantom Materials and Dimensions

A grid phantom was created in-house similar to that outlined by Wang et al, [65] and can be seen in Figures 3.2 and 3.3. Four sets of spacers, placed at the top and bottom of the grid sheets, were used in order to hold mesh grid sheets in place at intervals of 0.64 cm. The spacers and sheets were placed in a tank which had dimensions of roughly 40 cm by 27.31 cm by 52.71 cm. The grid intersections were roughly 1.58 cm from each other in the x and y directions with a 0.79 cm separation in the z direction. The tank was made of polymethyl methacrylate (PMMA), whereas the spacers and grid were made of polyethylene. The susceptibility values of polyethylene and PMMA are rare in literature and can vary depending on the density of the plastic. Values of -9.01 ppm and -9.47 ppm were taken respectively with respect to water as a reference [9]. As the two materials have similar susceptibility values, large susceptibility distortions are avoided.

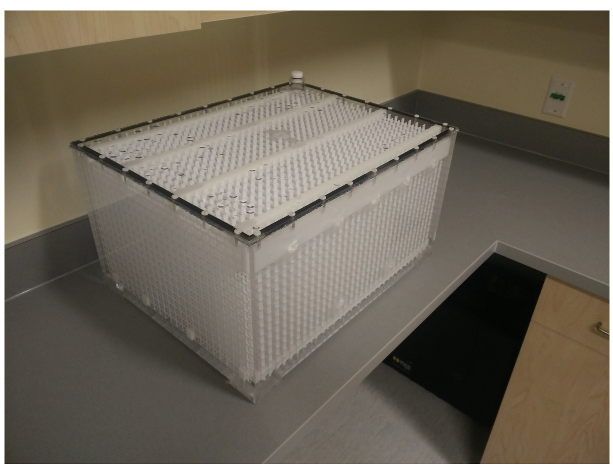

Figure 3.2: The grid phantom built in-house to determine the distortion field

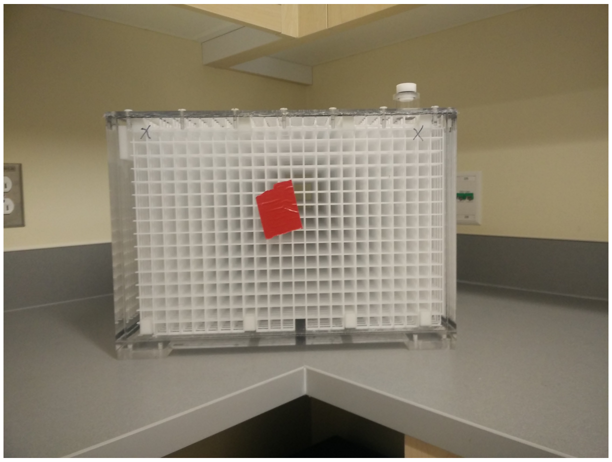

(a)

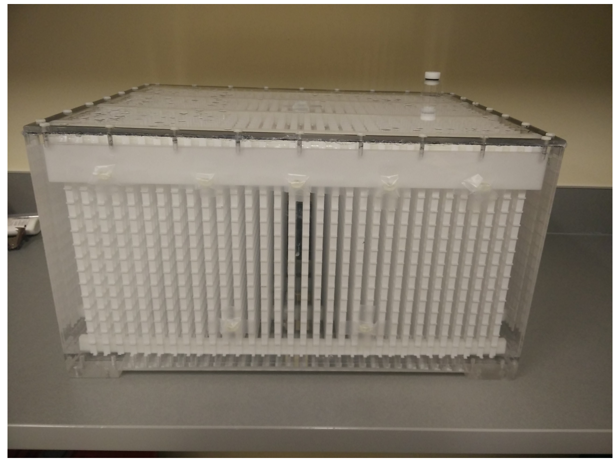

(b)

Figure 3.3: The (a) front and (b) side view of the phantom showing the spacings involved in the grid sheets

The phantom was then filled with mineral oil in order to produce signal within the phantom, as well as reduce artifacts caused by the B_1 pulse. The resonant RF wavelength of B_1 pulse in water is roughly 26 cm which was similar to the dimension of the tank. This similarity can lead to negative RF interference within the phantom. The interference in turn leads to inhomogeneities of the RF field with up to complete cancellations in certain areas. The inhomogeneities then cause irregular flip angles throughout the phantom causing what appear to be intensity artifacts [45]. With the use of mineral oil, the RF resonant wavelength becomes roughly 160 cm and the interference is no longer an issue as shown in Figure 3.4.

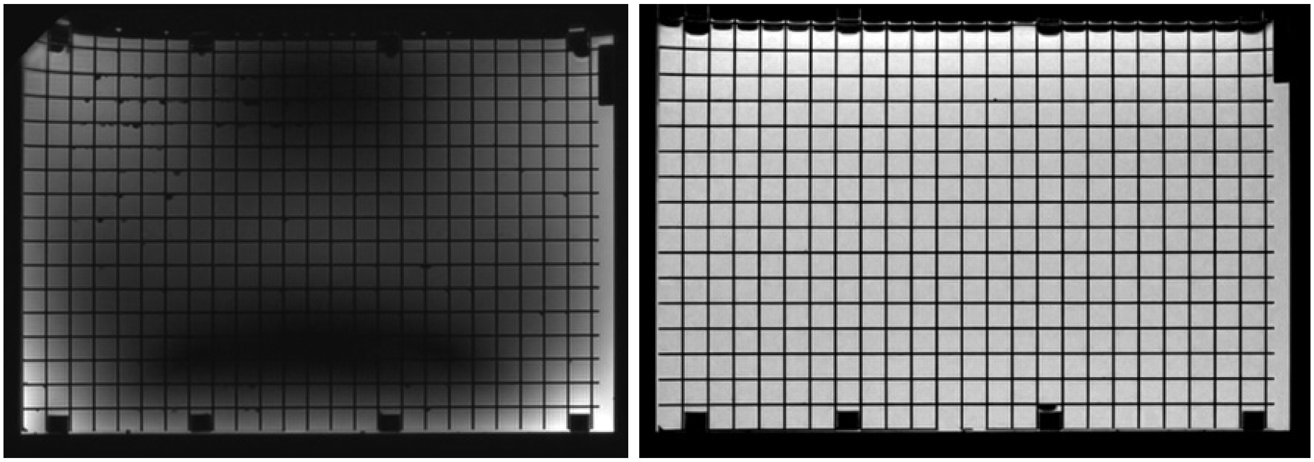

(a) **(b)**

Figure 3.4: (a) Axial slice of the grid phantom when filled with water, 270 g of salt and roughly 50 mL of Gadovist. (b) Same axial slice of phantom filled with mineral oil.

One face of the tank was marked as the head and vitamin E pills were taped to the sides of the phantom in order to help with alignment. In addition to aiding with alignment, the vitamin E pills also helped to determine the orientation of the phantom during the registration process.

3.1.2 Phantom Imaging

3.1.2.1 Computed Tomography

A helical CT head scan (Brilliance Big Bore CT, Philips Healthcare, Eindhoven, The Netherlands) was performed on the phantom at a kVp of 120, to act as the gold standard. The CT image is an acceptable gold standard image as no uncorrected distortions should be present in an x-ray projection image of the phantom. A scan was initially obtained of the unfilled phantom using an in-plane pixel size of 1.17 mm * 1.17 mm and a slice thickness of 0.8 mm. A second CT was then obtained once the phantom was filled, with an in-plane pixel size of 1 mm * 1 mm and a slice thickness of 0.8 mm. Due to a loss of contrast at the grid caused by the mineral oil, the empty CT image was used as the reference moving forward. To account for any minor motions of the grid during the filling process, as well as to provide a more desirable voxel size of 1 mm * 1 mm * 0.8 mm, the empty CT image was linearly registered to filled CT image.

3.1.2.2 Magnetic Resonance Imaging

All phantom MR images were obtained on a 3 T scanner (Ingenia, Philips Healthcare, Eindhoven NL). The vitamin E pills on the grid phantom were used to help with the alignment within the MR. The lasers on the MR, along with a predetermined location near the vitamin E pill, were used to ensure the orientation of the phantom was consistent for all following scans. Parallel imaging was turned off for all the following scans unless stated otherwise.

3.1.2.3 B0 Mapping

The B_0 inhomogeneity was obtained on different days to determine the effect of phantom positioning and B_0 shimming on the reproducibility of the B_0 field. Much like the magnitude images, used most commonly for viewing anatomy, the MR is also able to produce phase images. The phase, ϕ, is those of the spins which precess at the Larmor frequency, and are sensitive to variations in the B_0 field. The phase images used to determine the B_0 inhomogeneity were obtained using a multi-echo gradient echo sequence optimized for phase imaging. This sequence was named, and will referred to in this thesis as, the SWIp-QSM sequence. The SWIp-QSM sequence was performed with 3 echoes at echo times of 2.78, 5.57, and 8.36 ms. This sequences used a TR of 10.9 ms with a 20°flip angle, and a 1.5 mm isotropic voxel size.

The phase images obtained from the scanner are wrapped $(-\pi \leq \phi < \pi]$ resulting in discontinuities in the images. These images must therefore be unwrapped in order to determine the B_0 homogeneity. The phase images of the phantom were spatially unwrapped using a quality guided approach [20]. Following spatial unwrapping, temporal phase wrapping was observed in the second and third echo. Two pi was added to every voxel in the second and third echo, resulting in a manual temporal unwrapped image. The final phase unwrapped images were used to obtain B_0 maps in units of radian per second. Given the Larmor equation as seen in Equation 2.9, the angular frequency was then divided by the gyromagnetic ratio to obtain the B_0 inhomogeneity, which were then converted to ppm. The B_0 inhomogeneities were then compared to determine whether the B_0 inhomogeneity distortions would vary from day to day.

3.1.2.4 The Effect of Vendor Corrections on Measured Distortions

The effect of the provided vendor corrections was tested on the T1-w 3D gradient echo. The sequence used to perform these tests was a single echo gradient echo sequence, using only 1 signal average. The flip angle was set to 12°, with a TR of 5.05 ms, and a TE of 3.00 ms. The resolution of all performed scans were 1 mm * 1 mm * 1.5 mm, with a 300 mm AP, 450 mm RL and 250 mm SI field of view. The AP direction was used as the frequency encode direction, whereas RL was the phase encode direction. Three sets of images were obtained, one which had no vendor correction, one with the corrections set to ”2D compensation”, and the other with the correction set to ”3D compensation” as provided by the vendor.

Post processing was then performed, as detailed in section 3.1.3, and deformation fields were obtained in all three axes. These three deformation fields were used to calculate the total distortion values as seen in Equation 3.1

$$D = \sqrt{\Delta x^2 + \Delta y^2 + \Delta z^2} \tag{3.1}$$

where D was the total displacement and Δx, Δy, and Δz were the displacement in each respective direction. The average distortion as a function of radial distance from the isocenter was then obtained for each correction algorithm and compared. These average distortion values were calculated for a 1 mm range at 1 cm intervals. Comparisons were made for the average total displacement value in all directions, as well as the average distortion in each direction.

3.1.2.5 Distortion Fields of Clinically Relevant Sequences

The distortions present in four clinically relevant pulse sequences were then examined. The first sequence used was a T1-weighted 3D gradient echo used primarily in our institution for brain and pelvis imaging. Distortions in a T1-weighted 3D spoiled turbo gradient echo, referred to by Philips and in this thesis as the THRIVE sequence, was also examined. The THRIVE sequence uses a 180°inversion pulse prior to the excitation pulse to allow for fat signal suppression. This sequence is typically used in our institution for post contrast imaging in non-brain regions, and in head and neck cases. The two final sequences used were a T2-weighted 2D spin echo sequence used primarily in our institution for pelvis imaging, and a T2-weighted 3D spin echo sequence used for head and neck as well as pelvis imaging. The pulse sequence parameters can be seen in Table 3.1.

Table 3.1: Parameters of the four clinically relevant sequences used to determine distortion fields.

Sequence	**TR** [ms]	**TE** [ms]	**Flip angle** [°]	**ETL**
T1-w 3D Gradient Echo	5.05	3.00	12	1
T1-w THRIVE	7.71	3.70	10	1
T2-weighted 2D Spin Echo	4889	100	90	17
T2-weighted 3D Spin Echo	1800	245	90	81

All images were obtained using their default correction algorithms, meaning ”2D compensation” for 2D sequences and ”3D compensation” for 3D sequences. The resolution used was 1 mm * 1 mm * 1.5 mm for all sequences except the THRIVE sequence which used a resolution of 1 mm * 1mm * 0.8 mm. All other sequences had a reduced resolution with respect to the gold standard CT image due to time limitations of the scan. Though the other sequences had larger slice thicknesses, a slice thickness of 1.5 mm was selected to be acceptable as this was relevant to clinical scans. Again a 300 mm AP, 450 mm RL, and 250 SI field of view was used for all images. The AP direction was the frequency encode direction, with the RL direction being the phase encode direction for the T1-weighted 3D GRE, T2-weighted 2D SE, and T2-weighted 3D SE sequences. The RL direction was the frequency encode with the AP direction being the phase encode direction for the THRIVE sequence.

Post processing was then performed, as detailed in section 3.1.3, and deformation fields were obtained in all three axes. These three deformation fields were used to calculate the total distortion values as seen in Equation 3.1. In addition to the average distortion as a function of radial distance from the isocenter, the distortions were separated into those in the phase encode, frequency encode, and through plane directions individually and compared for each sequence.

Once the distortions were characterized as a function of radial distance from the isocenter, an acceptable radial distance for radiation therapy planning was determined for each sequence. This radial distance was determined as the radial distance at which the average distortions were 2 mm.

3.1.2.6 Reproducibility of the Distortion Measurements for the T1-weighted 3D GRE Sequence

The reproducibility of the distortions obtained in the T1-weighted 3D gradient echo sequence were then examined. T1-weighted 3D gradient echo images were obtained three times over the course of roughly two weeks. All parameters used were held identical for each test. The flip angle, TR and TE were maintained the same as shown in Table 3.1, being set to 12°, 5.05 ms, and 3.00 ms respectively. All tests again used a resolution of 1 mm * 1 mm * 1.5 mm for field sizes of 300 mm AP, 450 mm RL, and 250 SI. Post processing was then performed, as detailed in section 3.1.3, and deformation fields were obtained in all three axes. These three deformation fields were used to calculate the total distortion values as seen in Equation 3.1. The total distortions as well as the distortion in the x, y, and z directions were compared between all acquired images.

3.1.2.7 Effect of MRI Slice Thickness Interpolation on Distortion Field Measurement

Though the MR images were acquired with a 1.5 mm slice thickness, they were interpolated down to images of 0.8 mm slice thickness during the linear registration. This was due to the fact that the gold standard CT image had a slice thickness of 0.8 mm. The CT images where obtained with the smallest possible slice thickness in order to accurately capture the warping of the grids at each surface. The effect of having a different slice thickness for

MR and CT, along with the ability of the registration software (MIMVista, MIM Software, Cleveland, USA) to interpolate the distortion field for varying MR slice thicknesses, were then examined.

The T1-w 3D gradient echo was once again used to acquire the images. The in-plane resolution was maintained as 1 mm * 1 mm while different images were taken with slice thicknesses of 2 mm, 1.5 mm, 1.25 mm and 1 mm respectively. The field of view was maintained as 300 mm AP, 450 mm RL, and 250 SI for all image acquisitions.

Post processing was then performed, as detailed in section 3.1.3, and deformation fields were obtained in all three axes. These three deformation fields were used to calculate the total distortion values as seen in Equation 3.1. The distortion as function of radial distance from the isocenter was once again examined to determine the effect of varying the MR slice thickness.

3.1.2.8 Distortions Fields for Varying Bandwidths

The readout bandwidth was then manipulated to determine its effect on the observed distortions. The theoretical relation between the bandwidth, SNR and the amount of observed distortion is described in section 2.4.3.

The T1-weighted 3D gradient echo was once again used to observe the effect of different bandwidth. As the Philips software allows for control of the bandwidth through the amount of the desired water-fat shift, the water-fat shift was manipulated for different image sets. Images were obtained at the maximum allowable water-fat shift, a water-fat shift of 1.4 pixels, a water-fat shift of 1 pixels, a water-fat shift of 0.7 pixels as used in standard 3D GRE imaging, and the minimum allowable fat shift. These corresponded to bandwidth per pixel values of 244, 309, 434, 617, and 926 Hz/pixel respectively. All other parameters were kept consistent to the previously performed tests. The resolution was once again 1 mm * 1 mm * 1.5 mm, for a field size of 300 mm AP, 450 mm RL, and 250 SI.

Post processing was then performed, as detailed in section 3.1.3, and deformation fields were obtained in all three axes. These three deformation fields were used to calculate the total distortion values as seen in Equation 3.1. The total distortion, as well as the distortion in all three axes individually, were compared to determine the effect of the bandwidth on the radial distance from the isocenter acceptable for radiation therapy planning.

3.1.2.9 Imaging for Sequence Independent distortions

The sequence independent distortions were then determined using the T1-w 3D gradient echo sequence. An image of the phantom was obtained with parameters as in Table 3.1. A second set of images was then acquired of the phantom, with identical sequence parameters, but with the polarity of the frequency encode direction in the opposite direction. On the Philips 3T Ingenia, the polarity of the frequency encode direction is set through the selection of the direction of the water-fat shift. For the two acquired image sets, the water-fat shift was set to anterior then posterior respectively.

3.1.3 Post Processing

3.1.3.1 Image Registration to Obtain Distortion Field

A central portion of the grid phantom on the MR images were identified such that the entire grid could be seen, with minimal signal loss at the corners. This corresponded to roughly the central 20 cm of the phantom in the SI direction. The gray scale MR images were linearly registered to the CT images with the use of a commercially available package (MIMVista, MIM Software, Cleveland, USA). An affine transformation was performed to correct the scaling, translation, shear, and rotation of the image. Once the images had been registered, the CT and registered MR images were cropped in order to isolate the grid as shown in 3.5.

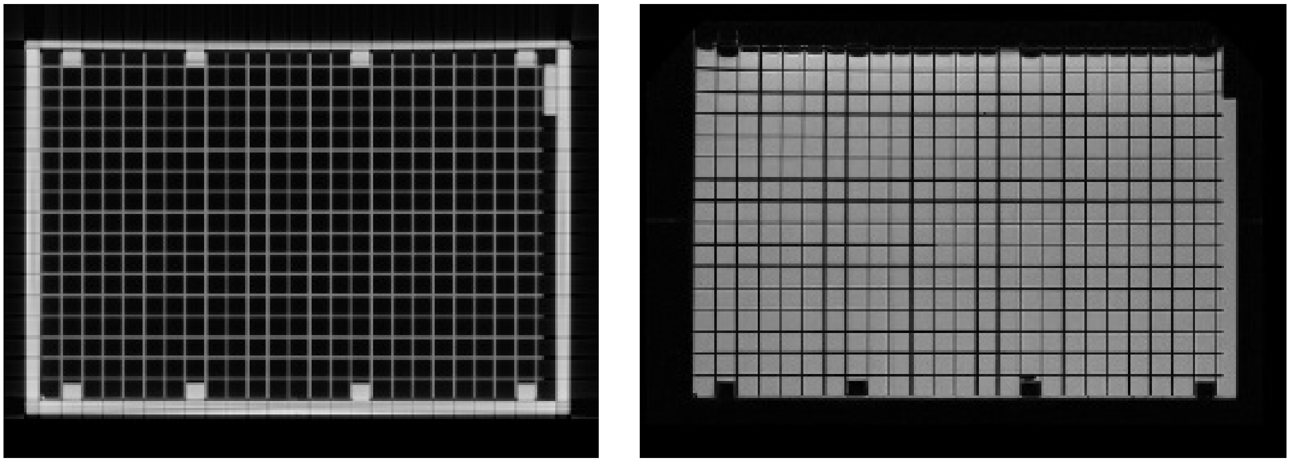

(a) CT slice of the phantom **(b)** MRI slice of the phantom

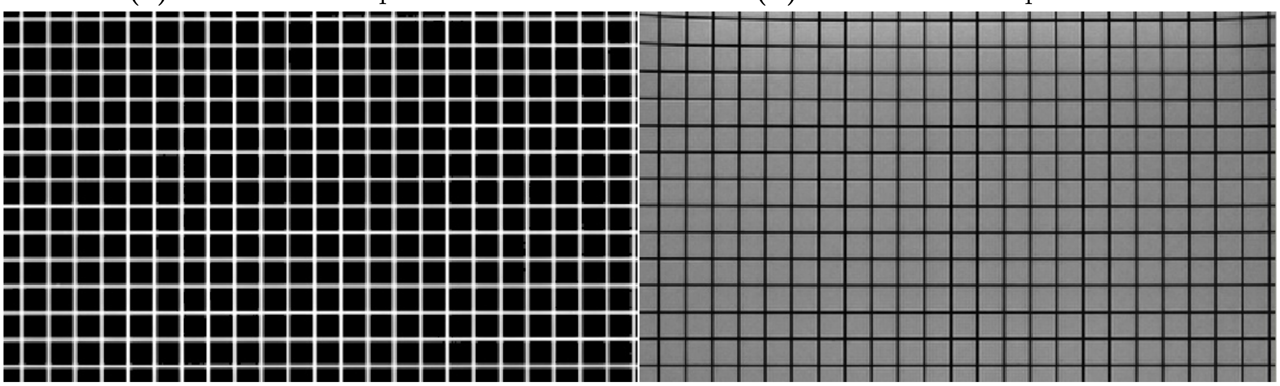

(c) CT slice of the phantom cropped to isolate the grid

(d) MRI slice of the phantom cropped to isolate the grid

Figure 3.5: The linearly registered images were cropped in order to isolate the grid. The isolated grid was the region used for the non-linear registration methods in order to obtain the distortion field

Once the images were cropped, the cropped CT image was processed with the use of MATLAB to improve the contrast of the grid. First, an image sharpening was performed using the unsharp masking method (imsharpen) in order to obtain improved contrast between the grid and the background. Histogram spreading (imadjust) was then performed on the sharpened image to further enhance the contrast. The histogram spreading allowed for the mapping of the image histogram between the highest and lowest value of the brightness scale, with 1% of the image being saturated at the lowest and highest points. The effect of both these methods on the image and its histogram can be seen in Figure 3.6.

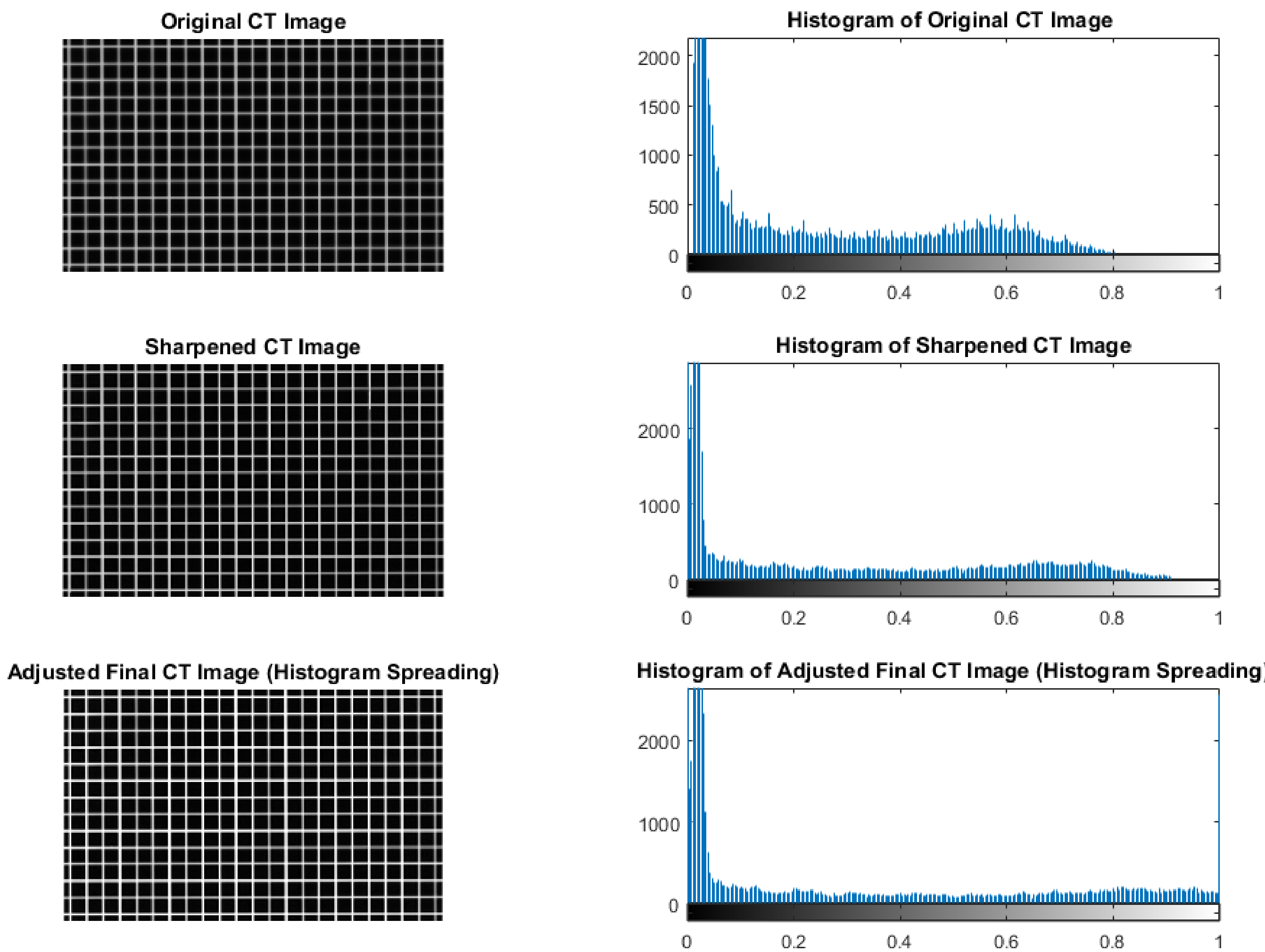

Figure 3.6: Image sharpening as well as histogram spreading was performed on the CT image to increase the contrast of the grid.

Following the processing of the CT image, the MR images were then manipulated to make them appear similar to CT images as seen in 3.8. First, as the signal was produced from the oil in MR as opposed to the grid in CT, the MR image was inverted. This caused the grid to appear bright in the MR image and the oil to appear dark.

To further increase the similarity of the two sets of images, a histogram equalization was performed between the cropped CT images and the cropped registered MR images. Histogram equalization matches the image histogram of the input image, MR, to that of the image histogram of the target image, CT. The effect of the histogram equalization can be seen in Figure 3.7.

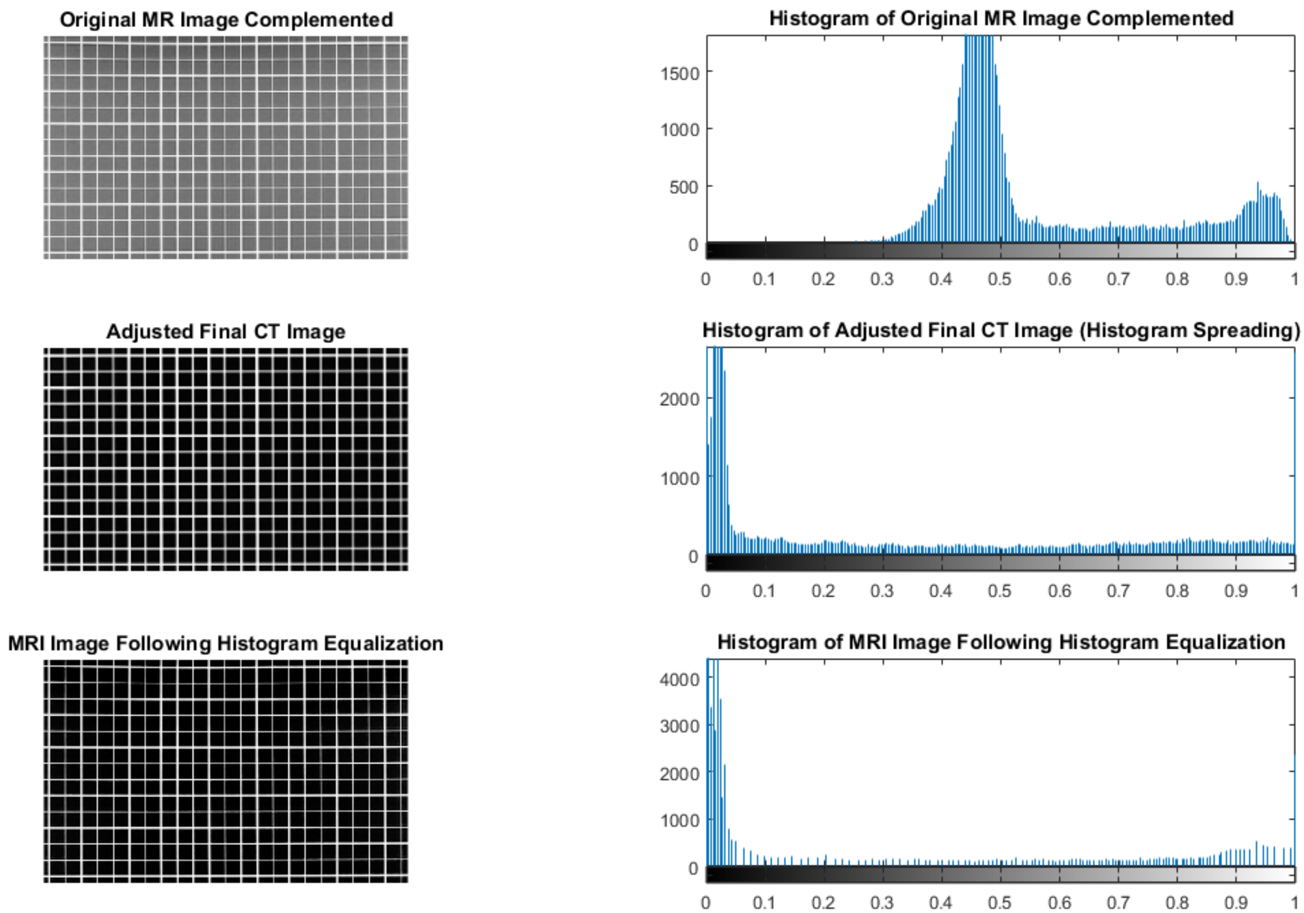

Figure 3.7: A histogram equalization was performed on the complemented MR image to make it look similar to the CT image.

The edges were then again enhanced on the MR images, and a histogram spreading was once again performed. Finally, a threshold was then performed for the CT and MR images to remove small gray regions between the grids caused by the histogram equalization. By performing all of the previous steps, the appearance of the modified MR image was very close to that of the processed CT image which allowed for the use of a monomodal nonlinear demons registration (imregdemons implemented in MATLAB, The Mathworks, Natick, USA). A demons registration is a grey-scale based registration algorithm in which the moving image is deformed to match that of the fixed image. The voxels in the static image are used to compute local forces that displace voxels of the moving image. Each pixel has an associated displacement vector and the moving image is iteratively deformed by applying a displacement vector to each pixel to match the static image [22, 58, 59]. A monomodal registration was performed as opposed to a MRI to CT multimodal nonlinear registration due to considerably shorter computational times.

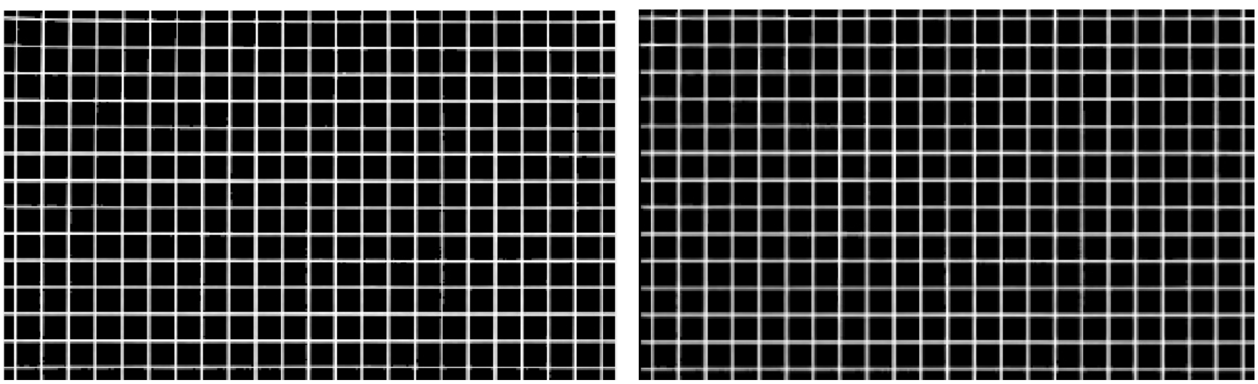

(a) **(b)**

Figure 3.8: (a) The MR image seen in 3.5 following the image processing make it appear similar to the CT image (b) The final image following the nonlinear registration of the cropped, and processed MR image to the cropped CT image

During the creation of this final registered image, displacement maps were also produced. These maps displayed the pixel by pixel displacement of the CT image to obtain the MR image, thereby giving a measure of the distortion field.

3.1.3.2 Additional Post Processing for Sequence Independent Distortion

As the sequence independent distortion measurement used two sets of images, with a reversed polarity in the frequency direction, an additional post processing step was required. The distortion field in the frequency encode, phase encode and through plane directions were averaged. The frequency encode polarity reversal should act to reverse the direction of the distortion in the frequency encode direction. Therefore by averaging the two distortion fields, the sequence independent distortions are isolated.

3.2 Patient-Dependent Distortions and Multi-Echo Gradient Echo Image Quality Assessment

The following section outlines the the methods used to achieve the second major objective of this thesis. Patient dependent distortions were simulated in a healthy volunteer, and areas of high expected distortions were observed. The bandwidth was increased to reduce the observed distortions and multi-echo averaging, as well as conventional signal averaging, was used to regain the lost SNR. The images produced by the multi-echo averaging and conventional signal averaging were then compared in ability to regain the SNR, ability to maintain CNR, and their overall image quality. All data were acquired using a multi-channel receive-only head coil. The study was approved by the Research Ethics Board of the McGill University Health Centre, and informed consent was obtained.

3.2.1 In-vivo Distortions and the Effect of Bandwidth

An estimate of the susceptibility induced in-vivo distortions were calculated as described by Wang et al., [66]. A SWIp-QSM pulse sequence, as explained in section 3.1.2.3, was used to acquire phase data in a healthy volunteer. Three echoes were used with echo times of 2.2, 4.4, and 6.6 ms to ensure the fat and water signals were in-phase. A mask was created using the magnitude data such that only pixels with values higher than 4 standard deviations of the noise were used for the creation of the B0 map. The acquired phase data was initially unwrapped using a quality guided approach similar to that used in section 3.1.2.3. The phase difference between the unwrapped first and third echo were then used to calculate the B_0 field distortion as follows:

$$\Delta B_0 = \frac{\Delta \phi}{2\pi \Delta TE} \tag{3.2}$$

Here, the unwrapped phase difference $\Delta\phi$ evolved between the first and third echoes separated by ΔTE is used to calculate the B_0 field distortion in units of Hz. This B_0 field distortion map was then used in Equation 2.36 to determine the expected susceptibility distortions in the healthy volunteer. The first and third echoes were used as the flyback setting was turned off on the MR which results in a spatial discrepancy between even and odd echoes.

Areas of large expected distortions were then investigated on the magnitude data of the healthy volunteer. The volunteer was scanned three times using a T1-weighted 3D gradient echo sequence for bandwidth values of 241.4, 481.6, and 918.5 Hz/pixel. All scans used a TR, TE, and flip angle of 6.3 ms, 3.0 ms, and 12°respectively, with the frequency encode in the AP direction. The 481.6 Hz/pixel image and the 241.4 Hz/pixel image were linearly registered to the 918.5 Hz/pixel image with the use of a commercial image registration software (MIMVista, MIM Software, Cleveland, USA), and the areas of large expected distortions were qualitatively compared to observe the effect of bandwidth on the produced distortions.

3.2.2 Bandwidth Effects on SNR

The theoretical relation between the receive bandwidth and the SNR, as stated in Equation 2.37, was validated using the ACR MRI phantom. The TR, TE, flip angle, and number of signal averages were held constant for all tests at 6.3 ms, 3.0 ms, 12°, and 1 respectively. Two sets of images were acquired for each bandwidth of 241.4, 362.1, 481.6, 604.9, 729.4, 847.9 and 918.5 Hz/pixel to permit calculation of the SNR using the difference method.

The SNR was calculated using the difference technique outlined by Dietrich et al., [15]. This technique uses two sets of images taken with identical parameters to determine the signal in a region of interest, S_{diff}, and the standard deviation of the noise, σ_{diff}, as seen in Equation 3.3.

$$SNR = \frac{S_{diff}}{\sigma_{diff}} = \frac{\frac{1}{2} * mean(S(r,k_1) + S(r,k_2))}{\frac{1}{\sqrt{2}} * stddev(S(r,k_1) - S(r,k_2))} \qquad , \qquad r \epsilon ROI \tag{3.3}$$

In Equation 3.3, $S(r, k_1)$ and $S(r, k_2)$ represent the signal within the region of interest in the first and second image respectively. A homogeneous region of interest within the ACR phantom was chosen and the SNR was calculated at each bandwidth using Equation 3.3.

The same pulse sequence parameters were used to obtain head images in a healthy volunteer in order to determine the effect of the bandwidth in-vivo. Due to time limitations, only three bandwidth values were able to be tested. The bandwidth values were chosen to be 241.4 Hz/pixel, and 918.5 Hz/pixel, and 481.6 Hz/pixel as these represented the minimum BW for acceptable distortion, highest possible and a median bandwidth respectively. A homogeneous white matter region was used as the region of interest and the SNR was calculated with the use of Equation 3.3.

3.2.3 Multi-Echo Averaging Simulations

Multi-echo averaging is one way to regain the lost SNR in high bandwidth acquisitions and as such, simulations were performed as described by Helms et al., to model the SNR advantage provided by multi-echo averaging in different brain regions [23]. The signal for a gradient echo sequence was simulated using Equation 2.30 by setting the proton density to 1. The decay of the signal amplitude, represented by the $e^{-TE/T2^*}$ in Equation 2.30, was represented by a term A such that

$$A(TE) = A_0 exp(-TE/{T_2}^*) \tag{3.4}$$

where A_0 was fixed to 1. To simulate signal decay in multi-echo averaging a cumulative average was taken of Equation 3.4 for 12 echoes spaced 4.92 ms apart. This was done for a white matter region (splenium), gray matter region (caudate) and cerebrospinal fluid region (pallidum) using ${T_2}^*$ values of 45.3 ms, 45.4 ms and 29.0 ms respectively to reproduce the Helms et al., simulations [23].

Again, as described by Helms et al., by the substitution of the trigonometric terms in Equation 2.30 by the half-angle tangents, and by using 3.4 to simulate the signal decay, the signal of the gradient echo sequence was calculated as

$$S(\alpha, TR) \approx A \frac{TR/T1}{\alpha^2/2 + TR/T1} \alpha. \tag{3.5}$$

The TR, T1, and α were fixed to 66 ms, 773 ms, and 35° to again reproduce the Helms et al, simulations. Using these signal values, the SNR values were then calculated with noise values extracted from the Helms et al., paper. All SNR values were then normalized to that of the first echo in order to observe the SNR increase with increasing number of averaged echoes.

As the Helms paper only simulated the SNR increase in healthy brain regions, a second simulation was performed to account for tumor regions. The tumor simulation involved simulating the SNR increase for gray matter, white matter, a Gadolinium enhanced glioblastoma, and a non-enhanced glioblastoma. The ${T_2}^*$ values for the gray and white matter regions were taken from literture to be 54.6 ms and 59.7 ms [40]. The ${T_2}^*$ for a glioma in a mouse was taken to be 21.9 ms at 7 T [12], and 15 ms and 9.4 T [7]. The R_2* values were taken as the reciprocal of the ${T_2}^*$ value of the gliomas at 7 and 9.4 T and linearly extrapolated in order to obtain a non-enhancing glioma ${T_2}^*$ of 93.9 ms at 3 T [40]. By using a Gd-DTPA concentration of 1.45 mmol in the tumor, the ${T_2}^*$ of the enhancing glioma was calculated to be 44.9 ms [31]. The TEs, TR, and flip angle were all maintained the same as the Helms et al., simulations for the tumor simulations.

3.2.4 Multi-Echo Averaging vs Conventional Signal Averaging

3.2.4.1 SNR Measurements

The effect of multi-echo averaging on SNR was then compared to conventional signal averaging for similar imaging times. Two sets of T1-weighted 3D GRE images were obtained for both an ACR phantom and the head of a healthy volunteer. The TR, TE, flip angle (α) and number of signal averages used were 6.3 ms, 3 ms, 12°, and 3 respectively. The two sets of images had a bandwidth of 918.5 Hz/pixel.

For the multi-echo images on the other hand, the TR and number of echoes were chosen such that the imaging time remained similar to that of the 3 signal average measurements. Accordingly, two sets of 5 echo multi-echo gradient echo images were obtained with a bandwidth of 918.5 Hz/pixel, a TE of 1.85 ms, and an echo spacing of 1.6 ms. To account for the additional echoes, the TR was increased to 19 ms. In order to maintain a similar T1 weighting the flip angle was adjusted as suggested by Helms et al., [23].

$$q = \frac{\alpha^2}{2 * TR} \tag{3.6}$$

By maintaining the same q in Equation 3.6 for both the multi echo and 3 signal average images, the same amount of T1-weighting could be maintained. As such, a flip angle of 20.7^o was used for the multi-echo average images.

Multi-echo averaging was performed with MATLAB (The Mathworks, Natick, USA). The cumulative sum of all echoes was obtained and the echoes were averaged in order to determine the increase in SNR as a function of the echo train length. For the phantom SNR measurements, a homogeneous region in the ACR phantom was manually selected for calculation to be performed. For the in-vivo images, the SNR was calculated in two white matter regions and a gray matter region manually defined as seen in Figure 3.9. White matter region 1, white matter region 2, and the gray matter region had an ROI area of 72 mm^2, 45 mm^2, and 36 mm^2 respectively. The SNR was once again calculated using the difference technique as seen in Equation 3.3.

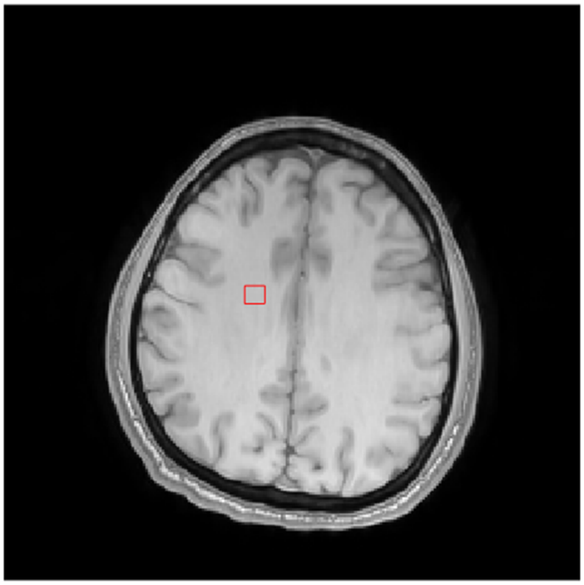

(a)

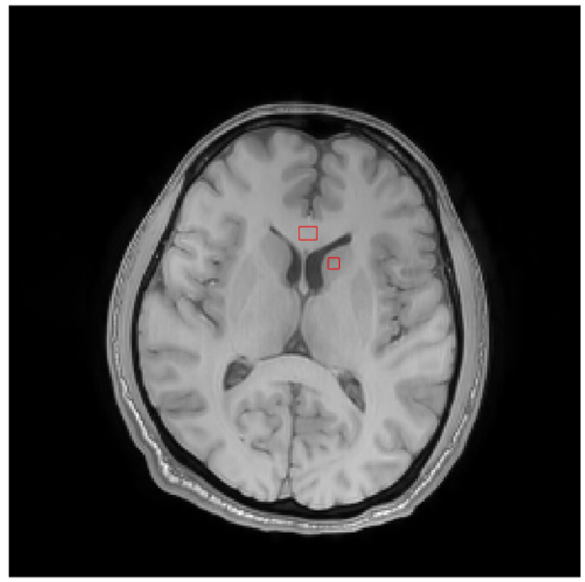

(b)

Figure 3.9: The regions of interest used for the SNR and CNR calculation. (a) A homogeneous white matter region referred to in the remainder of the thesis as white matter region one (WM1). (b) A second homogeneous white matter region and a gray matter region referred to from here on as white matter region 2 (WM2) and gray matter (GM) respectively.

3.2.4.2 Contrast to Noise Ratio Measurements

The white-grey matter contrast-to-noise ratio was then determined in the high bandwidth image, the multi-echo average image, the conventional signal average image, and the image of the first echo in the multi-echo sequence. The high bandwidth image with 1 signal average was used as the reference image to which all CNR values were normalized. The CNR was defined as Equation 3.7 inspired by the difference method SNR calculations. In Equation 3.7 the signal values and the standard deviation values were obtained as described by the difference technique [15].

$$CNR = \frac{|S_{WM2} - S_{GM}|}{\sigma_{diff}} = \frac{|(\frac{1}{2} * mean(S1_{WM2} + S2_{WM2})) - (\frac{1}{2} * mean(S1_{GM} + S2_{GM}))|}{\frac{1}{\sqrt{2}} * stddev(S1_x - S2_x)} \tag{3.7}$$

Inspired by the SNR calculation of Dietrich et al., $S1_{WM2}$ and $S2_{WM2}$ represent the signal in white matter region 2 in the first and second image respectively. Similarly, $S1_{GM}$ and $S2_{GM}$ represent the signal in the grey matter in the first and second image respectively. $S1_x$ and $S2_x$ on the other hand represent the signal value, at a specific region of interest, used to determine the standard deviation of the noise. As the difference technique was originally described to determine the SNR in one region of interest and the CNR calculation uses two different regions of interest, the region at which the standard deviation of the noise is calculated must be chosen. As such, the CNR was calculated three separate times with the standard deviation of the noise calculated in three separated regions. The CNR was calculated with the standard deviation of the noise being calculated in white matter region 1, white matter region 2, and the gray matter region as shown in Figure 3.9.

3.2.4.3 Critical Structure Depiction

Overall image quality was qualitatively assessed for the high bandwidth, first echo, conventional signal average, and multi-echo average images. The optic nerve, optic chiasm, lacrimal gland and pituitary gland were examined in order to determine the clarity of depiction in each image. These regions were chosen as they are either critical structures to be avoided during brain radiotherapy or, in the case of the lacrimal glands, areas to be avoided when treating the orbits. In either case, these regions must be clearly visualized in images for planning. In order to make equitable comparisons, all images were linearly registered to the high bandwidth image using a commercial image registration software (MIMVista, MIM Software, Cleveland, USA). As a result, positional shifts in the different images were accounted for. Of note, the comparison of the conventional signal average and multi-echo average images allowed for an image quality comparison of two methods used to regain SNR, whereas the first echo was used to observe the image quality of a short TE scan.

Chapter 4

Results and Discussion

All experimental and simulation results are presented in the following chapter. For the sake of clarity, the results have been separated into two subsection. Subsection 4.1 presents all experimental results associated with system-dependent distortion measurements, whereas subsection 4.2 presents all results associate with patient-dependent distortions and gradient echo image quality. Each measurement is accompanied with a discussion summarizing and interpreting the main result.

4.1 System-Dependent Distortion Quantification Using Grid Phantom

As mentioned in section 2.4, image distortions can be classified as system-dependent and patient-dependent. The quantification of system-dependent distortions is valuable to radiation therapy planning as they are caused by MRI hardware and common to all patients. These distortions are caused by inhomogeneities in the B_0 field along with non-linearities in the gradient field, and upon quantification an acceptable radial distance from the isocenter can be determined for imaging.

4.1.1 B0 Mapping

The B_0 field was mapped at all points in the volume of 51.2 cm by 51.2 cm by 25 cm. Field maps were extracted in 3 selected slices. Maps were obtained at the isocenter as defined by the scanner coordinate system in the DICOM image files, 7.5 cm superior to the isocenter, and 7.5 inferior to the isocenter. These slices can be seen in Figure 4.1. The isocenter was seen to be very homogeneous, with regions of inhomogeneity greater than 1 ppm only at radial distances greater than 200 mm from the isocenter. At the superior and inferior slices, the inhomogeneities are more pronounced and again seen in the top corners. As the top corners are the regions furthest from the isocenter, they are the areas most affected by B_0 inhomogeneities.

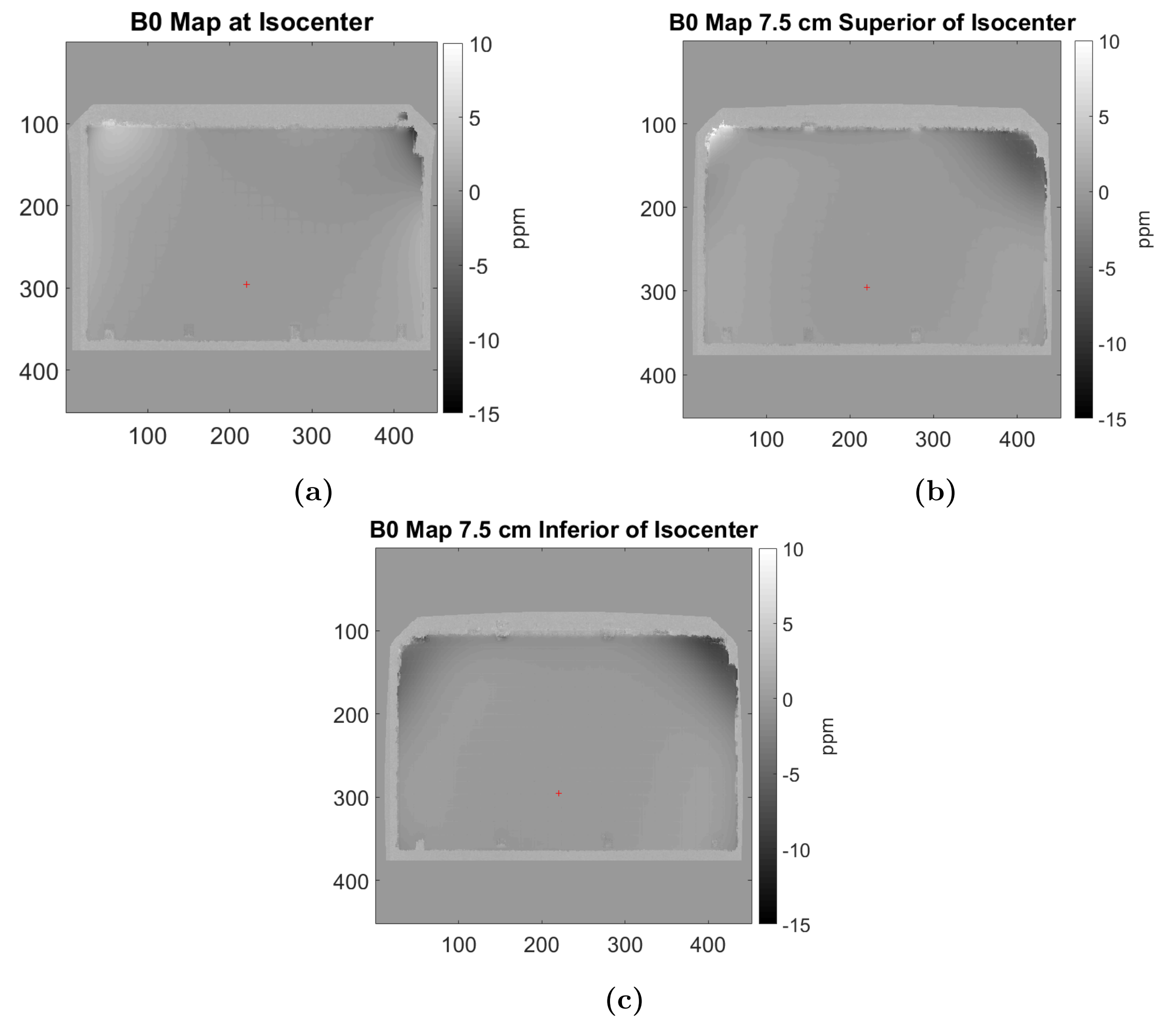

Figure 4.1: The B_0 map at (a) the isocenter, (b) 7.5 cm superior to the isocenter and (c) 7.5 cm inferior to the isocenter. Slight variation can be seen in the corners of the phantom.

The B_0 inhomogeneity was plotted as a function of radial distance from the isocenter and can be seen in 4.2a. The B_0 field did not vary significantly until an approximate radial distance of 200 mm. At distances under 200 mm from the isocenter, the average inhomogeneity remained near 0 ppm with standard deviations under 1 ppm. The change in the B_0 field was compared on scans obtained on two different days and can be seen in Figure 4.2b. The B_0 field near the isocenter again did not vary significantly from day to day and deviations of over 0.5 ppm were only seen past radial distances of 200 mm. This suggests that day-to-day drift and repositioning has a minimal effect on the B_0 field uniformity, and that the scanner shows consistent performance.

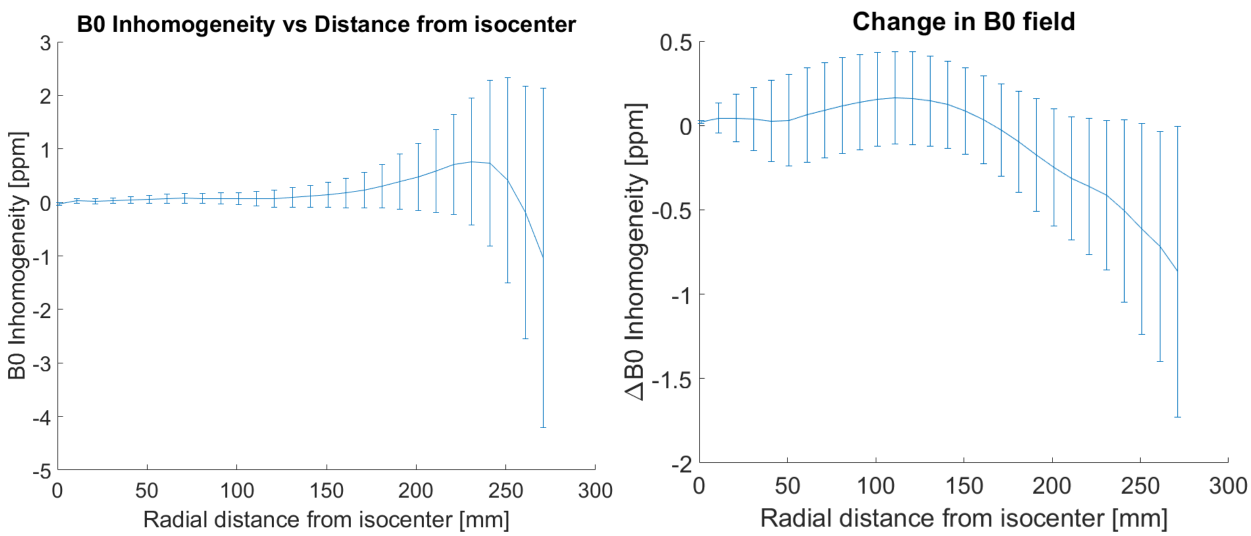

(a) **(b)**

Figure 4.2: (a) The B_0 field as a function of radial distance from the isocenter, where the error bars represent one standard deviation. (b) The difference in the B_0 field on two scans with repositioning.

4.1.2 The Effect of Vendor Corrections on Measured Distortions

MRI scanner vendors provide algorithms which correct geometric distortion at the console. The performance of these correction algorithms was tested on a T1-weighted 3D gradient echo sequence. Though distortion values were below 2 mm within 12 cm of the isocenter, they were seen to increase substantially past the 12 cm radial distance. Without the application of the vendor provided corrections the distortions were as large as 9 mm at the corners of the phantom. An axial, sagittal, and coronal slice through the isocenter along with distortion values at each pixel for the T1-w 3D GRE without vendor corrections can be seen in Figure 4.3. Though large distortion values are seen with out the application of the vendor corrections, these corrections are applied by default leading to significant decreases in the geometric distortions.

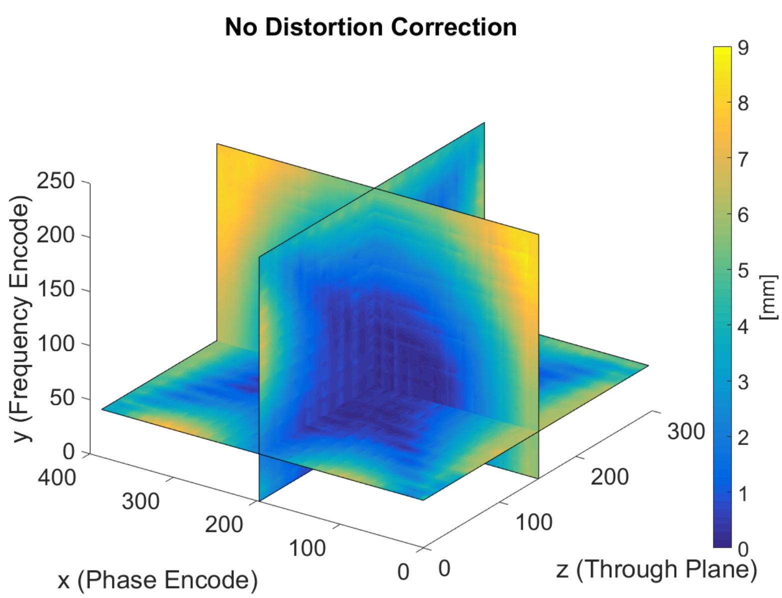

Figure 4.3: Distortion at each pixel with no vendor distortion corrections.

The MRI system featured in this work (Ingenia, Philips Healthcare) provides two algorithm options known as ”2D compensation” and ”3D compensation”. Axial, sagittal, and coronal slices of the distortion map were extracted following the application of each respective correction algorithm, and can be seen in Figure 4.4. Both correction algorithms are seen to significantly decrease the amount of distortion. The average distortion of the pixels in the upper corners were near 9 mm without distortion corrections, and were reduced to below 4 mm for the 2D and 3D compensation algorithms. Regardless of the correction algorithm applied, it was seen that the highest amount of distortion was always seen in the upper corners of the grid. This was expected as the upper corners represented the furthest distance from the isocenter.

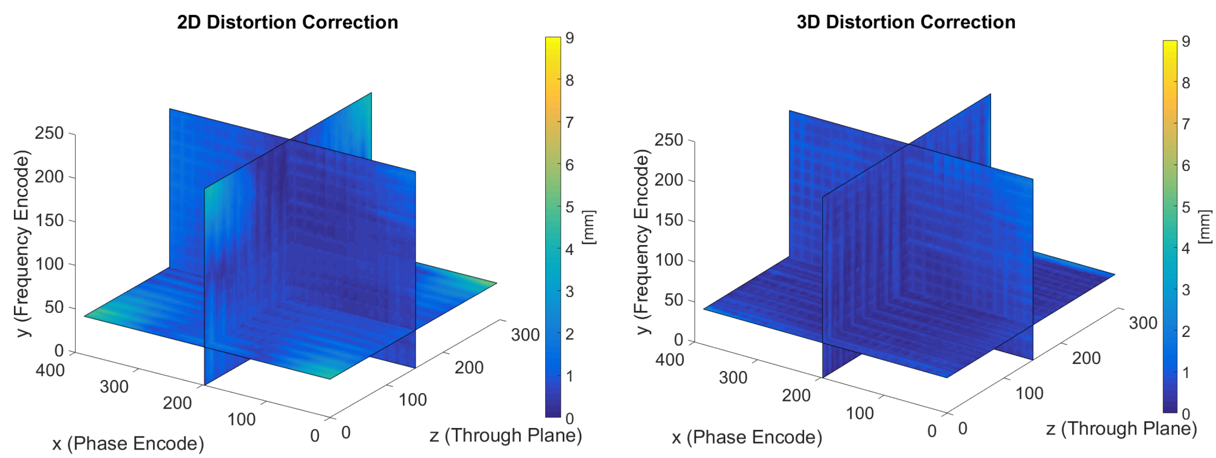

(a) (b)

Figure 4.4: An axial, sagittal, and coronal slice through the isocenter which display the distortion at each pixel following the application of (a) the 2D vendor correction and (b) the 3D vendor correction. The distortions can be seen increase toward the corners which correspond to the furthest distances from the isocenter.

The average distortions as a function of radial distance from the isocenter, with and without vendor corrections, can be seen in Figure 4.5. Again, both correction algorithms reduce distortions substantially as compared to when no algorithm is applied. The 2D correction reduces the maximum average correction seen from 9.5 mm to below 4 mm whereas the 3D correction algorithm further reduced the maximum average distortion to 2.2 mm. As the radius of an adult human head is roughly 90 mm, geometric distortions are not problematic for brain radiation therapy planning images. This observation was consistent with that of

Stanescu et al., 2008 [51].

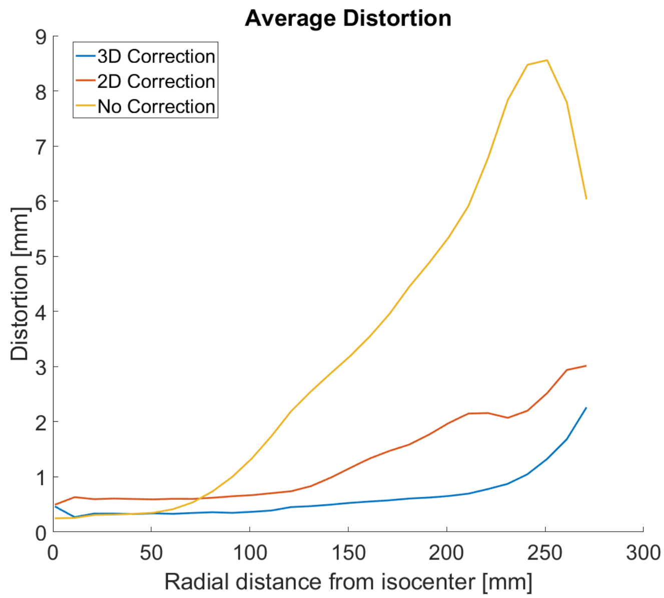

Figure 4.5: The average distortion as a function of radial distance from the isocenter for the available correction options. The 2D correction significantly reduces the amount of distortion as compared to no correction. The 3D corrections further reduce the distortion.

Distortions on each individual axis were also inspected and can be seen in Figure 4.6. It was seen that both correction algorithms were successful in correcting in-plane distortions. The difference in the correction algorithms were seen in the through plane, z, direction. The through plane distortion was seen to be similar for the 2D correction and when no correction was applied. As expected, this implies that the 2D compensation algorithm was not correcting distortions in the z direction. The through plane distortions were however corrected for by the 3D correction algorithm. This was expected as 2D corrections are normally applied to 2D sequences in which multiple slices are excited individually to obtain a 3D data set. As such, the distortions in the slice direction in 2D imaging are fundamentally different than distortions in the other two directions. 3D corrections on the other hand are applied to 3D sequences in which an entire volume is excited simultaneously, thus requiring a correction in all three directions.

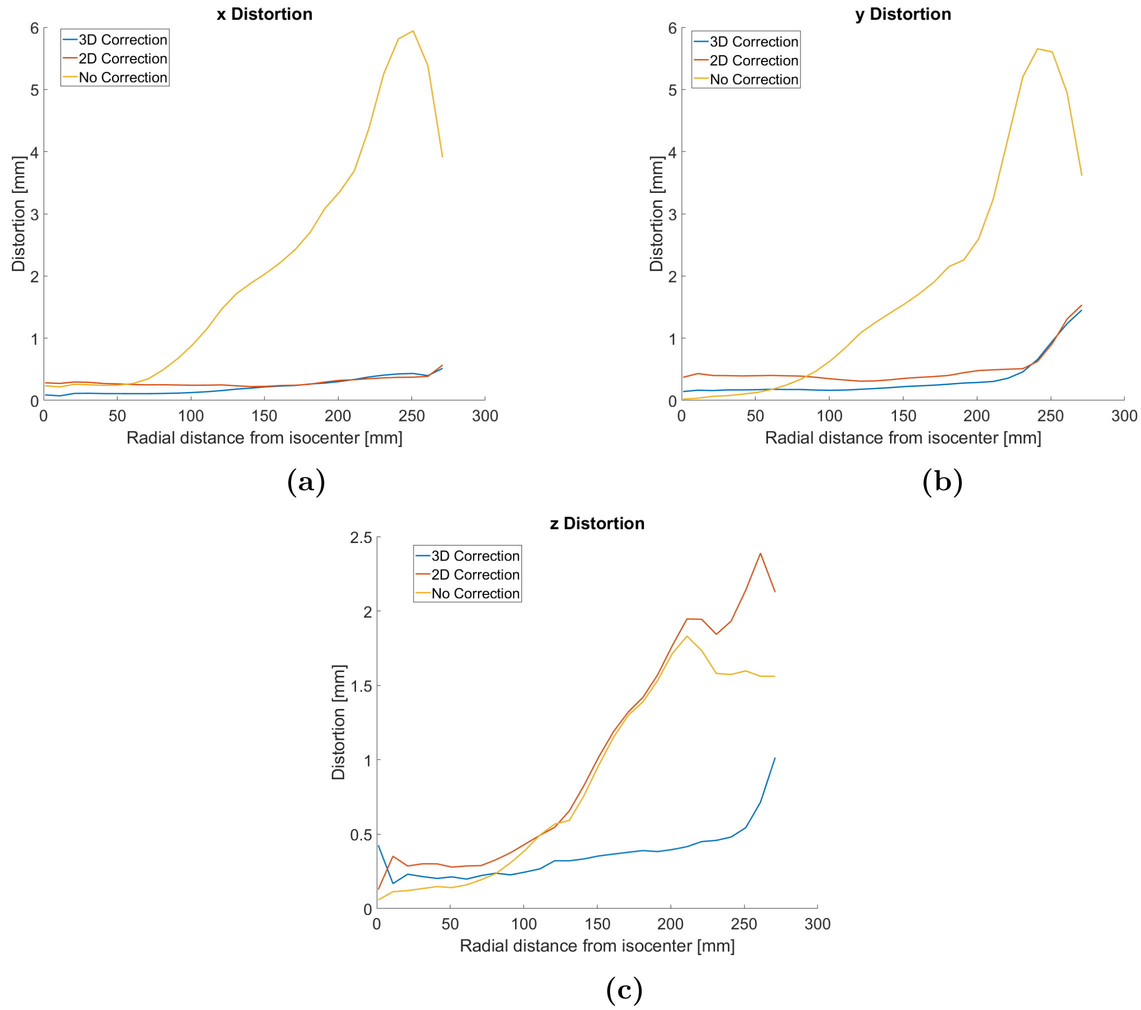

Figure 4.6: The average distortion as a function of radial distance for all correction options in the (a) x, (b) y, and (c) z directions.

In the uncorrected image, the in-plane distortions were seen to reach a maximum and begin to decrease. This is not to be interpreted as an improvement in the observed distortion but rather a limitation of the nonlinear registration. The observed distortion in the T1-w 3D GRE was such that the corners of the grid were moved up and out of the field of view used for registration. As the first grid intersection is moved out of the field of view, the second intersection immediately below is moved to closer to the original location of the first intersection. As the second intersection becomes increasingly closer to the location of the first intersection, the nonlinear registration registers the second intersection to the location of the first intersection which has been lost. The maximum is seen at around 6 mm, which corresponds to roughly half of the distance which separates the center of two grid intersection.

The plateau seen in the z distortion for the uncorrected and 2D corrected algorithms follows a similar reasoning. This plateau is seen roughly at the halfway distance of the separation of two grid sheets. Though they are placed 6.4 mm apart, there is up to 1 mm grid warping on either side of the grid, causing the separation to be closer to 4-5 mm.

4.1.3 Distortion Fields of Clinically Relevant Sequences

Multiple pulse sequences can be used to obtain images for radiation therapy planning, all with slightly different distortion fields. The distortion fields were measured for a T1-weighted 3D gradient echo, T2-weighted 2D spin echo, T2-weighted 3D spin echo and THRIVE sequence and can be seen below. The average distortion, as well as the 99.5 percentile maximum distortion were plotted as a function of radial distance from the isocenter and can be seen in Figures 4.7a, and Figure 4.7b. The 99.5 percentile maximum was measured rather than the true maximum in order to account for any outlier values. The radial distance from the isocenter at which the average distortion and the 99.5 percentile maximum distortion is below the 2 mm threshold can be seen in Table 4.1. All tested sequences were seen to have an average distortion of less than 2 mm up to a radial distance of 200 mm. The 3D gradient and spin echoes specifically were seen to have the largest radial distances with average distortion values below 2 mm. Both sequences were able to maintain an average distortion value below 2 mm for radial distances above 265 mm. The 99.5 percentile maximum distortion was less than 2 mm up to a radial of 200 mm for all but the T2-w 2D sequence. The T1-w 3D GRE and T2-w 3D spin echo specifically had radial distances up to 250 mm and 255 mm where the 99.5 percentile maximum distortion remained under 2 mm.

The acceptable radial distance for radiation therapy planning was defined by Weygand et al., as the radial distance from the isocenter at which distortion values remain below 2 mm [69]. If this radial distance was determined conservatively from the 99.5% maximum distortion, this would lead to acceptable radial distances of 154 mm, 230 mm, 255 mm, 250 for the T2-w 2D SE, T1-w THRIVE, T1-w 3D GRE and T2-w 3D SE respectively. As the average radius of a human head is roughly 100 mm, these sequences are acceptable for brain images acquired for radiotherapy planning. It has also been previously shown by Stanescu et al that geometric distortions are clinically insignificant in brain cases [51].

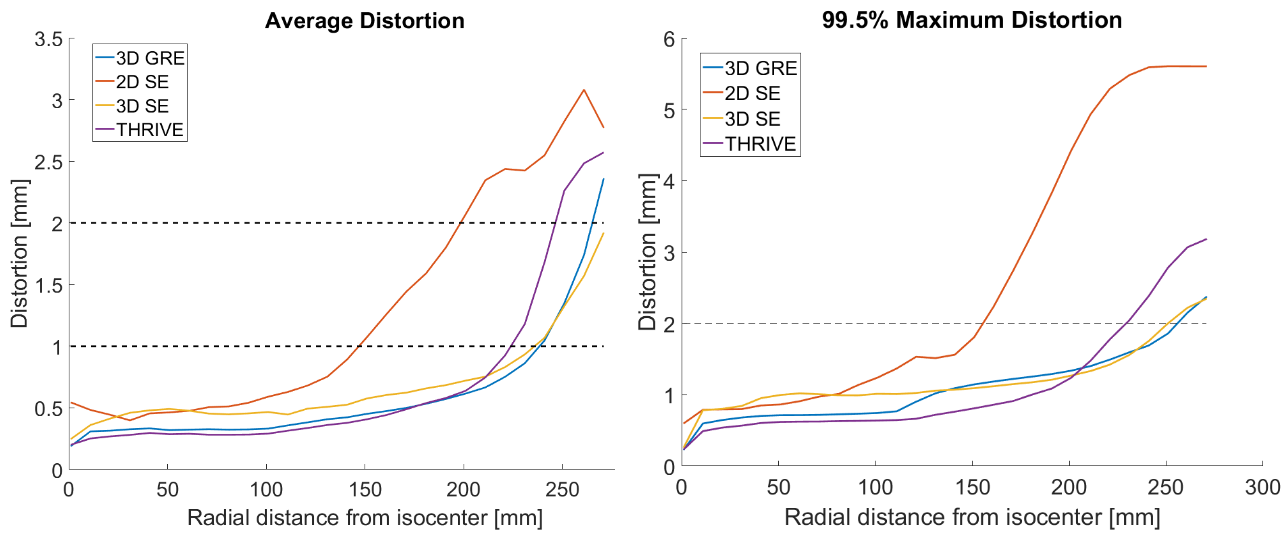

(a) (b)

Figure 4.7: (a) The average distortion as a function of radial distance for the T1-w 3D gradient echo, T2-w 2D spin echo, T2-w 3D spin echo and T1-w THRIVE sequences. (b) The 99.5 percentile maximum distortion for the four clinically relevant sequences.

Table 4.1: The radial distances from the isocenter at which an average of 1 mm and 2 mm distortions are present. Additionally, the radial distance at which the 99.5 percentile maximum distortion remains below 2 mm.

Sequence	**Radial distance with <1 mm average distortion (mm)**	**Radial distance with <2 mm average distortion (mm)**	**Radial Distance with 99.5% Maximum Distortion <2 mm (mm)**
T2-w 2D SE	146	200	154
THRIVE	223	245	230
T1-w 3D GRE	237	265	255
T2-w 3D SE	230	>270 (∼272)	250

The distortion for each sequence in each direction was also inspected and can be seen in

Figure 4.8. The average distortion for the T2-weighted 2D spin echo sequence was seen to be dominated by those in the through plane direction. As mentioned in section 4.1.2, as the 2D sequence uses the 2D correction algorithm, distortions are not corrected for in the through plane direction.

All sequences showed similar distortion values in the phase and frequency encode directions up to a radial distance of 200 mm. Beyond a radial distance of 200 mm, the distortions were dominated by those in the frequency encode direction.

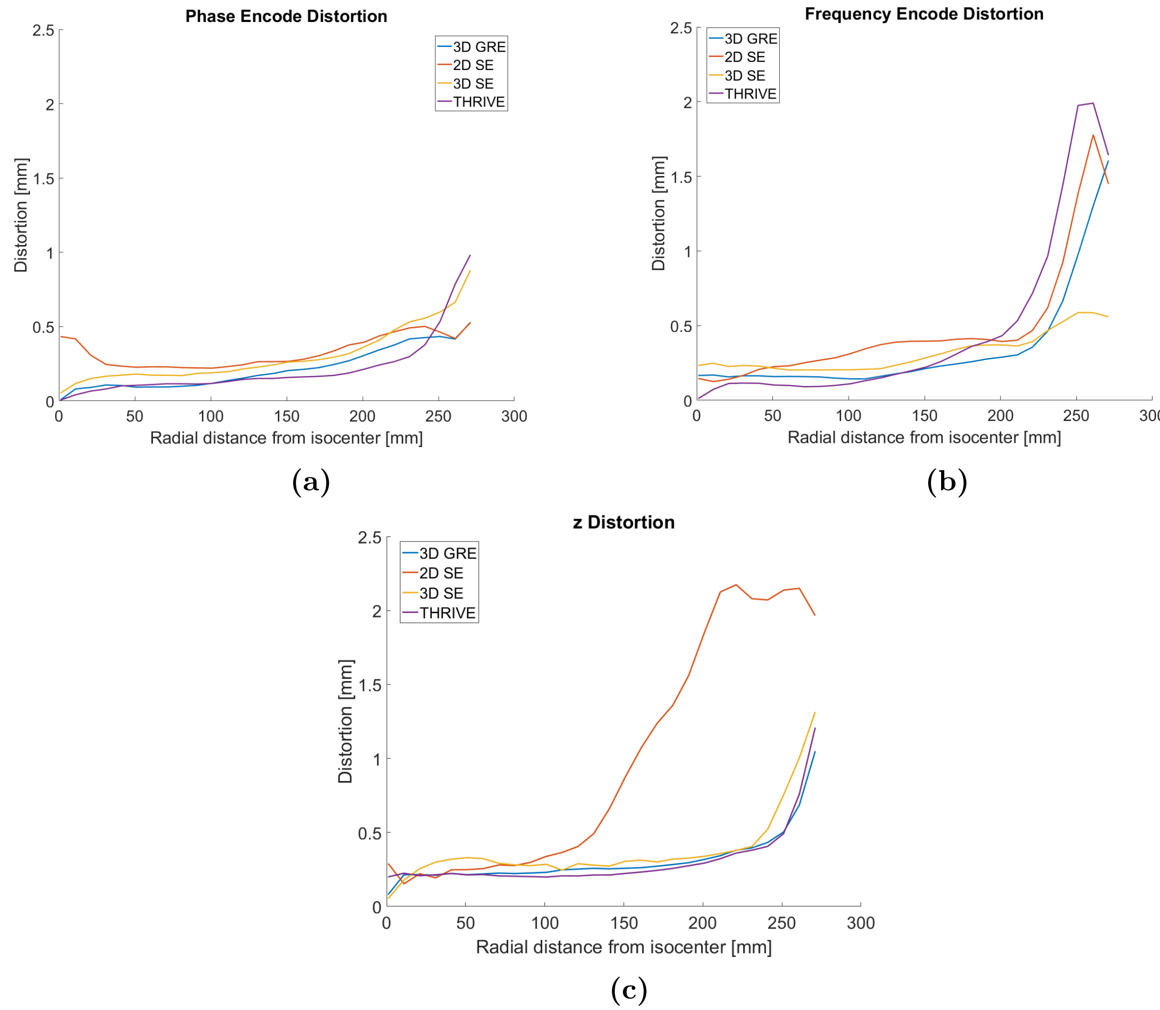

Figure 4.8: The average distortion in the (a) phase encode, (b) frequency encode, and (c) through plane directions for the four relevant sequences. The distortion in the frequency encode direction dominates past a 200 mm radial distance from the isocenter for all but the 2D spin echo sequences.

In addition to geometric distortion, varying degrees of signal loss was also present for each tested sequence. Signal loss must be taken into consideration for radiation therapy planning images as the external body contour are used for dose calculations and setup. To demonstrate this, a 3D reconstruction was performed on the acquired grid images, as seen in Figure 4.9. Signal loss was seen at the upper corners of the grid near the edge of field of view in all acquired sequences. This signal loss was a limiting factor of the field of view, as significant losses were seen in the grid when using an SI dimension of greater than 250 mm. The amount of signal loss is seen to be sequence dependent but occur at the same regions. Of note, the T2-w 3D spin echo showed the most signal loss of all tested sequences whereas the T1-w 3D gradient echo showed the least. One possible explanation for the high degree of signal loss for the T2-w 3D spin echo sequence may be due to the long echo train used. The long echo train created by the train of modulated refocusing pulses might be sensitive to B_0 inhomogeneities. As as these inhomogeneities are significant at the corners of the used imaging field of view used, it may lead to the large loss of signal.

The degree of signal loss should be taken into consideration when a pulse sequence is chosen for the acquisition of radiation therapy planning images. The choice of pulse sequence however, is only important for cases where the sensitive volume for imaging extends beyond 25 cm from the isocenter. For cases such as the head, where the imaging volume remains within a 25 cm radial distance, signal dropout is not to be expected regardless of the selected pulse sequence. The T2-weighted 3D spin echo shows signal drop out even at the slice at isocenter, at the corners, at a radial distance of 28 cm. As such, regardless of the location of the slice in the through plane direction, the T1-weighted 3D gradient echo sequence may be more suitable for anatomy near the edges of the imaging field of view.

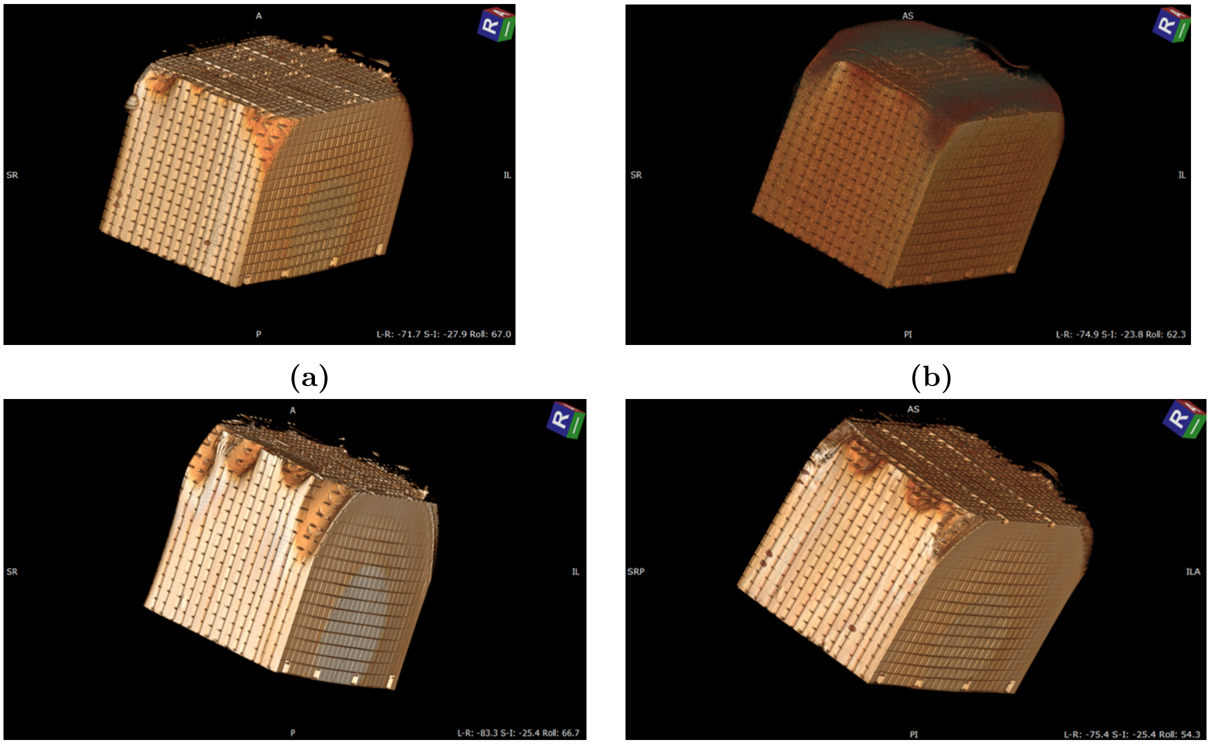

(a) **(b)**

(c) **(d)**

Figure 4.9: 3D reconstructions of the grid obtained using the (a) T1-weighted 3D gradient echo, (b) T2-weighted 2D spin echo, (c) T2-weighted 3D spin echo, and (d) T1-weighted THRIVE sequences.

4.1.3.1 T1-weighted 3D Gradient Echo

Each pulse sequence was then examined individually to determine the range and standard deviation seen at each sampled radial distance. The standard deviations and ranges for the T1-weighted 3D gradient echo can be seen below in Figure 4.10. Table 4.2 displays the average distortions, standard deviation and ranges for the T1-w 3D GRE in 50 mm increments of the radial distance.

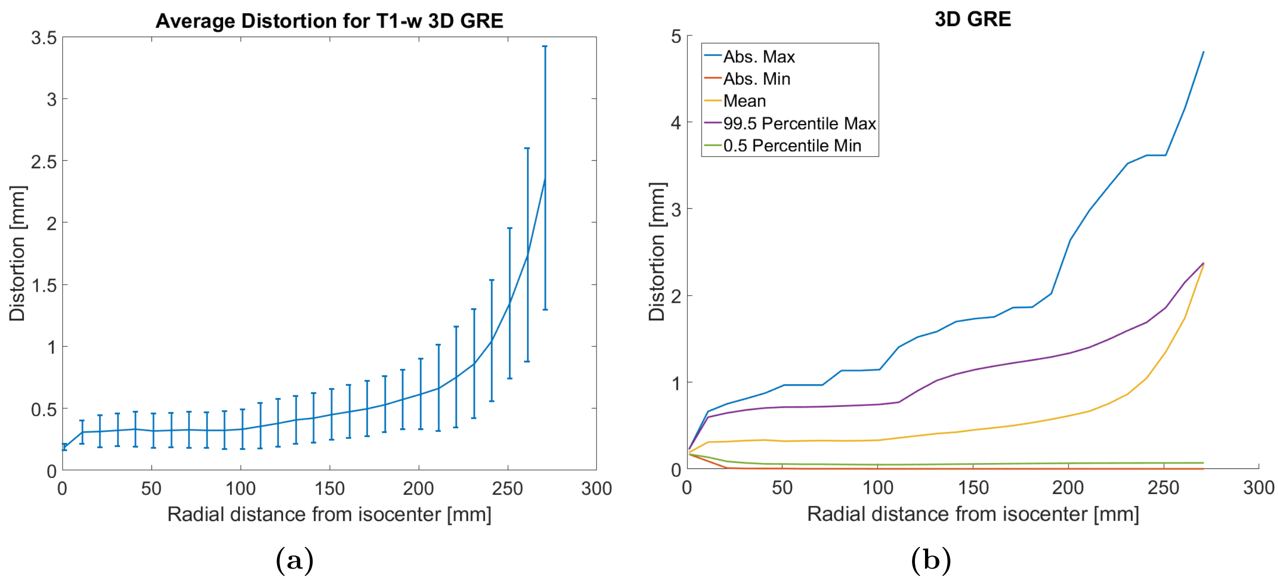

Figure 4.10: (a) The average distortion of the T1-w 3D gradient echo with the error bars representing the standard deviation at each sampled point. (b) The range of distortion values for the T1-w 3D gradient echo sequence.

Table 4.2: The average distortion, standard deviation and ranges observed in the T1-weighted 3D gradient echo sequence in 50 mm radial distance increments.

Radial distance from isocenter [mm]	**Average Distortion [mm]**	**SD [mm]**	**Abs. Min-Abs. Max [mm]**	**0.5% Min-99.5% Max [mm]**
1	0.2	0.0	0.2-0.2	0.2-0.2
50	0.3	0.1	0.01- 1.0	0.06-0.7
100	0.3	0.2	0.00-1.1	0.05-0.7
150	0.5	0.2	0.00-1.7	0.05-1.1
200	0.6	0.3	0.00-2.6	0.06-1.3
250	1.4	0.6	0.00-3.6	0.07-1.9
270	2.4	1.1	0.00-4.8	0.07-2.4

The average distortions in the T1-w 3D GRE were below 2 mm for radial distances below 265 mm from the isocenter. At a radial distance of 250 mm, the 99.5% maximum distortion remains under 2 mm, at 1.86 mm. The standard deviation is also seen to increase as the distortion value increases. The standard deviation remains roughly half that of the average distortion value.

4.1.3.2 T2-weighted 2D Spin Echo

The average distortion for the T2-weighted 2D spin echo, along with the range and standard deviations can be seen in Figure 4.11. Table 4.3 then displays these values in 50 mm increments from the isocenter. Though an average distortion value of 2 mm is seen at a 200 mm radial distance, the large standard deviation of 1.04 mm leads to significant maximum distortion values. The 99.5% maximum distortion at a 200 mm radial distance is 4.42 mm. These large distortion values are due to the significant through plane distortions that go uncorrected in the 2D spin echo sequence. The 99.5% max is seen to increase significantly following 150 mm due to the significant increase in the through plane distortion as seen in Figure 4.8.

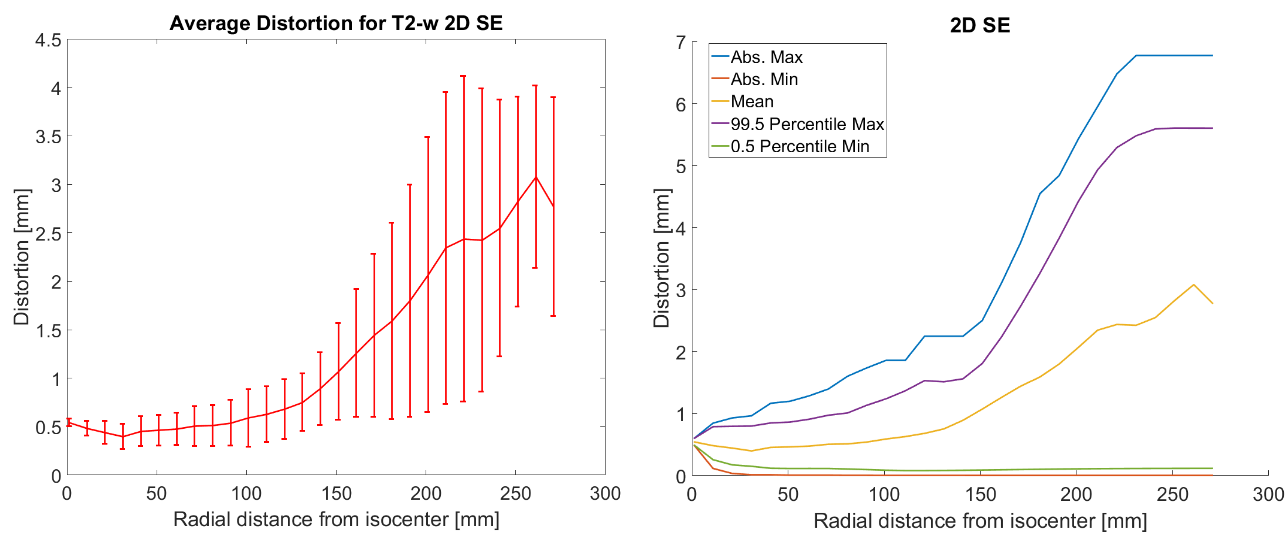

(a) (b)

Figure 4.11: (a) The average distortion of the T2-w 2D spin echo with the error bars representing the standard deviation at each sampled point. (b)The range of distortion values for the T2-w 2D spin echo sequence.

Table 4.3: The average distortion, standard deviation and ranges observed in the T2-weighted 2D spin echo sequence in 50 mm radial distance increments.

Radial distance from isocenter [mm]	**Average Distortion [mm]**	**SD [mm]**	**Abs. Min-Abs. Max [mm]**	**0.5% Min-99.5% Max [mm]**
1	0.5	0.0	0.5-0.6	0.5-0.6
50	0.5	0.2	0.01-1.2	0.1-0.9
100	0.6	0.3	0.00-1.9	0.09-1.2
150	1.1	0.5	0.00-2.5	0.09-1.8
200	2.1	1.4	0.00-5.4	0.1-4.4
250	2.8	1.1	0.00-6.8	0.1-5.6
270	2.8	1.2	0.00-6.8	0.1-5.6

4.1.3.3 T2-weighted 3D Spin Echo

The average distortion, along with the standard deviation and range values for the T2-weighted 3D spin echo can be seen in Figure 4.12 and Table 4.4. The radial distance at which an average distortion of 2 mm is seen goes slightly beyond 270 mm, to an extrapolated value of 272 mm. The 99.5% max was seen to be 2 mm for a radial distance of 250 mm.

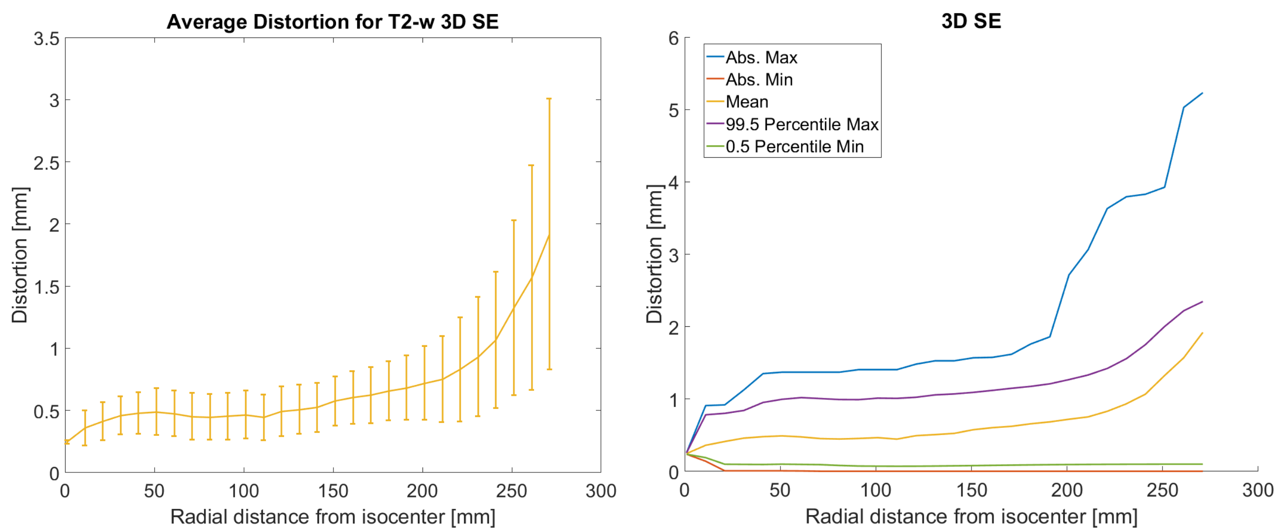

(a) **(b)**

Figure 4.12: (a) The average distortion of the T2-w 3D spin echo with the error bars representing the standard deviation at each sampled point. (b) The range of distortion values for the T2-w 3D spin echo sequence.

Table 4.4: The average distortion, standard deviation and ranges observed in the T2-weighted 3D spin echo sequence in 50 mm radial distance increments.

Radial distance from isocenter [mm]	Average Distortion [mm]	SD [mm]	Abs. Min-Abs. Max [mm]	0.5% Min-99.5% Max [mm]
1	0.3	0.0	0.2-0.3	0.2-0.23
50	0.5	0.2	0.01-1.4	0.1-1.0
100	0.5	0.2	0.00-1.4	0.07-1.0
150	0.6	0.2	0.00-1.6	0.08-1.1
200	0.7	0.3	0.00-2.7	0.1-1.3
250	1.3	0.7	0.00-3.9	0.1-2.0
270	1.9	1.1	0.00-5.2	0.1-2.4

As the debate between using the old and more conventional 2D spin echo sequence, or the newer and potentially improved 3D spin echo sequence remains unsettled, each sequence was seen to have unique advantages. The application of the 3D correction algorithm was seen to reduce the geometric distortion seen in the 3D SE sequence to well below those of the 2D SE sequence. Though the distortions were seen to be reduced, as mentioned in section 4.1.3, the 3D SE sequence suffers for a high degree of signal loss at large radial distances from the isocenter. As such both aspects should be taken into consideration when choosing between the 2D or 3D spin echo sequences.

4.1.3.4 T1-weighted THRIVE

The average distortion, along with the standard deviation and range values for the T1-weighted THRIVE sequence can then be seen in Figure 4.13 and Table 4.5. The radial distance at which an average distortion of 2 mm was seen was slightly lower than those of the 3D spin echo and 3D gradient echo sequences. An average distortion of 2 mm was seen at a radial distance of 245 mm. The 99.5% maximum distortion of 2 mm was seen at approximately 230 mm.

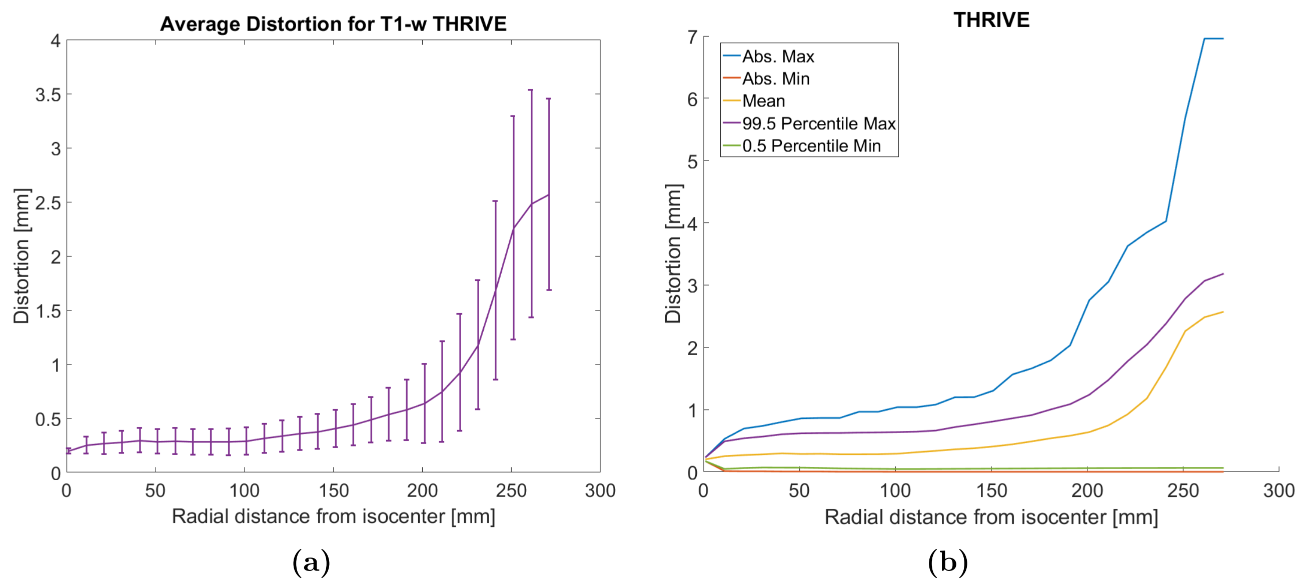

Figure 4.13: (a) The average distortion of the T1-w THRIVE with the error bars representing the standard deviation at each sampled point. (b) The range of distortion values for the T1-w THRIVE sequence.

Table 4.5: The average distortion, standard deviation and ranges observed in the T1-weighted THRIVE sequence in 50 mm radial distance increments.

Radial distance from isocenter [mm]	**Average Distortion [mm]**	**SD [mm]**	**Abs. Min-Abs. Max [mm]**	**0.5% Min-99.5% Max [mm]**
1	0.2	0.0	0.2-0.2	0.2-0.2
50	0.3	0.1	0.01-0.9	0.07-0.6
100	0.3	0.1	0.00-1.0	0.05-0.6
150	0.4	0.2	0.00-1.3	0.05-0.8
200	0.6	0.4	0.00-2.8	0.06-1.2
250	2.3	1.0	0.00-5.7	0.06-2.8
270	2.6	0.9	0.00-7.0	0.06-3.1

For all curves, though the error bars represent the standard deviation of the distortion, it was noted that this was not a representation of the image noise alone. As the distortions are averaged across all angles for different radial distances, the contribution of the distortion caused by the three different gradient fields vary for every angle. As such, large variations can be seen in the distortions across all orientations at a given distance.

4.1.4 Reproducibility of the Distortion Measurements for the T1-weighted 3D GRE Sequence

The reproducibility of the distortion measurements were tested for the T1-weighted 3D gradient echo sequence and can be seen in Figure 4.14. The average total distortions were seen to be very reproducible regardless of the day the images were required. The majority of the deviations seen were for radial distances of less than 250 mm and even in these regions the maximum variation is only 0.10 mm. This reproducibility was also determined in each axis and can be seen below in Figure 4.15.

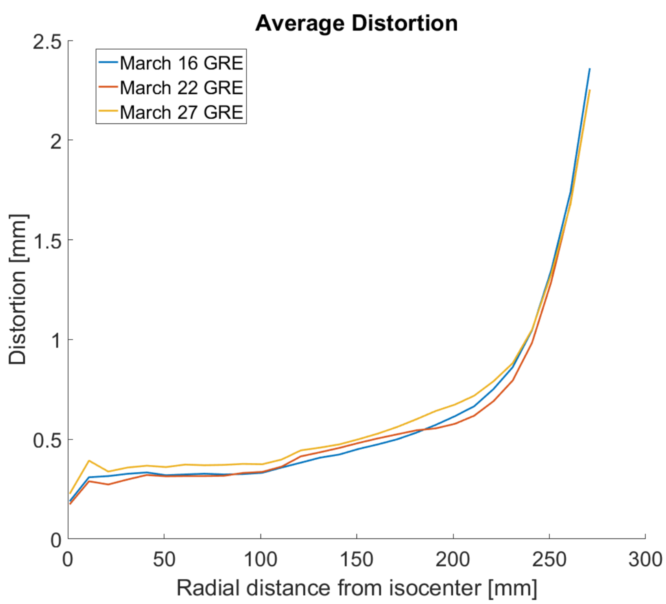

Figure 4.14: The reproducibility of the distortions seen in the T1-w 3D GRE. The maximum variation seen from scan to scan is roughly 0.1 mm.

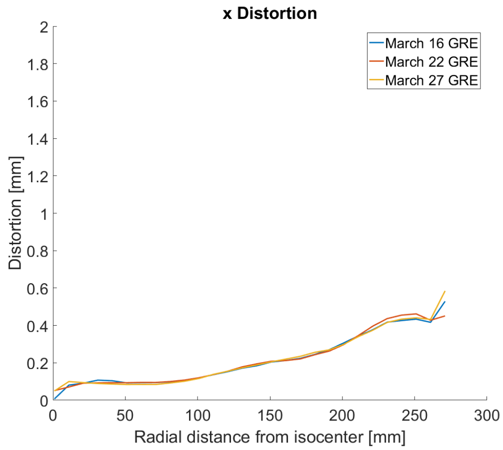

(a)

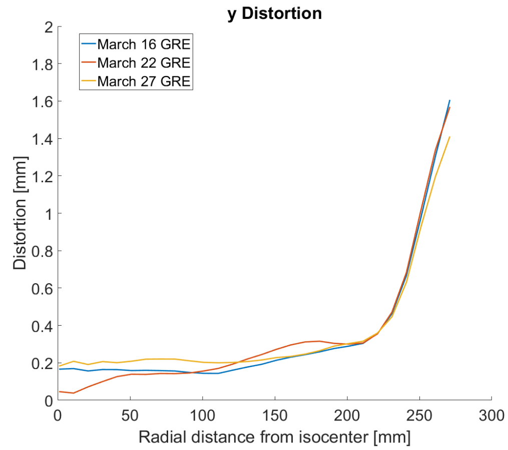

(b)

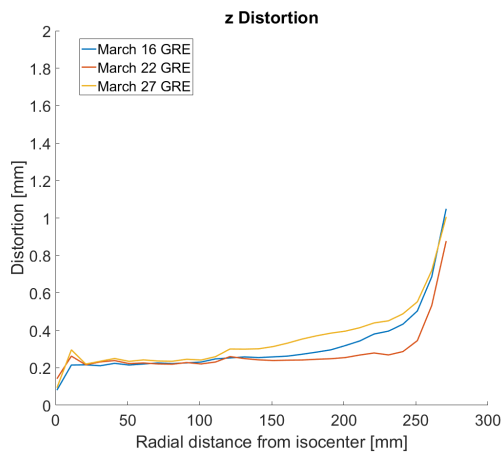

(c)

Figure 4.15: The reproducibility of the T1-w 3D GRE in all the (a) x, (b) y, and (c) z directions. The distortions were seen to be reproducible in every direction.

Upon determining the distortion in each individual direction for the three T1-weighted 3D gradient echo images it was seen that the distortions were reproducible in every direction. A maximum variation of 0.21 mm was seen in the z direction, which was less than the slice thickness of the image, and low enough to have minimal clinical significance.

4.1.5 Effect of MRI Slice Thickness Interpolation on Distortion Field Measurement

The distortion measurements using varying slice thicknesses of MR can be seen in Figure 4.16. The effect of using larger slice thicknesses was seen to have a minimal effect on the observed distortion below 270 mm radial distances. The maximum variation seen between the four slice thickness was 0.14 mm. This was similar to the reproducibility tests, as seen in section 4.1.4, which showed a maximum variation of 0.10 mm. All deviations were seen to be subvoxel in magnitude and clinically insignificant.

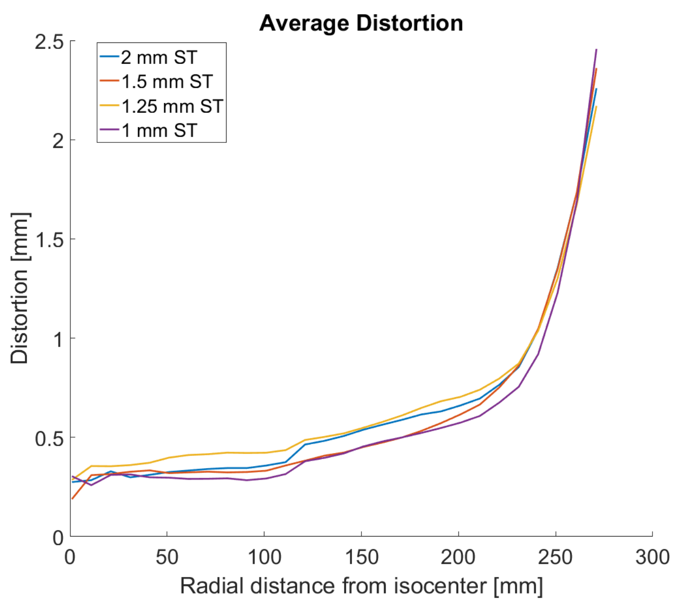

Figure 4.16: The effect of using different slice thicknesses on the MR to find the distortion field. The effect of the slice thickness was seen to be minimal with variations similar to those seen in the test of the reproducibility.

The distortion was also split into its x, y and z components and can be seen below in Figure 4.17. Again, the distortions were seen to be reproducible in all directions. The biggest difference was expected to be seen in the z direction as this corresponded to the slice thickness used. The maximum deviation seen in the z direction however was 0.26 mm, similar to the 0.21 mm deviation seen in the z direction for the reproducibility tests. The y distortion showed a maximum variation of 0.52 mm at radial distance of 270 mm, but again the signal drop out may have influenced these values near the edges of the field.

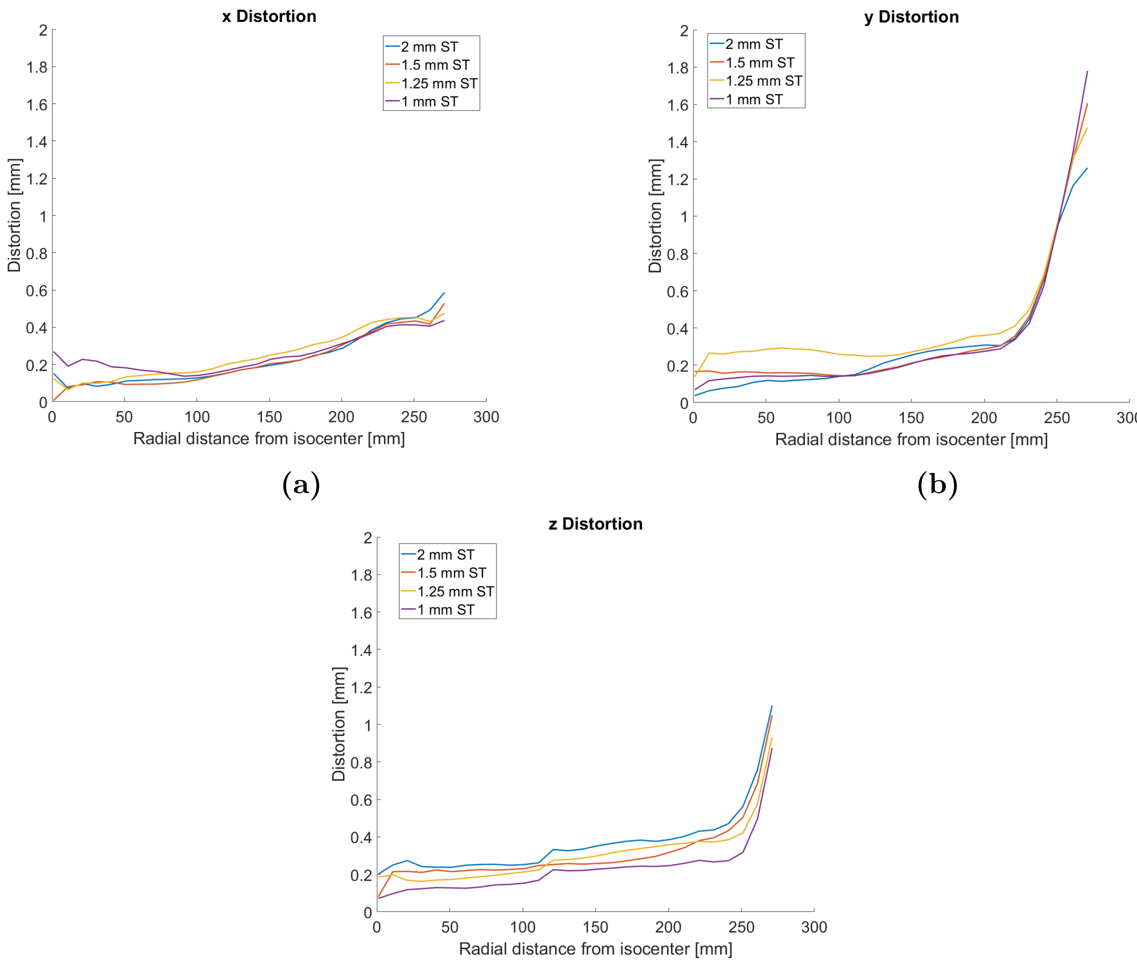

(a) (b)

(c)

Figure 4.17: The effect of the MR slice thickness on the obtained distortion in the (a) x, (b) y, and (c) through plane directions. The effect was seen to be minimal in the three directions.

Since an increase in the slice thickness showed a minimal effect on the measured distortion, slices larger than the CT thickness can be used when acquiring the images for distortion field measurements. By using larger slice thicknesses, the scan time can be significantly reduced.

4.1.6 Distortions Fields for Varying Bandwidths

The bandwidth was then varied and the average distortions were observed as shown in Figure 4.18. The radial distance at which an average 2 mm distortion was measured can be seen Table 4.6. As expected, the radial distance at which an average of 2 mm distortion was measured was seen to increase with increasing bandwidth. From the minimum bandwidth of 244 Hz/pixel to the maximum bandwidth of 926 Hz/pixel an increase of roughly 30 mm of acceptable radial distance is acquired. It was also noted that the reduction in distortion was mainly seen past a radial distance of 200 mm. Below a 200 mm radial distance, the different levels of bandwidth showed similar amounts of distortion.

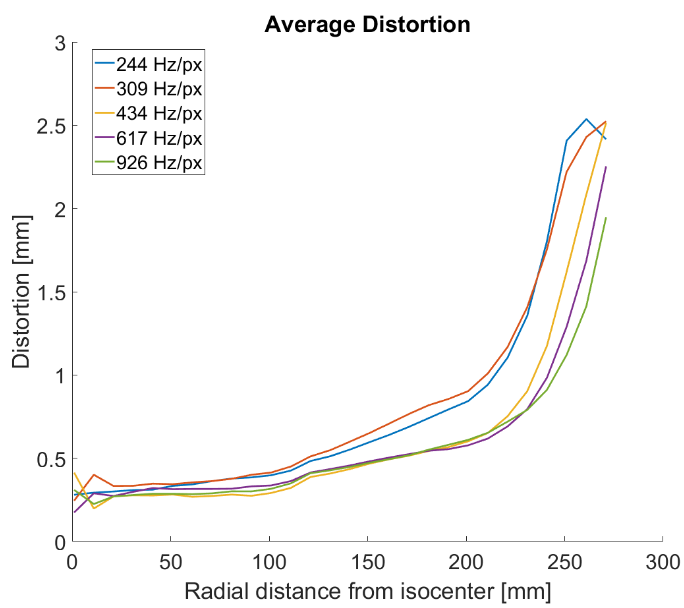

Figure 4.18: The total distortion as a function of radial distance for varying bandwidth values. The bandwidth values of each sequence can be seen in Table 4.6. Increasing the bandwidth is seen to decrease the distortion as expected.

Table 4.6: The radial distance at which average distortions are below 1 mm and 2 mm for T1-w 3D GRE images as a function of radial distance with varying bandwidth levels.

Bandwidth/pixel	**Radial distance with <1 mm distortion (mm)**	**Radial distance with <2 mm distortion (mm)**
244 Hz/px	213	243
309 Hz/px	210	245
434 Hz/px	238	258
617 Hz/px	240	265
926 Hz/px	244	>270 (~271)

The effect of the bandwidth on the distortion in each individual direction can be seen below in Figure 4.19. In Figure 4.19 it can be seen that by increasing the bandwidth, the distortion was only reduced in the frequency encode direction. The distortion in the phase encode and through plane directions were constant, regardless of the bandwidth value. Additionally, the reduction of distortion seen in the frequency encode direction was significant only after the 200 mm radial distance mark. Below a radial distance of 200 mm, the distortions in all directions were similar.

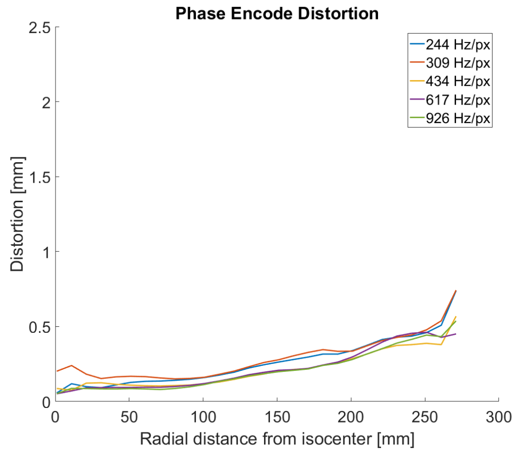

(a)

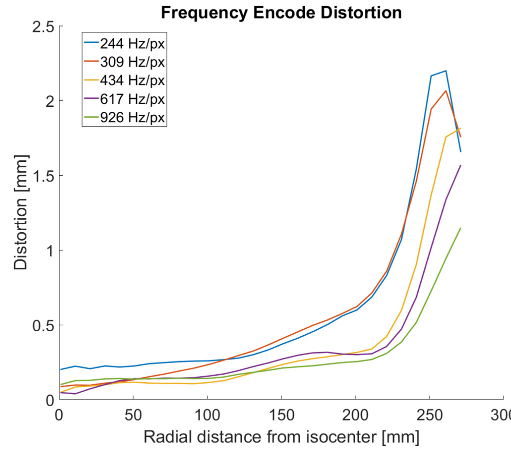

(b)

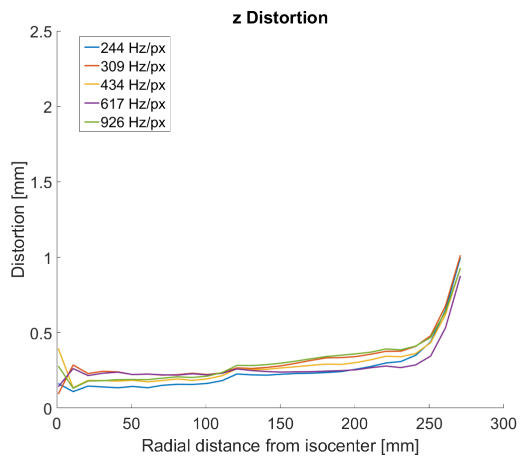

(c)

Figure 4.19: The distortion as a function of radial distance in (a) the phase encode, (b) the frequency encode, and (c) the through plane directions. The bandwidth is seen to reduce the distortion in the frequency direction.

4.1.7 Sequence Independent Distortions

The sequence independent distortion was found using the T1-w 3D gradient echo sequence and can be seen in Figure 4.20. It can be seen that the average distortion was of similar value regardless of the fat shift direction, where the fat shift direction corresponds to a polarity of the frequency encode gradient. Once the sequence independent distortions where isolated, it was seen that the sequence dependent distortions were always below 2 mm for the tested 270 mm radial distance from the isocenter. This is similar to the sequence independent distortion seen by Baldwin et al., who saw distortion values within -2 mm to 2 mm in a 400x250x120 mm^3 FOV in a 3T scanner [5].

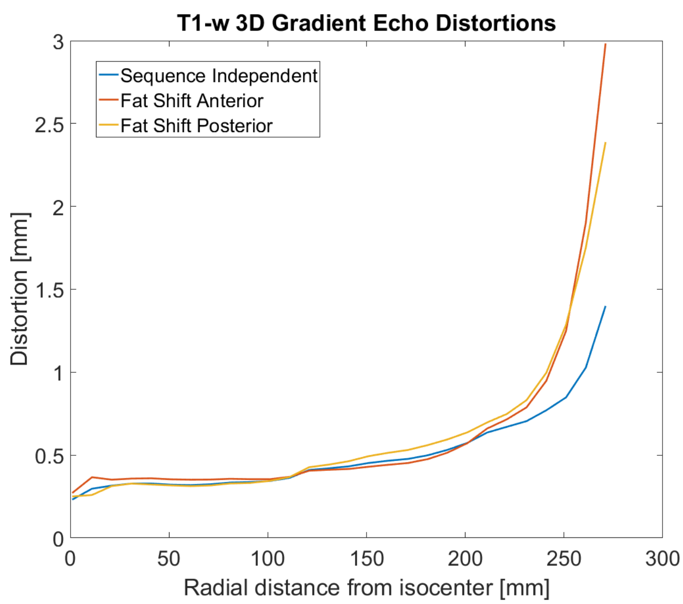

Figure 4.20: The total distortion as a function of radial distance from the isocenter for the T1-w 3D gradient sequence with the fat shift in the anterior and posterior direction. These distortions are then averaged to obtain the sequence independent distortion.

The sequence independent distortion was looked at in the phase encode, frequency encode, and through plane distortions and can be seen in Figure 4.21. As only the polarity of the frequency encode gradient was reversed, the direction of the distortions were seen to be flipped in only the frequency encode direction. The sequence independent distortions were seen to be dominant in the through plane distortions.

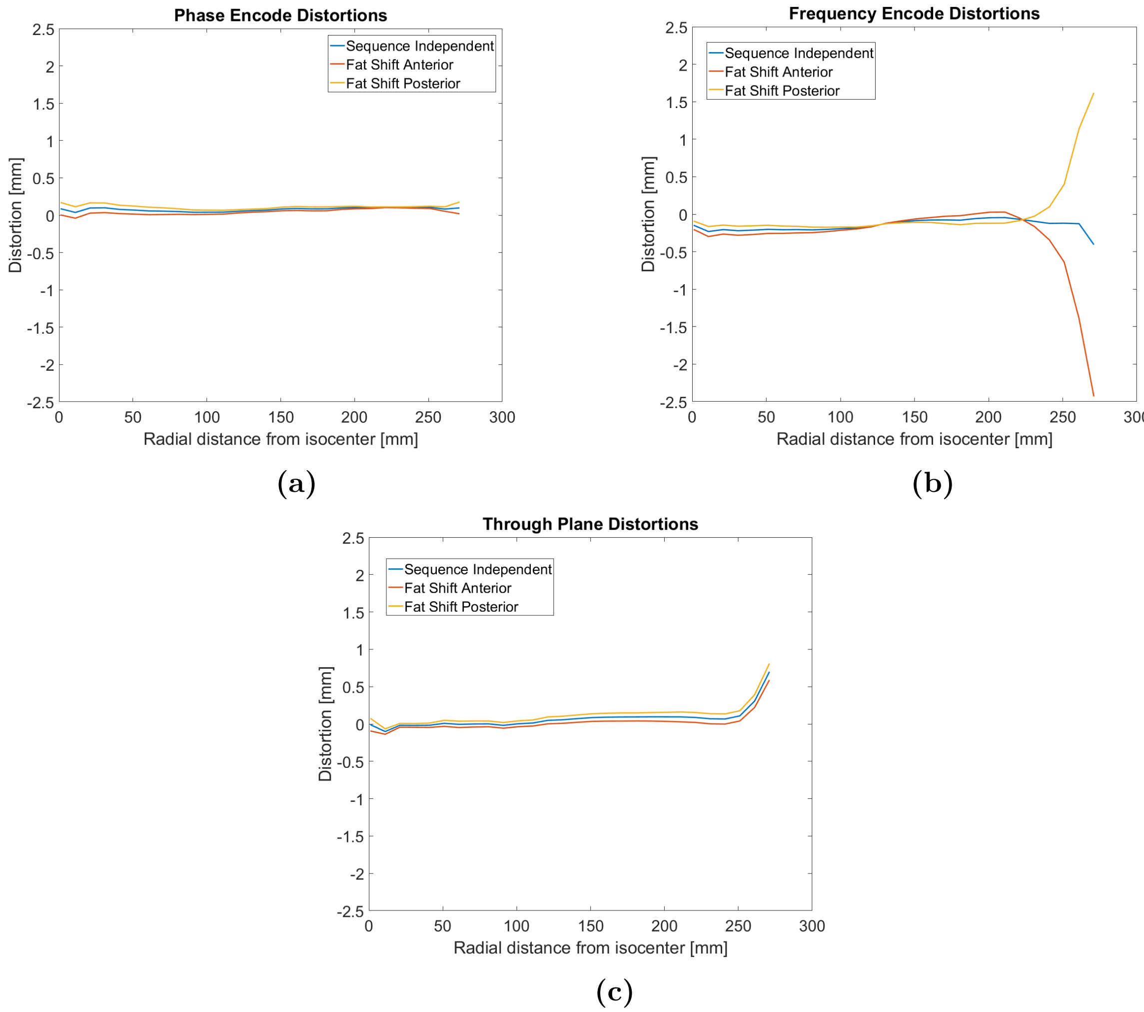

Figure 4.21: The sequence independent distortion as a function of radial distance in (a) the phase encode, (b) the frequency encode, and (c) the through plane directions.

4.1.8 Summary of the System-Dependent Distortion Experiments

System-dependent distortions were measured for a large field of view using an in-house pelvis sized phantom. The B_0 homogeneity was measured and was found to vary by over 1 ppm only at radial distances greater than 200 mm from the isocenter. The performance of the ”2D compensation” and ”3D compensation” vendor provided correction algorithms were also tested on the T1-weighted 3D gradient echo sequence. The ”2D compensation” algorithm corrected in-plane distortions, whereas the ”3D compensation” algorithm corrected both in-plane and through plane distortions. Due to the significant distortion reduction achieved by the correction algorithms, it is suggested they be used for all scans obtained for radiation therapy planning.

Distortion fields were also quantified for the T1-weighted 3D gradient echo, T2-weighted 2D spin echo, T2-weighted 3D spin echo, and T1-weighted THRIVE sequences. The radial distance from the isocenter at which their average distortions were below 2 mm were found to be 265 mm, 200 mm, 272 mm, and 245 respectively. The radial distance from the isocenter at which the 99.5 percentile maximum distortion was below 2 mm was found to be 255 mm, 154 mm, 250 mm, and 230 mm respectively. The distortion for the 3D sequences were all dominated by frequency encode direction distortions, whereas the distortion in the 2D sequence was mainly in the through plane direction. The frequency encode distortions were reduced with increased readout bandwidth.

The reproducibility of the distortion field was also tested for the T1-weighted 3D sequence and the maximum variation was seen to be within 0.1 mm for all tests. The effect of the MRI slice thickness used for distortion field quantifications was also observed and seen to be minimal. This suggested MRI slice thicknesses as large as 2 mm could be acceptable for distortion field quantification. Finally, the sequence independent distortion were measured and seen to be below 1.5 mm for the entire 270 mm radial distance tested.

4.2 Patient-Dependent Distortions and Multi-Echo Gradient Echo Image Quality Assessment

In addition to system-dependent distortion, patient-dependent distortions also reduce the spatial precision of MR images. Patient-dependent distortions are in-vivo distortions caused by large differences in susceptibility. As such, these distortions are prevalent around air-tissue or air-bone interfaces. The standard way to reduce these distortions is through an increase in the bandwidth, which comes at a cost of SNR. However, methods may be applied following the acquisition of high bandwidth images to regain the lost SNR. The conventional method used to regain SNR is through signal averaging. Conventional signal averaging involves repeated acquisition of images which are then averaged to increase SNR. As opposed to conventional signal averaging, multi-echo averaging is another method by which SNR may be regain. In multi-echo averaging multiple images are acquired at varying echo times per each excitation. These images may also be averaged to obtain an increase in SNR. The following section presents a study of patient-dependent distortions, and a comparison of conventional signal averaging to multi-echo averaging in terms of image quality.

4.2.1 Patient-Dependent Distortions

4.2.1.1 Regions of High Expected Distortions

Though susceptibility distortions vary from patient to patient, the areas at which they occur remain constant. The expected susceptibility induced distortions in a head were calculated using phase data collected from a healthy volunteer, and can be seen in Figure 4.22. The maximum expected distortions were seen at air-tissue and air-bone interfaces as predicted, and explained in Section 2.4.2. Susceptibility induced distortions are most prevalent in regions of large susceptibility differences, such as those between air and tissue or air and bone. As such, the susceptibility induced distortions are most relevant near areas such as the sinuses, and the ear canal. Though the distortion in these areas may not be of concern for diagnostic images, they are important to consider in radiation therapy planning. More homogeneous areas such as the gray and white matter in the brain do not have large susceptibility differences and therefore do not experience a large amount of susceptibility induced distortions. This suggests that susceptibility distortions are not of concern when imaging brain tumors far from air-tissue or air-bone interfaces.

Though the maximum expected susceptibility induced distortions were seen around the sinus and the ear canal, the magnitude of these distortions was still below 2 mm. The use of a high bandwidth acts to reduce these distortion values near areas of concern.

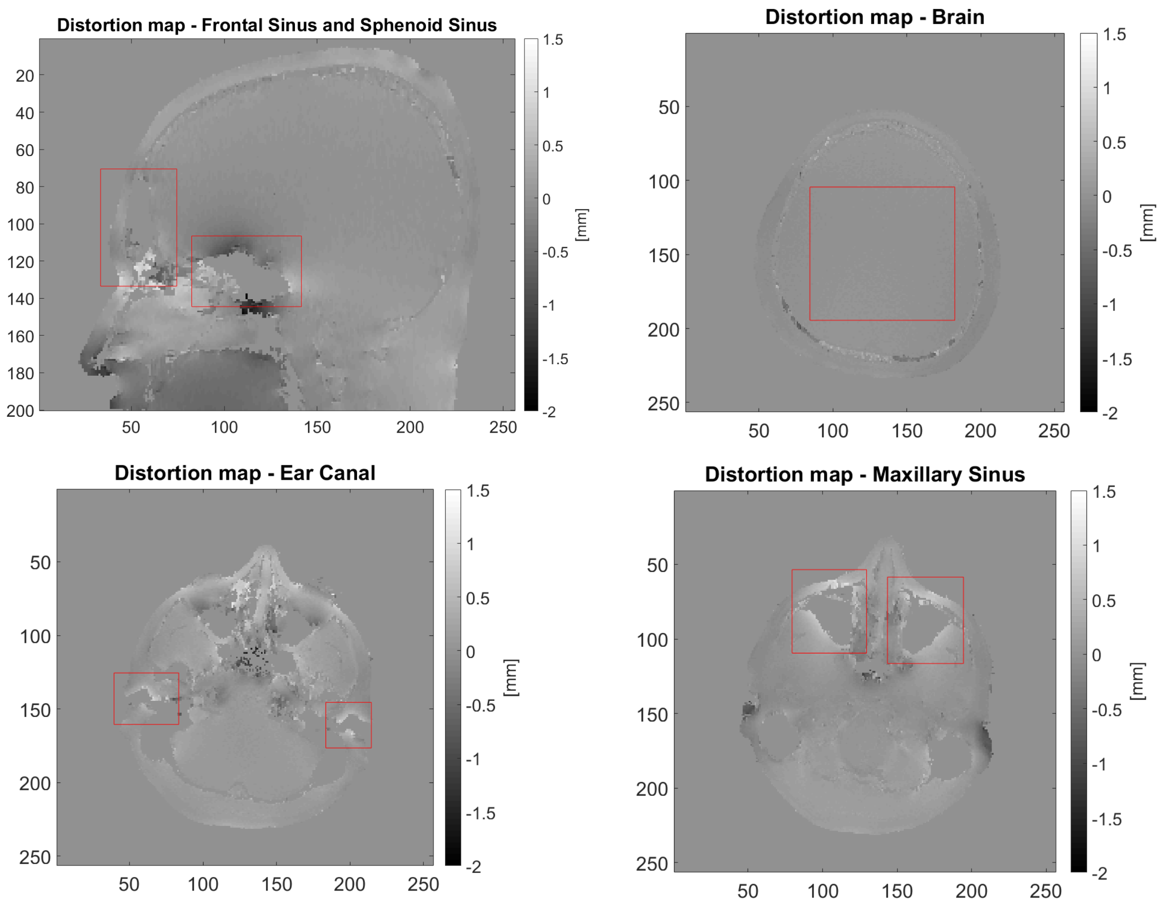

Figure 4.22: The expected distortions in the frontal sinus, sphenoid sinus, maxillary sinus, ear canal and the brain. The sinuses as well as the ear canal present regions of large expected distortions due to the large difference in susceptibility in the tissue-air interface. The brain shows low expected distortions as the susceptibility is more homogeneous.

4.2.1.2 Reduction of Distortions at High Bandwidth

As a CT of a healthy volunteer was not able to be obtained, a lack of a gold standard image rendered a reliable quantitative measurement of the distortions to be difficult. Instead, a qualitative improvement in the image quality with increasing bandwidth can be seen figures 4.23, and 4.24.

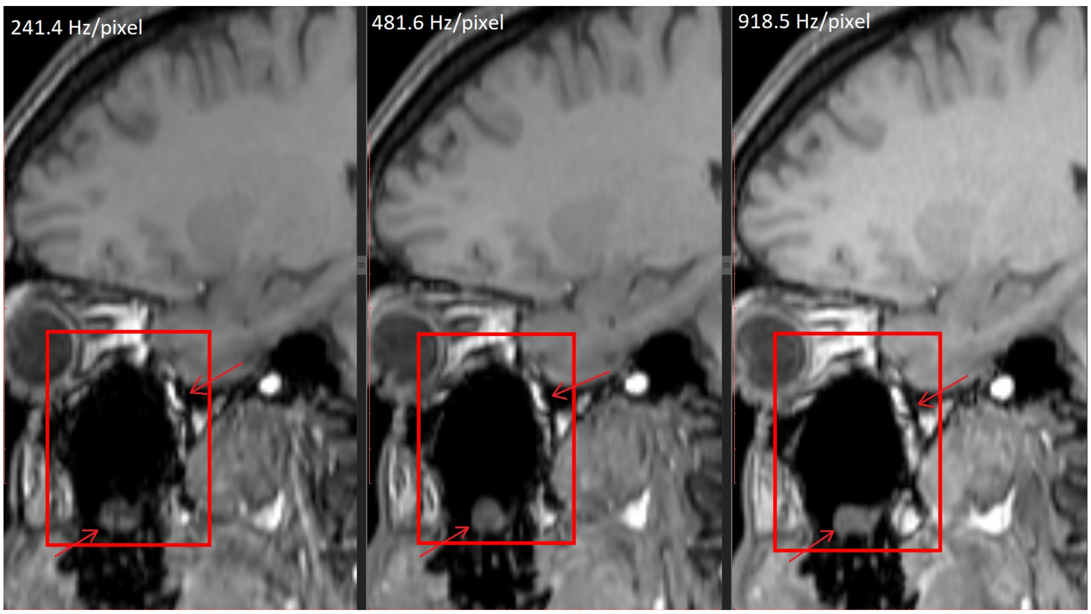

Figure 4.23: The distortion in a sagittal image of the maxillary sinus for readout bandwidth values of 241.4, 481.6, and 918.5 Hz/pixel. The definition of structures along the tissue-air boundary can be seen to increase with increasing bandwidth

As predicted by Figure 4.22, one region which presents a region of high susceptibility induced distortion is the maxillary sinus as seen in Figure 4.23. With increasing bandwidth regions within the maxillary sinus become more defined. This effect can again be seen in the sphenoid sinus in Figure 4.24. The definition of the pituitary gland as well as the tissue-air interface is improved with increasing bandwidth.

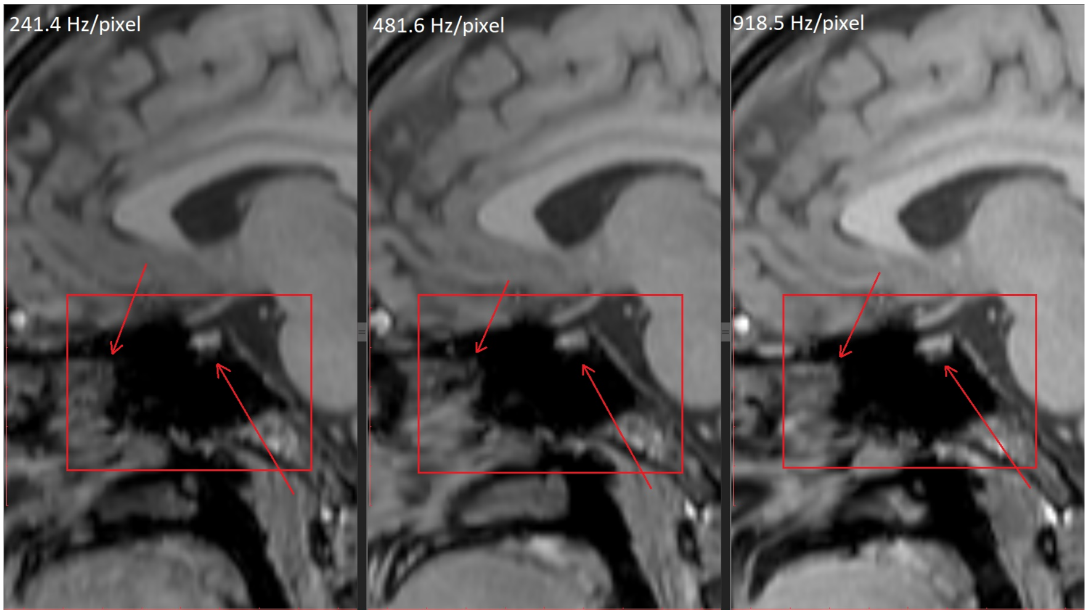

Figure 4.24: The distortion in the sphenoid sinus for readout bandwidth values of 241.4, 481.6, and 918.5 Hz/pixel. The definition of the pituitary glad as well as the tissue-air boundary are increased with increasing bandwidth

4.2.2 Bandwidth effect on SNR

4.2.2.1 ACR Phantom

As explained in section 2.4.3, an increase in the bandwidth comes at the cost of SNR. This relation is described by Equation 2.37. In order to validate the SNR-bandwidth relation, as well as the difference technique, phantom tests were performed in an ACR MRI phantom. As expected, the SNR was seen to decrease as a function of the bandwidth. The expected decrease as described by Equation 2.37 as well as the calculated SNR can be seen in Figure 4.25. This suggests that the SNR values calculated by the difference technique are acceptable as they follow expected relationships. The maximum percent error for the SNR value was 16.9% and seen at the highest bandwidth value of 918.5 Hz/pixel. The minimum percent error was 0.3% with the average percent error across all measurements being 10.0%. As the expected SNR values were calculated using SNR of the 241.4 Hz/pixel bandwidth image, it was assumed that this was the true SNR value.

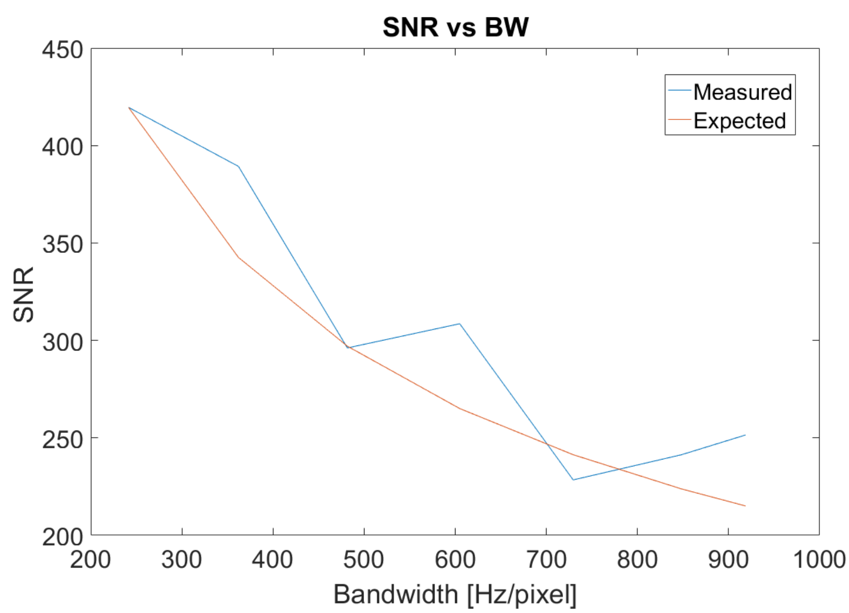

Figure 4.25: The effect of increasing bandwidth on the SNR in the ACR phantom.

4.2.2.2 In-vivo Measurements

In addition to phantom measurement, the SNR-bandwidth relationship and the difference technique were also validated in-vivo. The SNR of the white matter region 1 taken at different bandwidths can be seen in Figure 4.26. The 241.4 Hz/pixel bandwidth image, as expected, had the highest SNR of 111.7, followed by 79.0 for 481.6 Hz/pixel bandwidth image and 59.7 for the 918.5 Hz/pixel bandwidth image. By using the 241.4 Hz/pixel bandwidth image, the expected SNR values of the medium and high bandwidth images were calculated to be 79.0 and 57.3 leading to relative differences of 0% and 4.2%. The agreement seen in the expected and actual SNR in white matter again validates the use of the difference technique in in-vivo SNR calculations.

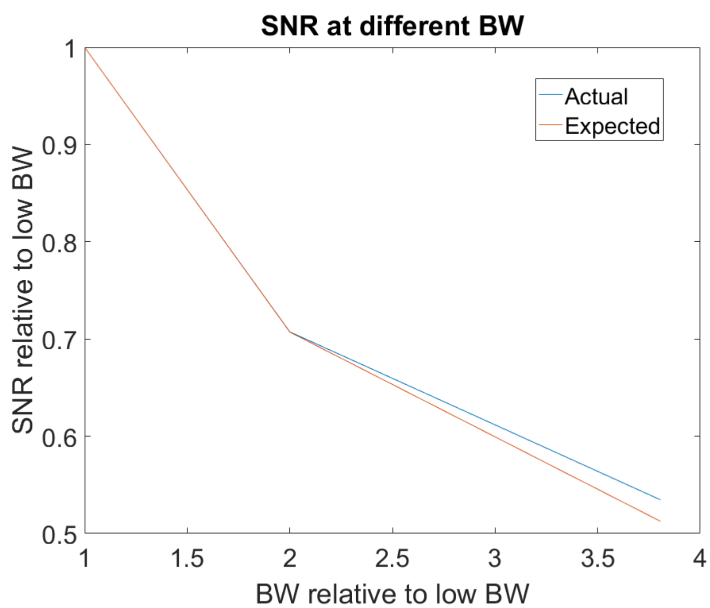

Figure 4.26: The SNR calculated in white matter region 1 versus the expected SNR value. The SNR has been normalized to the SNR of the lowest bandwidth image, and the BW has been normalized to that of the lowest BW. The expected SNR values are calculated with reference to the low bandwidth SNR with the use of Equation 2.37.

4.2.3 Simulation of SNR increase with multi echo averaging

As multi-echo averaging was one proposed method to improve SNR, simulations were performed to determine the SNR increase. The SNR increase for white matter, gray matter and cerebral spinal fluid were modelled by Helms et al., and an adaptation of their simulations can be seen in Figure 4.27 [23]. All SNR values were normalized to that of the first echo. It was noted by Helms et al., that averaging multiple echoes increases the obtained SNR in the image up to a certain echo train length, which corresponds to the T2* value of region [23]. Though the SNR was shown to increase until echo times passed the T2* value of the region, it was also noted by Helms et al., that with increasing echo times an increase in the signal dropout could be observed. Helms et al., suggested keeping echo times lower than 25 ms to reduce signal dropout in regions such as the orbitofrontal cortex. Additionally, a further reduction of the echo train length is suggested if regions prone to signal dropout, such as the orbitofrontal cortex, are regions of interest [23].

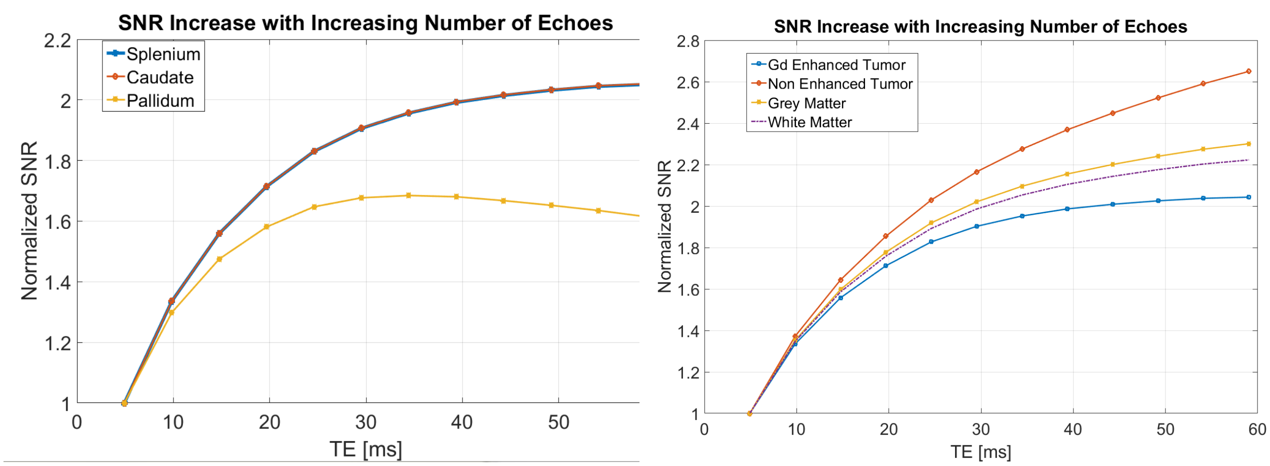

(a) **(b)**

Figure 4.27: (a) Recreation of multi-echo averaging SNR increase from [23]. (b)SNR increase in multi-echo averaging for glioblastomas and healthy brain regions.

4.2.4 Multi-Echo Averaging vs Conventional Signal Averaging

4.2.4.1 SNR Measurment in the ACR Phantom

As multi-echo averaging and conventional signal averaging are both techniques used to increase SNR, they were compared in the ACR MRI phantom. The SNR was calculated in a homogeneous region for the high bandwidth image, the high bandwidth image with 3 signal averages, and the high bandwidth multi-echo image and can be seen in Figure 4.28. The high bandwidth image had an SNR of 166, whereas the high bandwidth image with 3 signal averages had an SNR of 339.6. By using the SNR of the high bandwidth image, an expected SNR of 287.5 was calculated for the high bandwidth image with 3 signal averages, resulting in a percent error of 18.1%. The 5 echoes averaged image on the other hand displayed an SNR of 871.5, which was an increase of over 5.25x that of the high bandwidth image and 2.5x that of the signal averaged image. The SNR value of each sequence, as well as the SNR normalized to that of the high bandwidth 1 signal average image can be seen in Table 4.7. As both the signal averaging image and the echo averaging image used similar imaging times, this suggested that multi-echo averaging was more efficient in increasing the SNR than conventional signal averaging. This result is in agreement with literature as Jutras et al., also compared the SNR efficiency of conventional signal averaging and echo averaging, and were able to show an increased SNR efficiency in the multi-echo images even while using higher sampling bandwidths [30]. Also of note, as the high bandwidth image has a bandwidth value of 918.5 Hz/pixel and and SNR of 166, the SNR of a 241.4 Hz/pixel low bandwidth can be calculated using Equation 2.37. This calculation suggests that the low bandwidth image should have an SNR of approximately 323. By using conventional echo averaging it was seen that the SNR of the high bandwidth image could be regained to equal that of the low bandwidth image, where as multi-echo averaging was able to increase the SNR well beyond that of the low bandwidth image.

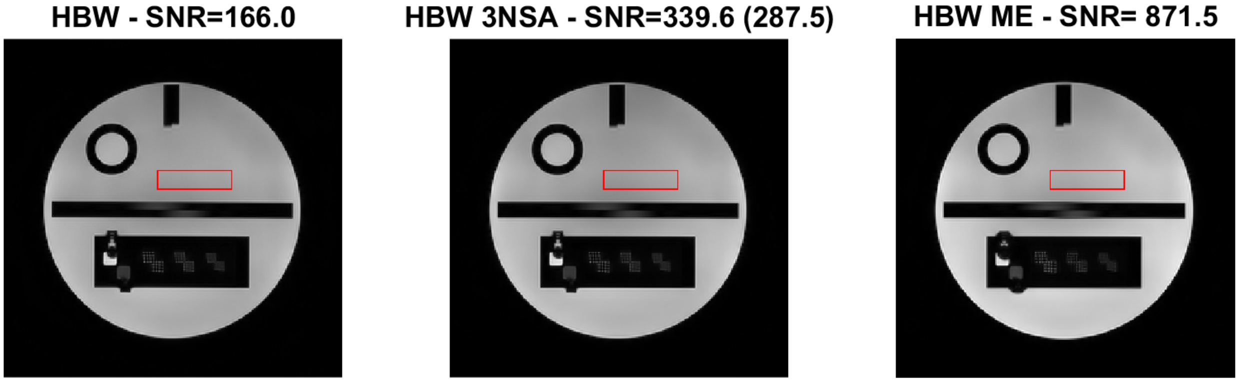

Figure 4.28: The SNR calculated in the high bandwidth, high bandwidth 3 signal averages, and high bandwidth multi-echo images. The expected SNR of the high bandwidth 3 signal average image is given in brackets as calculated from the high bandwidth image.

Table 4.7: The SNR values obtained in the ACR phantom for the high bandwidth 1 signal average, high bandwidth 3 signal average, and multi-echo average images.

Sequence	**SNR**	**Normalized SNR**
High bandwidth 1 NSA	166.0	1
High bandwidth 3 NSA	339.6	2.0
Multi-echo average	871.5	5.25

The SNR of cumulatively averaged echoes can be seen in Figure 4.29. As the SNR is compared to that of the 3 signal averages to determine efficiency, all SNR values have been normalized to that of the 3 signal average image. It was observed that by averaging cumulative echoes a linear increase was obtained in the SNR. The SNR was higher than that of the 3 signal average image by the second echo, and went on to be nearly 2.5x greater by the fifth echo. As SNR is predicted to increase until the T2* value of the object by Helms et al., and the simulations in section 4.2.3, this consistent increase in the SNR can be explained by the fact that very short echo times were used.

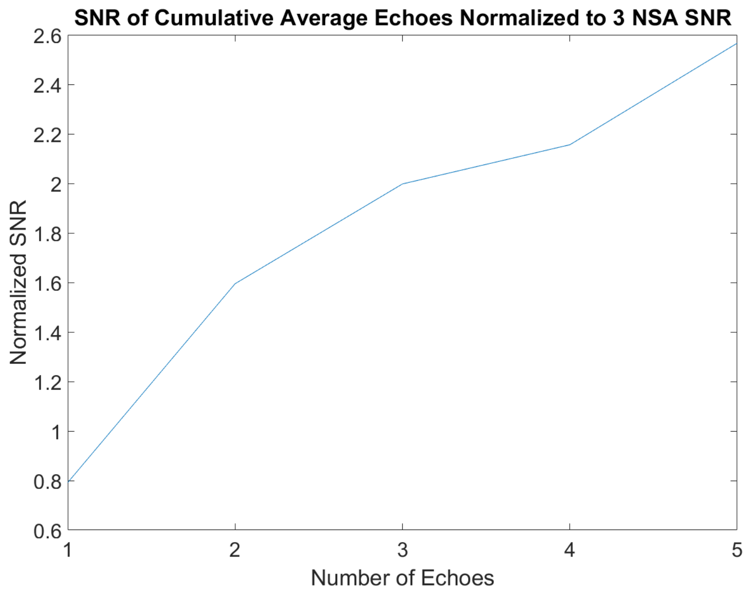

Figure 4.29: The increase in the SNR with cumulative echo averaging as measured in the ACR phantom. The first echo was taken at 1.8 ms with every additional echo at a spacing of 1.65 ms. All SNR values were normalized to the SNR of the high bandwidth 3 signal average image.

4.2.4.2 In-vivo SNR Measurements

An SNR comparison of multi-echo averaging and conventional signal averaging was also performed in a healthy volunteer. Increasing the number of signal averages was seen to increase the SNR in white matter region 1 as described by Equation 2.38. Much like the phantom measurement in section 4.2.4.1, the SNR seen in the multi-echo average image showed a noted increase over the high bandwidth 1 signal average, and high bandwidth 3 signal average images. Once SNR values were normalized to that of the high bandwidth 1 signal average image, it was seen that multi-echo averaging showed a 400% increase in SNR as opposed to the 60% increase of conventional signal averaging. The measured SNR values can be seen in Table 4.8.

Table 4.8: The SNR values obtained in the white matter region 1 for the high bandwidth 1 signal average, high bandwidth 3 signal average, and multi-echo average images.

Sequence	SNR	Normalized SNR
High bandwidth 1 NSA	59.7	1
High bandwidth 3 NSA	94.9	1.6
Multi-echo average	297.8	5.0

Along with the multi-echo averaging, the change in the TR and flip angle to preserve the T1-weighting is also expected to play a role in the SNR increase. With an increase in the TR and flip angle, the signal intensity is increased. The effect on the signal caused by the increased TR and flip angle can be approximated with the use of Equation 2.30. The signal calculated from 2.30 can then be scaled according to 2.38 to account for the number of signal averages. By doing so, the effect of the TR and flip angle were seen to be prominent as the first echo had signal values higher than that of the 3 NSA image. By the fifth echo, the TR and flip angle effect were seen to cause over a 2x increase in the signal as seen in Figure 4.30.

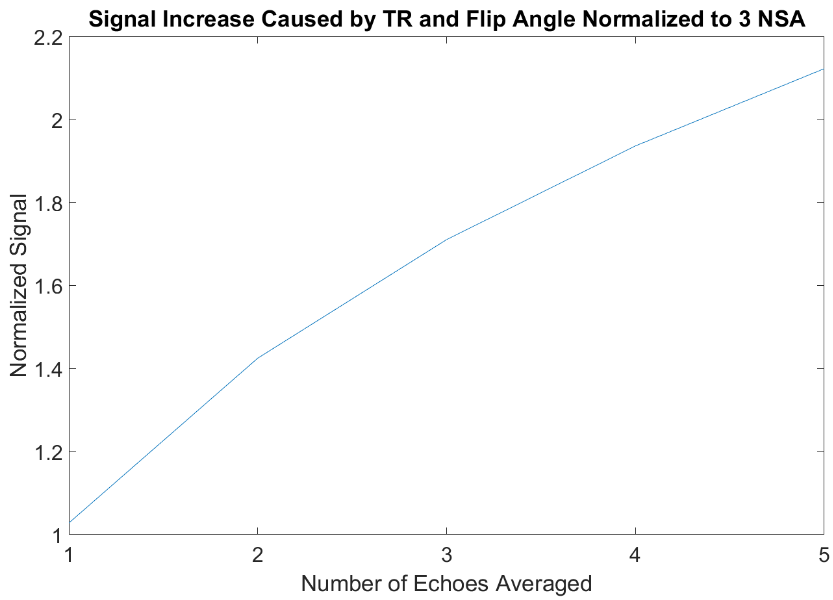

Figure 4.30: The increase in the signal caused by the increased TR and flip angle of the multi-echo sequence. All values were normalized to the signal of the 3 NSA. The TR and flip angle effect is prominent as they cause a higher signal at the first echo and lead to a 2x increase in the signal by the fifth echo.

To further evaluate the SNR of multi-echo averaging, the SNR for each cumulative average was obtained and compared to that of the high bandwidth 3 signal average test. The SNR increase with each additional echo can be seen in Figure 4.31.

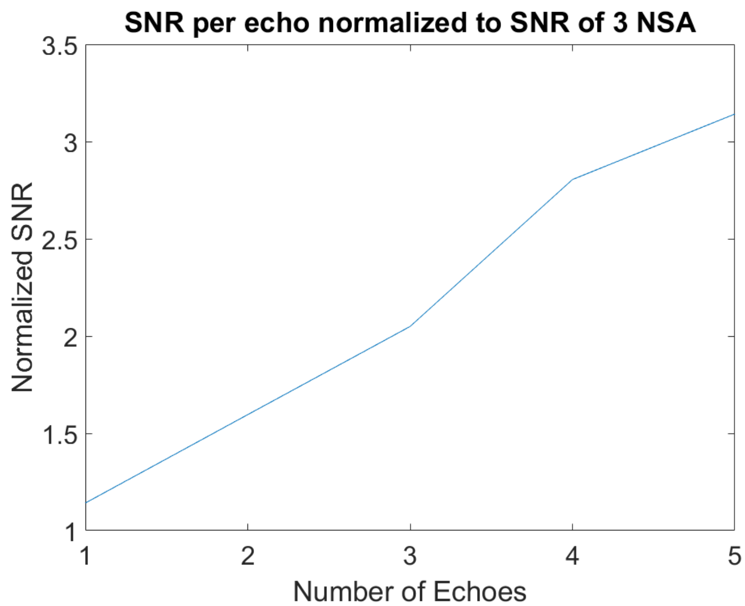

Figure 4.31: The SNR calculated in white matter region 1 for cumulatively averaged echoes. All SNR values have been normalized to that of the 3 signal average image.

The SNR in white matter region 1 for each cumulative echo average can be seen in Figure 4.31. The SNR values were normalized to that of the high bandwidth 3 signal average image. The TR and flip angle effect was seen to be prominent as the first echo alone showed a higher SNR than that of the high bandwidth 3 signal average image. The SNR gain was seen to further increase linearly with an increasing number of echo averages. By the fifth echo the SNR was greater than 3x that of the conventional averaging image. As the TR and flip angle effect was only seen to double the signal intensity by the fifth echo, the use of multi-echo averaging was seen to have an additional benefit.

The SNR was further determined at a second homogenous white matter region and a homogeneous gray matter region as seen in Figure 4.32. In white matter region 2, the SNR was seen to increase until the fourth echo, following which a slight decrease was observed. The gray matter region on the other hand only showed an increase in SNR up to the second echo, at which it plateaued and began to decrease at the fourth echo. Regardless of the plateau or decrease it was noted that all SNR values were higher than that of the conventional signal average image.

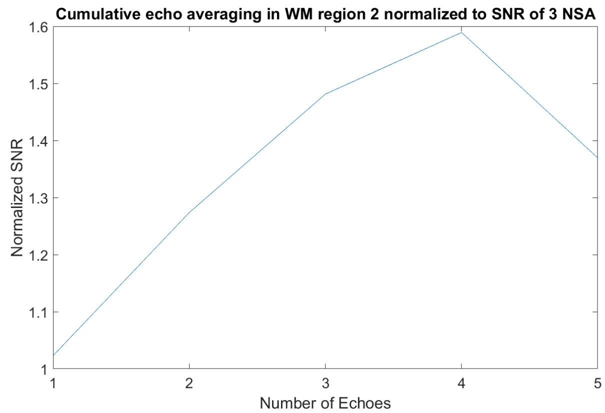

(a)

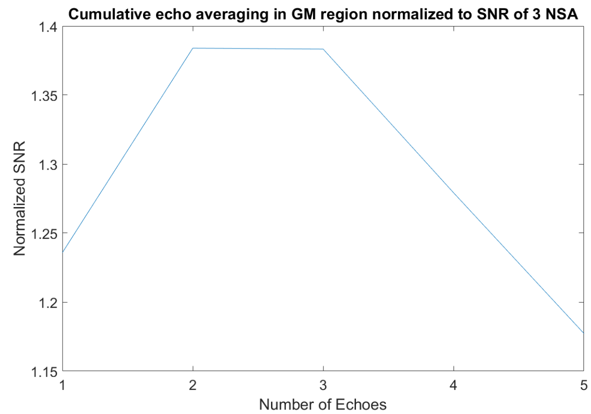

(b)

Figure 4.32: (a) The SNR calculated in white matter region 2 for cumulatively averaged echoes. (b) The SNR calculated in the gray matter region for cumulatively averaged echoes. All SNR values have been normalized to that of the 3 signal average image.

Multi-echo averaging was able to outperform conventional signal averaging in terms of SNR in both phantom and in-vivo tests. In addition to multi-echo averaging, an SNR increase over the current clinical sequence was also measured when a shorter TE, longer TR, and larger flip angle were used. Though a plateau or decrease in the SNR were seen in the grey matter region and white matter region 2, these were only present following the third echo. As opposed to averaging 5 echoes, 3 echoes could be averaged to ensure an adequate SNR increase in all regions. Though the effects caused by a reduced TR and flip angle have to be further studied, this suggests that a reduced number of echoes can be used to obtain an adequate SNR gain. By using a reduced number of echoes, the TR could be reduced resulting in shorter scan times. As the 5 echo scan time was matched to that of the clinical signal average scan, a 3 echo multi-echo scan may provide an increased SNR and shorter scan time than that of the current clinical sequence.

4.2.4.3 In-vivo CNR Measurements

In addition to SNR measurements, CNR measurements were also performed as outlined in Section 3.2.4. The CNR values calculated using the standard deviation in the three regions were normalized to that of the high bandwidth image and can be seen in Table 4.9. Regardless of the region used to obtain the standard deviation, the multi-echo average image always performed better than the high bandwidth 1 signal average, high bandwidth 3 signal average and the first echo images. Though large CNR advantages weren't always seen using multi-echo averaging, the CNR never fell below that of the high bandwidth image.

Table 4.9: The CNR values calculated in the high bandwidth 1 signal average, high bandwidth 3 signal average, only the first echo to represent a short TE scan, and the multi-echo averaged image. All CNR values were normalized to that of the high bandwidth 1 signal average image.

Sequence	**WM1 Normalized CNR**	**WM2 Normalized CNR**	**GM Normalized CNR**
High Bandwidth 1 NSA	1	1	1
First Echo	0.97	0.83	1.12
High Bandwidth 3 NSA	1.05	0.92	1.22
Multi-Echo Average	1.16	1.04	1.35

To further study the effect of multi-echo averaging on the white-gray matter CNR, the CNR was calculated as a function of increasing number of cumulatively averaged echoes, and can be seen in Figure 4.33. All CNR values in Figure 4.33 were normalized to that of the first echo. Regardless of the region used to acquire the standard deviation of the noise, the CNR was seen to increase by averaging at least two echoes. Though the trend following the second echo varied depending on the region used, the CNR value never fell below that of using only one echo. This suggests that using multi-echo averaging provides a CNR advantage over a single short TE scan.

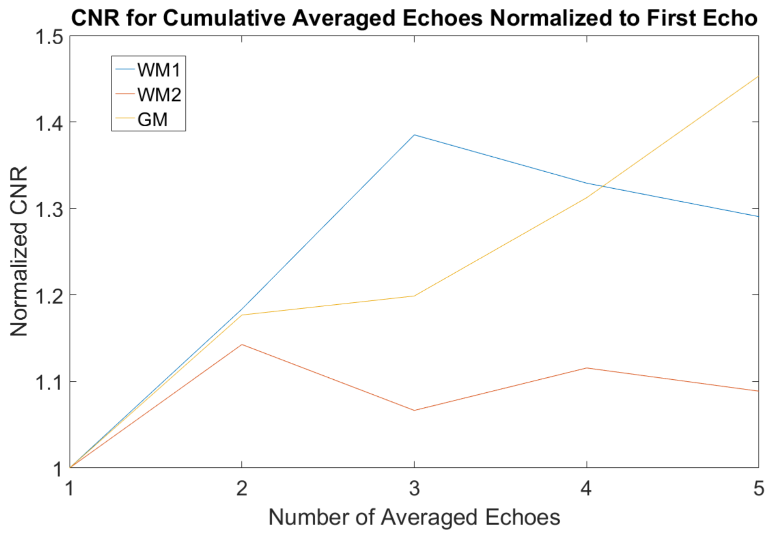

Figure 4.33: The white-grey matter CNR increase with increasing number of echoes averaged. All CNR values were normalized to that of the first echo.

As mentioned in section 2.4.3, two ways to regain the SNR following high bandwidth image acquisition is through the use of conventional signal averaging and multi-echo averaging. As such a comparison between the cumulatively averaged echoes and the 3 signal average image was performed and can be seen in Figure 4.34. The CNR values of the cumulatively averaged echoes were normalized to that of the 3 signal average images to demonstrate the amount of echoes required to obtain a CNR advantage.

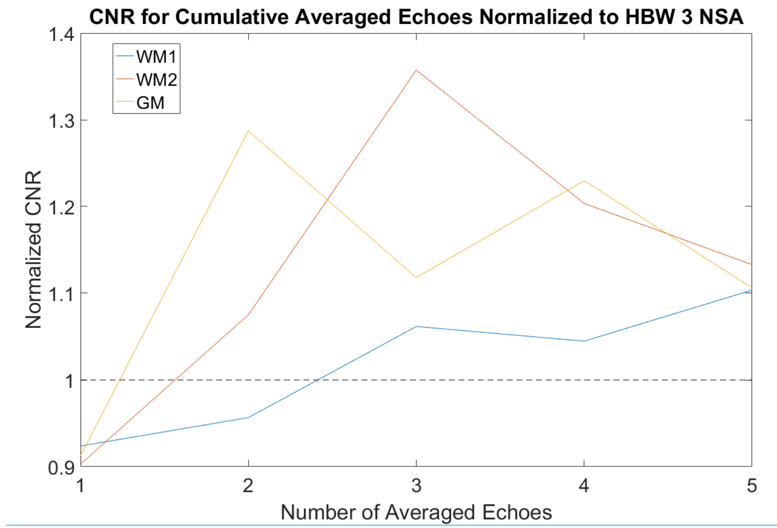

Figure 4.34: The white-grey matter CNR increase with increasing number of echoes averaged. All CNR values were normalized to that high bandwidth 3 signal average image.

Regardless of the region used to obtain the standard deviation of the noise, a CNR advantage was obtained by the third echo. Though a clear trend in the CNR is again not present, it is clear that while using a minimum of three echoes, multi-echo averaging performs superior to conventional signal averaging in terms of white-gray matter contrast-to-noise ratio.

Much like SNR as mentioned in section 4.2.4.2, by the third echo a CNR increase was seen in the multi-echo average relative to conventional signal averaging. As such, to build on from section 4.2.4.2, with the use of a 3 echo multi-echo scan an increase in SNR and CNR may be achieved while reducing the scan time relative to the current clinical scan.

A limitation of the comparisons performed between conventional and multi-echo averaging stems from the fact that they were only performed in images of a healthy volunteer. To further investigate potential advantages of multi-echo averaging, and to provide increased clinical relevance, the comparisons should be made of patients presenting with tumors. Additionally, pre and post contrast images should also be investigated to determine the effect of multi-echo averaging on contrast-enhanced images.

4.2.4.4 Critical Structure Depiction

Images were assessed qualitatively through depiction of critical structures usually contoured for brain radiotherapy. The image quality was compared between the high bandwidth image, the first echo, the conventional signal average and the multi-echo average. The biggest comparison of interest was between the high bandwidth 3 signal average image and the multi-echo average image. Both of these images were acquired for similar imaging times and are of a method used to improve the SNR of high bandwidth image acquisitions. The comparison of the first echo and the multi-echo average was also of interest as they are images obtained during the same acquisition. The first echo image represents the image produced when a short TE is used.

The first critical structure observed was the pituitary gland, which showed the greatest depiction in the high bandwidth image with 1 signal average. Though the edges of the pituitary gland look slightly easier to distinguish in the multi-echo average, the image quality of the first echo, high bandwidth image with 3 signal averages and multi-echo average seemed similar. The image of the pituitary gland in all four images can be seen in Figure 4.35.

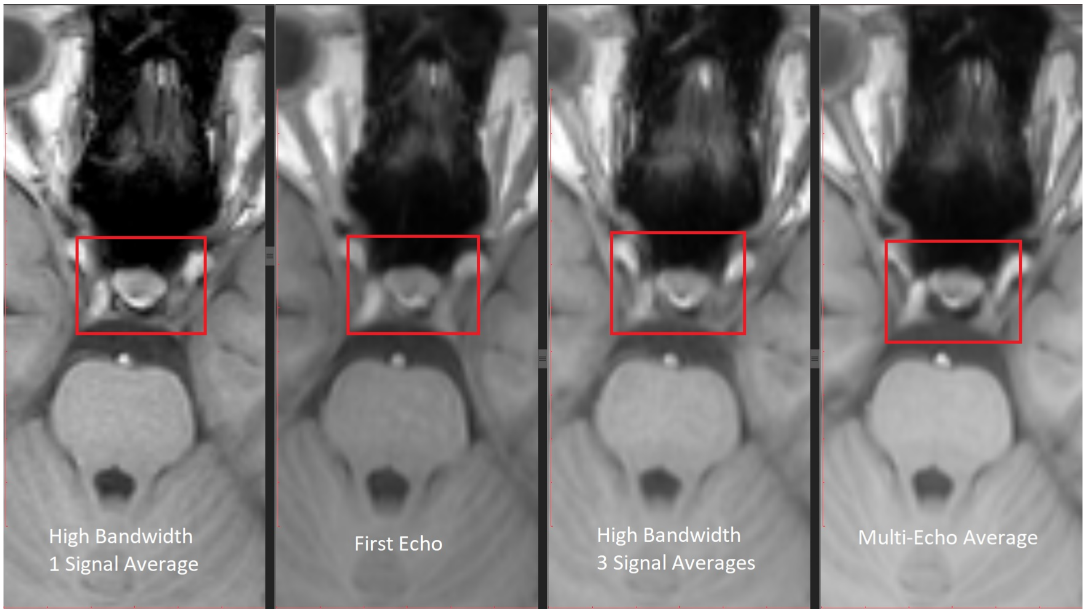

Figure 4.35: The pituitary gland on the high bandwidth, first echo, 3 signal average, and multi-echo average images. The high bandwidth image with 1 signal average showed the best pituitary gland depiction, whereas the depiction in the first echo, high bandwidth image with 3 signal averages, and multi-echo average image seemed similar.

The definition of the lacrimal gland was also seen to be similar for the conventional signal average and multi-echo average images. The definition of the edges was seen to be slightly clearer than that of the high bandwidth, and first echo images. It was noted that the multi-echo average image showed better lacrimal gland depiction than the first echo image. This implies that even though longer echo times are used, resulting in an addition of T2* contrast to the T1-weighted image, the mixed T1+T2*-weighting helps with lacrimal gland depiction. The lacrimal gland in all four images has can be seen in Figure 4.36.

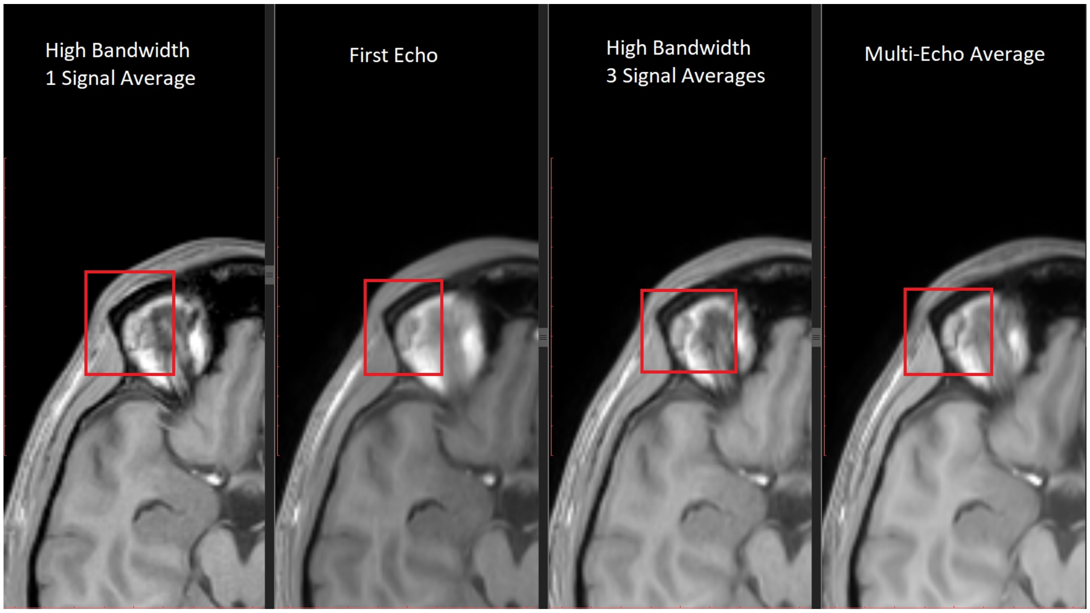

Figure 4.36: The lacrimal gland on the high bandwidth, first echo, 3 signal average, and multi-echo average images. The depiction of the lacrimal gland is similar for the high bandwidth image with 3 signal average and the multi-echo average image. The conventional signal average and multi-echo average images out perform the high bandwidth image with 1 signal average and the first echo image.

The depiction of the optic nerve on the other hand showed a clear improvement in the multi-echo average image, relative to all other tested images. The conventional signal average image showed an improvement over the high bandwidth 1 signal average image and the first echo image, but it displayed a slight distortion which was not present in the multi-echo average image. As the distortion was observed near the eye, eye motion may have contributed to the reduction in image quality as no measure was taken to ensure the eye remained completely still. As the time of each scan was similar however, equal eye movement was assumed for each image leading to a fair comparison. The optic nerve in all four images can be seen in Figures 4.37.

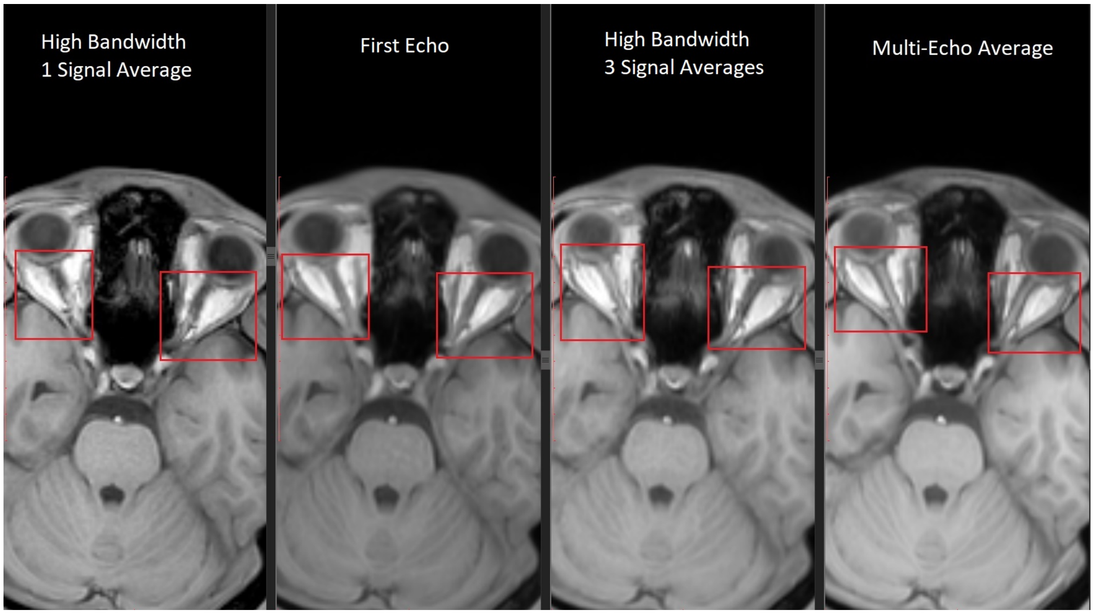

Figure 4.37: The optic nerve on the high bandwidth, first echo, 3 signal average, and multi-echo average images. The optic nerve seems to be the most defined on the multi-echo average image. The optic nerve shows the greatest depiction in the multi-echo average image. The conventional signal average image shows better depiction than the first echo image and the high bandwidth 1 signal average image.

The definition of the optic chiasm was the final critical structure observed, and its depiction was seen to be similar in the high bandwidth, first echo and high bandwidth 3 signal average images. Of the four images acquired, the clearest depiction of the optic chiasm was seen in the multi-echo average image. The optic chiasm can be seen in Figure 4.38.

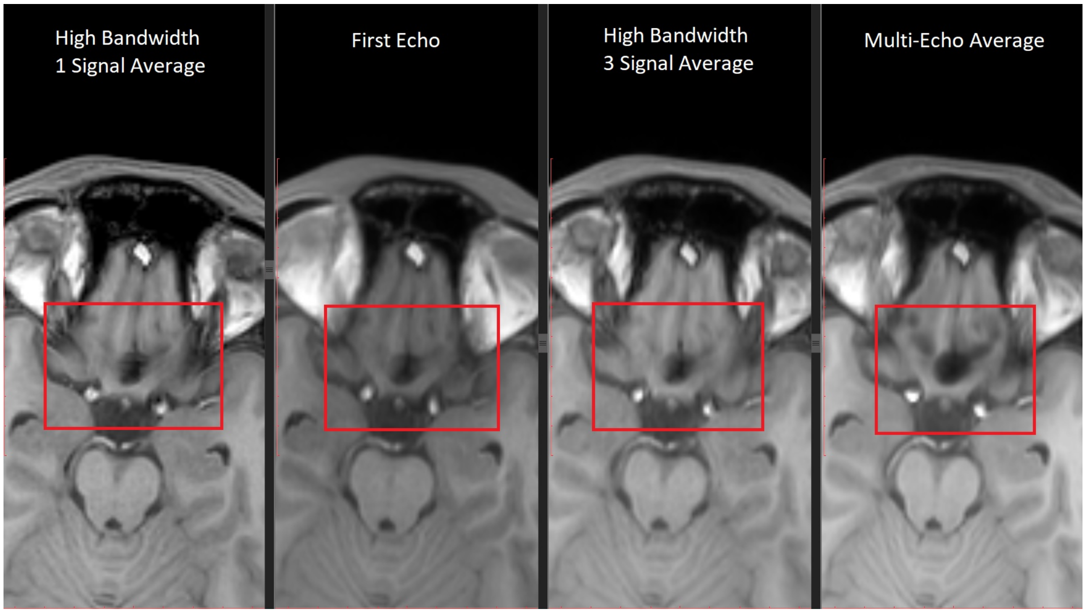

Figure 4.38: The optic chiasm on the high bandwidth, first echo, 3 signal average, and multi echo average images. The optic chiasm seems to be the most defined on the multi-echo average image.

It should be noted however that though the images were qualitatively assessed, they were not assessed by a clinician. With the help of clinicians to rank the obtain images, further insight can be gained into the clinical relevance of the qualitative image quality improvements.

4.2.5 Summary of Patient-Dependent Distortion and Multi-Echo Gradient Echo Image Quality Experiments

Regions of expected high patient-dependent distortions were determined in a healthy volunteer and were found to be at air-tissue and air-bone interfaces. Four regions of note were the frontal, maxillary and sphenoid sinuses, along with the ear canals. The patient dependent distortions were seen to be reduced with increased readout bandwidth.

Though the increased bandwidth resulted in reduced patient-dependent distortions, it also lead to a reduced SNR. The SNR-bandwidth relationship observed was seen to be consistent with Equation 2.37. The lost SNR was then regained through the use of conventional signal averaging and multi-echo averaging. For image acquisition of similar scan time, multi-echo averaging outperformed conventional signal averaging in terms of SNR. Additionally, the CNR of the multi-echo average image was either better than or equivalent to the conventional signal averaging for all regions tested. Finally, the depiction of relevant critical structures in brain radiotherapy were compared for the high bandwidth 1 signal average, first echo, high bandwidth 3 signal average and multi-echo average images. The depiction of the pituitary gland and lacrimal gland was similar for the conventional signal average and multi-echo average image, whereas the depiction of the optic nerve and optic chiasm was greatest in the multi-echo average image.

Chapter 5

Conclusion and Future Work

Quantification of system-dependent distortion was performed on a Phillips 3 T Ingenia over a large field of view using a phantom with appropriate dimensions to approximate pelvic or abdominal imaging. The distortion fields were obtained for the T1-w 3D gradient echo, T2-w 2D spin echo, T2-w 3D spin echo, and T1-w THRIVE sequences. By using a conservative acceptable radial distance for radiation therapy obtained from the 99.5 percentile maximum distortion, the T1-w 3D GRE and T2-w 3D GRE were seen to have the largest acceptable radial distance of the tested sequences. The T1-w 3D GRE had an acceptable radial distance of 255 mm from the isocenter, whereas the T2-w SE had an acceptable radial distance of 250 mm. The T2-w SE however showed a large degree of signal drop out at large radial distances, suggesting the T1-w GRE may be more appropriate for radiation therapy planning close to the edge of the FOV. Distortions values were reduced with increased bandwidth, but the reduction was only seen past 200 mm and in the frequency encode direction. Sequence independent distortions were also measured and seen to be below 1.5 mm for the volume tested.

Regions of expected patient-dependent distortions were then calculated and observed to be high at air-tissue and air-bone interfaces. Of note, the frontal sinus, maxillary sinus, sphenoid sinus and ear canals were the regions of highest expected distortions in the head. The present distortions were seen to qualitatively decrease with an increase in bandwidth, at the cost of SNR. Multi-echo averaging and conventional averaging were performed to regain the lost SNR and were compared. Multi-echo averaging was seen to outperform conventional echo averaging in terms of SNR and CNR. Additionally, multi-echo averaging was seen to either outperform or was equal to conventional echo averaging in terms of image quality. Depiction of the pituitary and lacrimal glands were seen to be similar for the conventional signal average image and the multi-echo average image, where as the multi-echo average showed improved depiction of the optic nerve and the optic chiasm. Though the effect of a reduced TR and flip angle may need to be studied, it was seen that by the use of a 3 echo multi-echo scan, the SNR and CNR may be improved while simultaneously reducing the scan time as compared to conventional signal averaging.

To further investigate the benefits of multi-echo averaging, the way in which the images were averaged can be optimized. To obtain the multi-echo average images in this thesis, each echo was simply added and divided by the total number of echoes. Literature suggests however that, depending on the sequence used, the root sum of squares or a weighted average may be more advantageous in terms of SNR gain [30]. The different averaging techniques can be performed and image quality can again be assessed, along with computational times, to determine an optimal method for radiation therapy planning and the radiation therapy planning workflow.

Bibliography

[1] *Prescribing, Recording and Reporting Photon Beam Therapy (Supplement to ICRU Report 50)*. ICRU, 1rst edition, 1999.

[2] M. Ahmed, M. Schmidt, A. Sohaib, C. Kong, K. Burke, C. Richardson, M. Usher, S. Brennan, A. Riddell, M. Davies, K. Newbold, K. Harrington, and C. Nutting. The value of magnetic resonance imaging in target volume delineation of base of tongue tumours - a study using flexible surface coils. *Radiotherapy and Oncology*, 94(2):161–167, 2010.

[3] H. Aoyama, H. Shirato, T. Nishioka, S. Hashimoto, K. Tsuchiya, K. Kagei, R. Onimaru, Y. Watanabe, and K. Miyasaka. Magnetic resonance imaging system for three-dimensional conformal radiotherapy and its impact on gross tumor volume delineation of central nervous system tumors. *International Journal of Radiation Oncology*Biology*Physics*, 50(3):821–827, 2001.

[4] L. N. Baldwin, K. Wachowicz, and B. G. Fallone. A two-step scheme for distortion rectification of magnetic resonance images. *Medical Physics*, 36(9Part1):3917–3926, 2009.

[5] L. N. Baldwin, K. Wachowicz, S. D. Thomas, R. Rivest, and B. G. Fallone. Characterization, prediction, and correction of geometric distortion in 3 T MR images. *Medical Physics*, 34(2):388, 2007.

[6] A. Berrington de Gonzalez, M. Mahesh, and K.-P. Kim. Projected cancer risks from computed tomographic scans performed in the united states in 2007. *Journal of Vascular Surgery*, 51(3):783, 2010.

[7] B. Blasiak, S. Barnes, T. Foniok, D. Rushforth, J. Matyas, D. Ponjevic, W. P. Weglarz, R. Tyson, U. Iqbal, A. Abulrob, G. Sutherlan, A. Obenause, and B. Tomanek. Com-

parison of T2 and T2 *-weighted MR molecular imaging of a mouse model of glioma. *BMC Medical Imaging*, 13(1), 2013.

[8] G. Burkill, R. Evans, V. Raman, and S. Connor. Modern radiology in the management of head and neck cancer. *Clinical Oncology*, 28(7):440–450, 2016.

[9] A. Carlsson, G. Starck, M. Ljungberg, S. Ekholm, and E. Forssell-Aronsson. Accurate and sensitive measurements of magnetic susceptibility using echo planar imaging. *Magnetic Resonance Imaging*, 24(9):1179–1185, 2006.

[10] Z. Chen, C.-M. Ma, K. Paskalev, J. Li, J. Yang, T. Richardson, L. Palacio, X. Xu, and L. Chen. Investigation of MR image distortion for radiotherapy treatment planning of prostate cancer. *Physics in Medicine and Biology*, 51(6):1393–1403, 2006.

[11] A. L. Chin, A. Lin, S. Anamalayil, and B.-K. K. Teo. Feasibility and limitations of bulk density assignment in MRI for head and neck IMRT treatment planning. *Journal of Applied Clinical Medical Physics*, 15(5):100–111, 2014.

[12] H. R. Cho, D. H. Kim, D. Kim, P. Doble, D. Bishop, D. Hare, C.-K. Park, W. K. Moon, M. H. Han, and S. H. Choi. Malignant Glioma: MR Imaging by Using 5-Aminolevulinic Acid in an Animal Model. *Radiology*, 272(3):720–730, 2014.

[13] P. Dammann, O. Kraff, K. H. Wrede, N. Ozkan, S. Orzada, O. M. Mueller, I. E. Sandalcioglu, U. Sure, E. R. Gizewski, M. E. Ladd, and T. Gasser. Evaluation of hardware-related geometrical distortion in structural MRI at 7 tesla for image-guided applications in neurosurgery. *Academic Radiology*, 18(7):910–916, 2011.

[14] E. M. Delfaut, J. Beltran, G. Johnson, J. Rousseau, X. Marchandise, and A. Cotten. Fat suppression in MR Imaging: Techniques and Pitfalls. *RadioGraphics*, 19(2):373–382, 1999.

[15] O. Dietrich, J. G. Raya, S. B. Reeder, M. F. Reiser, and S. O. Schoenberg. Measurement of signal-to-noise ratios in MR images: Influence of multichannel coils, parallel imaging, and reconstruction filters. *Journal of Magnetic Resonance Imaging*, 26(2):375–385, 2007.

[16] S. J. Doran, L. Charles-Edwards, S. A. Reinsberg, and M. O. Leach. A complete distortion correction for MR images: I. gradient warp correction. *Physics in Medicine and Biology*, 50(7):1343–1361, 2005.

[17] W. A. Edelstein, J. M. S. Hutchison, G. Johnson, and T. Redpath. Spin warp NMR imaging and applications to human whole-body imaging. *Physics in Medicine and Biology*, 25(4):751–756, 1980.

[18] B. Emami, A. Sethi, and G. J. Petruzzelli. Influence of MRI on target volume delineation and IMRT planning in nasopharyngeal carcinoma. *International Journal of Radiation Oncology*Biology*Physics*, 57(2):481–488, 2003.

[19] K. Farahani, U. Sinha, S. Sinha, L. C.-L. Chiu, and R. B. Lufkin. Effect of field strength on susceptibility artifacts in magnetic resonance imaging. *Computerized Medical Imaging and Graphics*, 14(6):409–413, 1990.

[20] V. Fortier and I. Levesque. Phase processing for quantitative susceptibility mapping of regions with large susceptibility and lack of signal susceptibility and lack of signal [abstract]. In: International Society for Magnetic Resonance in Medicine, Honolulu, 2017.

[21] G. Glover and N. Pelc. Method for correcting image distortion due to gradient nonuniformity, May 27 1986. US Patent 4,591,789.

[22] X. Gu, H. Pan, Y. Liang, R. Castillo, D. Yang, D. Choi, E. Castillo, A. Majumdar, T. Guerrero, and S. B. Jiang. Implementation and evaluation of various demons deformable image registration algorithms on a GPU. *Physics in Medicine and Biology*, 55(1):207–219, 2009.

[23] G. Helms and P. Dechent. Increased SNR and reduced distortions by averaging multiple gradient echo signals in 3D FLASH imaging of the human brain at 3T. *Journal of Magnetic Resonance Imaging*, 29(1):198–204, 2009.

[24] B. Hentschel, W. Oehler, D. Strauss, A. Ulrich, and A. Malich. Definition of the CTV prostate in CT and MRI by using CT-MRI image fusion in IMRT planning for prostate cancer. *Strahlentherapie und Onkologie*, 187(3):183–190, 2011.

[25] C. Hong, D.-H. Lee, and B. S. Han. Characteristics of geometric distortion correction with increasing field-of-view in open-configuration MRI. *Magnetic Resonance Imaging*, 32:786–790, 2014.

[26] A. Janke, H. Zhao, G. J. Cowin, G. J. Galloway, and D. M. Doddrell. Use of spherical harmonic deconvolution methods to compensate for nonlinear gradient effects on MRI images. *Magnetic Resonance in Medicine*, 52(1):115–122, 2004.

[27] D. Jones. ICRU Report 50-Prescribing, Recording and Reporting Photon Beam Therapy. *Medical Physics*, 21(6):833–834, 1994.

[28] J. H. Jonsson, M. G. Karlsson, M. Karlsson, and T. Nyholm. Treatment planning using MRI data: an analysis of the dose calculation accuracy for different treatment regions. *Radiation Oncology*, 5(1):62, 2010.

[29] J. Jovicich, S. Czanner, D. Greve, E. Haley, A. van der Kouwe, R. Gollub, D. Kennedy, F. Schmitt, G. Brown, J. MacFall, B. Fischl, and A. Dale. Reliability in multi-site structural MRI studies: Effects of gradient non-linearity correction on phantom and human data. *NeuroImage*, 30(2):436–443, 2006.

[30] J.-D. Jutras, K. Wachowicz, G. Gilbert, and N. De Zanche. SNR efficiency of combined bipolar gradient echoes: Comparison of three-dimensional FLASH, MPRAGE, and multiparameter mapping with VFA-FLASH and MP2RAGE. *Magnetic Resonance in Medicine*, 77(6):2186–2202, 2016.

[31] C. Kalavagunta and G. Metzger. A field comparison of R1 and R2* relaxivities of Gd-DTPA in aqueous solution and whole blood: 3T versus 7T. In *Proc ISMRM*, volume 18, page 4990, 2010.

[32] L. Koivula, L. Wee, and J. Korhonen. Feasibility of MRI-only treatment planning for proton therapy in brain and prostate cancers: Dose calculation accuracy in substitute CT images. *Medical Physics*, 43(8):4634–4642, 2016.

[33] J. Lambert, P. B. Greer, F. Menk, J. Patterson, J. Parker, K. Dahl, S. Gupta, A. Capp, C. Wratten, C. Tang, M. Kumar, J. Dowling, S. Hauville, C. Hughes, K. Fisher, P. Lau, J. Denhham, and O. Salvado. MRI-guided prostate radiation therapy planning: Investigation of dosimetric accuracy of MRI-based dose planning. *Radiotherapy and Oncology*, 98(3):330–334, 2011.

[34] J. C. Lau, A. R. Khan, T. Y. Zeng, K. W. MacDougall, A. G. Parrent, and T. M. Peters. Quantification of local geometric distortion in structural magnetic resonance images: Application to ultra-high fields. *NeuroImage*, 2017.

[35] D. W. McRobbie, E. A. Moore, M. J. Graves, and M. R. Prince. *MRI from picture to proton*. Cambridge University Press, 2 edition, 2006.

[36] D. G. Nishimura. *Principles of magnetic resonance imaging*. Stanford University, 2010.

[37] P. M. Parizel, B. A. van Hasselt, L. van den Hauwe, J. W. V. Goethem, and A. M. D. Schepper. Understanding chemical shift induced boundary artefacts as a function of field strength: influence of imaging parameters (bandwidth, field-of-view, and matrix size). *European Journal of Radiology*, 18(3):158 – 164, 1994.

[38] C. Park and O. I. Kwon. Current density imaging using directly measured harmonicbzdata in MREIT. *Computational and Mathematical Methods in Medicine*, 2013:1–9, 2013.

[39] D. Pasquier, N. Betrouni, M. Vermandel, T. Lacornerie, E. Lartigau, and J. Rousseau. MRI alone simulation for conformal radiation therapy of prostate cancer: technical aspects. In *2006 International Conference of the IEEE Engineering in Medicine and Biology Society*, Aug 2006.

[40] A. M. Peters, M. J. Brookes, F. G. Hoogenraad, P. A. Gowland, S. T. Francis, P. G. Morris, and R. Bowtell. T2* measurements in human brain at 1.5, 3 and 7 T. *Magnetic Resonance Imaging*, 25(6):748–753, 2007.

[41] A. Popovtzer, M. Ibrahim, D. Tatro, F. Y. Feng, R. K. T. Haken, and A. Eisbruch. MRI to delineate the gross tumor volume of nasopharyngeal cancers: which sequences and planes should be used? *Radiology and Oncology*, 48(3), 2014.

[42] C. Rasch, R. Keus, F. A. Pameijer, W. Koops, V. de Ru, S. Muller, A. Touw, H. Bartelink, M. van Herk, and J. V. Lebesque. The potential impact of CT-MRI matching on tumor volume delineation in advanced head and neck cancer. *International Journal of Radiation Oncology*Biology*Physics*, 39(4):841–848, 1997.

[43] J. R. Reichenbach, R. Venkatesan, D. A. Yablonskiy, M. R. Thompson, S. Lai, and E. M. Haacke. Theory and application of static field inhomogeneity effects in gradient-echo imaging. *Journal of Magnetic Resonance Imaging*, 7(2):266–279, 1997.

[44] J. F. Schenck. The role of magnetic susceptibility in magnetic resonance imaging: MRI magnetic compatibility of the first and second kinds. *Medical Physics*, 23(6):815–850, 1996.

[45] F. Schick. Whole-body MRI at high field: technical limits and clinical potential. *European Radiology*, 15(5):946–959, 2005.

[46] H. H. Schild. *MRI made easy.* Schering AG, 1990.

[47] T. Seibert, N. White, G. Kim, C. McDonald, N. Farid, V. Moiseenko, H. Bartsch, J. Kuperman, D. Holland, A. Mundt, A. Dale, and J. Hattangadi-Gluth. Distortion inherent to magnetic resonance imaging (MRI) can lead to geometric miss in radiosurgery planning. *International Journal of Radiation Oncology*Biology*Physics*, 90(1):S97, 2014.

[48] R. Smith-Bindman, J. Lipson, R. Marcus, K. P. Kim, M. Mahesh, R. Gould, A. B. de Gonzalez, and D. L. Miglioretti. Radiation dose associated with common computed tomography examinations and the associated lifetime attributable risk of cancer. *Archives of Internal Medicine*, 169(22):2078, 2009.

[49] B. Stall, L. Zach, H. Ning, J. Ondos, B. Arora, R. Miller, S. Smith, D. Citrin, and K. Camphausen. Comparison of T2 and FLAIR imaging for target delineation in high grade gliomas. *International Journal of Radiation Oncology*Biology*Physics*, 72(1):S530–S531, 2008.

[50] T. Stanescu, J. Hans-Sonke, K. Wachowicz, and G. Fallone. Investigation of a 3D system distortion correction method for MR images. *Journal of Applied Clinical Medical Physics*, 11(1):200–216, 2010.

[51] T. Stanescu, H.-S. Jans, N. Pervez, P. Stavrev, and B. G. Fallone. A study on the magnetic resonance imaging (MRI)-based radiation treatment planning of intracranial lesions. *Physics in Medicine and Biology*, 53(13):3579–3593, 2008.

[52] T. Stanescu, K. Wachowicz, and D. A. Jaffray. Characterization of tissue magnetic susceptibility-induced distortions for MRIgRT. *Medical Physics*, 39(12):7185, 2012.

[53] J. Sun, J. Dowling, P. Pichler, F. Menk, D. Rivest-Henault, J. Lambert, J. Parker, J. Arm, L. Best, J. Martin, J. Denham, and P. Greer. MRI simulation: end-to-end testing for prostate radiation therapy using geometric pelvic MRI phantoms. *Physics in Medicine and Biology*, 60(8):3097–3109, 2015.

[54] T. Tadic, D. A. Jaffray, and T. Stanescu. Harmonic analysis for the characterization and correction of geometric distortion in MRI. *Medical Physics*, 41(11):112303, 2014.

[55] S. F. Tanner, D. J. Finnigan, V. S. Khoo, P. Mayles, D. P. Dearnaley, and M. O. Leach. Radiotherapy planning of the pelvis using distortion corrected MR images: the removal of system distortions. *Physics in Medicine and Biology*, 45(8):2117–2132, 2000.

[56] R. Ten Haken, A. Thornton, H. Sandler, M. LaVigne, D. Quint, B. Fraass, M. Kessler, and D. McShan. A quantitative assessment of the addition of MRI to CT-based, 3-D treatment planning of brain tumors. *Radiotherapy and Oncology*, 25(2):121–133, 1992.

[57] B. Teo, A. Chin, and A. Lin. Dosimetric accuracy of bulk density assignment on MRI for head and neck IMRT treatment planning. *International Journal of Radiation Oncology*Biology*Physics*, 87(2):S15, 2013.

[58] J.-P. Thirion. Fast Non-Rigid Matching of 3D Medical Images. Research Report RR-2547, INRIA, 1995.

[59] J.-P. Thirion. Image matching as a diffusion process: an analogy with Maxwell's demons. *Medical Image Analysis*, 2(3):243–260, 1998.

[60] T. Torfeh, R. Hammoud, G. Perkins, M. McGarry, S. Aouadi, A. Celik, K.-P. Hwang, J. Stancanello, P. Petric, and N. Al-Hammadi. Characterization of 3D geometric distortion of magnetic resonance imaging scanners commissioned for radiation therapy planning. *Magnetic Resonance Imaging*, 34(5):645–653, 2016.

[61] K. Ulin, M. M. Urie, and J. M. Cherlow. Results of a multi-institutional benchmark test for cranial CT/MR image registration. *International Journal of Radiation Oncology*Biology*Physics*, 77(5):1584–1589, 2010.

[62] R. Viard, N. Betrouni, M. Vermandel, S. Mordon, J. Rousseau, and M. Vanhoutte. Characterization and 3D correction of geometric distortion in low-field open-magnet mri. pages 3649–3652, Aug 2008.

[63] K. Wachowicz, T. Stanescu, S. D. Thomas, and B. G. Fallone. Implications of tissue magnetic susceptibility-related distortion on the rotating magnet in an MR-linac design. *Medical Physics*, 37(4):1714, 2010.

[64] A. Walker, G. Liney, P. Metcalfe, and L. Holloway. MRI distortion: considerations for MRI based radiotherapy treatment planning. *Australas Phys Eng Sci Med*, 37(1):103–113, 2014.

[65] D. Wang, D. M. Doddrell, and G. Cowin. A novel phantom and method for comprehensive 3-dimensional measurement and correction of geometric distortion in magnetic resonance imaging. *Magnetic Resonance Imaging*, 22(4):529–542, 2004.

[66] H. Wang, J. Balter, and Y. Cao. Patient-induced susceptibility effect on geometric distortion of clinical brain MRI for radiation treatment planning on a 3T scanner. *Physics in Medicine and Biology*, 58(3):465–477, 2013.

[67] A. R. Webb. *Introduction to biomedical imaging*. IEEE, 2003.

[68] D. Weber, H. Wang, S. Albrecht, M. Ozsahin, E. Tkachuk, M. Rouzaud, P. Nouet, and G. Dipasquale. Open low-field magnetic resonance imaging for target definition, dose calculations and set-up verification during three-dimensional CRT for glioblastoma multiforme. *Clinical Oncology*, 20(2):157–167, 2008.

[69] J. Weygand, C. D. Fuller, G. S. Ibbott, A. S. Mohamed, Y. Ding, J. Yang, K.-P. Hwang, and J. Wang. Spatial precision in magnetic resonance imaging guided radiation therapy: The role of geometric distortion. *International Journal of Radiation Oncology*Biology*Physics*, 95(4):1304–1316, 2016.

[70] J. M. Wild, N. Woodhouse, M. N. Paley, S. Fichele, Z. Said, L. Kasuboski, and E. J. van Beek. Comparison between 2D and 3D gradient-echo sequences for MRI of human lung ventilation with hyperpolarized 3He. *Magnetic Resonance in Medicine*, 52(3):673–678, 2004.